Great Britain
Journals Press

GB JP

London Journal of
Engineering Research

Volume 24 | Issue 8 | Compilation 1.0

COMPILED IN UNITED KINGDOM

ENGLISH

They were leaders in building the early foundation of modern programming and unveiled the structure of DNA Their work inspired environmental movements and led to the discovery of new genes They've gone to space and back taught us about the natural world dug up the earth and discovered the origins of our species They broke the sound barrier and gender barriers along the way The world of research wouldn't be the same without the pioneering efforts of famous research works made by these women Be inspired by these explorers and early adopters- the women in research who helped to shape our society We invite you to sit with their stories and enter new areas of understanding This list is by no means a complete record of women to whom we are indebted for their research work but here are of history's greatest research contributions made by...

Read complete here:
https://goo.gl/1vQ3lS

Women In Research

Computing in the cloud!

Cloud Computing is computing as a Service and not just as a Product Under Cloud Computing...

Read complete here:
https://goo.gl/VvHC72

Writing great research...

Prepare yourself before you start Before you start writing your paper or you start reading other...

Read complete here:
https://goo.gl/np73jP

Journal Content
In this Issue

Great Britain
Journals Press

Study on the Landslide Caused by Difference Creep Behavior of Loess under Highway Excavation

Xuanyu Yang & Yaming Liu

University of Chinese Academy of Sciences

ABSTRACT

Large-scale road construction in mountainous areas inevitably leads to numerous excavation slopes, particularly in the Loess Plateau, characterized by abundant ancient landslides and complex stratigraphy. Excavation-induced stress relief can easily reactivate these ancient landslides, posing significant threats to engineering safety. This study takes an ancient landslide in the Loess Plateau as a case example. Field investigations clarified the lithological characteristics of the strata. Indoor triaxial unloading tests were conducted to examine the unloading creep behavior of silty soil and clay located near the sliding zone. Finally, numerical simulations were employed to analyze the evolution process of landslide reactivation induced by excavation. The study revealed the following findings: (1) The primary factor inducing the landslide is the differential unloading creep behavior of silty soil and clay. Silty soil readily reaches an accelerated creep state under unloading conditions, whereas clay remains relatively stable with smaller deformation. The creep behavior of the soil can be well described using the Nishihara model. (2) Comparison of two unloading stress paths showed that vertical stress unloading causes minor rebound deformation with minimal impact on overall deformation.

Keywords: loess plateau; ancient landslide; unloading creep; differential deformation; stress path.

Classification: LCC Code: GB1399.5

Language: English

Study on the Landslide Caused by Difference Creep Behavior of Loess under Highway Excavation

Xuanyu Yang [α] & Yaming Liu [σ]

ABSTRACT

Large-scale road construction in mountainous areas inevitably leads to numerous excavation slopes, particularly in the Loess Plateau, characterized by abundant ancient landslides and complex stratigraphy. Excavation-induced stress relief can easily reactivate these ancient landslides, posing significant threats to engineering safety. This study takes an ancient landslide in the Loess Plateau as a case example. Field investigations clarified the lithological characteristics of the strata. Indoor triaxial unloading tests were conducted to examine the unloading creep behavior of silty soil and clay located near the sliding zone. Finally, numerical simulations were employed to analyze the evolution process of landslide reactivation induced by excavation. The study revealed the following findings: (1) The primary factor inducing the landslide is the differential unloading creep behavior of silty soil and clay.

Silty soil readily reaches an accelerated creep state under unloading conditions, whereas clay remains relatively stable with smaller deformation. The creep behavior of the soil can be well described using the Nishihara model. (2) Comparison of two unloading stress paths showed that vertical stress unloading causes minor rebound deformation with minimal impact on overall deformation. In contrast, lateral stress unloading results in significant soil deformation, which is the main cause of the landslide. (3) During the landslide, there was an abrupt change in pore water pressure within the soil, which can be combined with deep soil deformation as a key indicator for monitoring and early warning of this type of landslide.

Author α: Shanxi Intelligent Transportation Research Co., Ltd, 030026, Taiyuan, Shanxi, China. Institute of Rock and Soil Mechanics, Chinese Academy of Sciences, 430071, Wuhan, Hubei, China. University of Chinese Academy of Sciences, Beijing, 100049, China. σ: Shanxi Transportation Technology Research and Development Co., Ltd, 030026, Taiyuan, Shanxi, China.

I. INTRODUCTION

The construction of highways in mountainous regions involves extensive excavation projects. Large-scale excavation can easily disrupt the original topography and geomorphology of the mountains, altering the initial stress state and subsequently inducing slope deformation and failure. The Loess Plateau, an important industrial and agricultural base in China, has a dense transportation network. In recent years, over 100,000 kilometers of roads have been constructed, involving extensive high-fill and deep excavation projects in mountainous areas. Due to the unique properties of loess and the diversity of geological layers, numerous landslides have occurred during construction (figure 1). Extensive research indicates that rainfall is the primary factor inducing loess landslides (Chang et al. 2021). In addition, excavation during the construction process also affects slope stability (Wang et al. 2014, Meng et al. 2021). Landslides during the construction process severely impact project progress, increase construction costs, and pose significant threats to the safety of engineering personnel.

(a) Jinyang highway landslide   (b) Lixi highway landslide

Fig. 1: Landslide because of excavation on Loess Plateau

The Loess Plateau exhibits typical stratification (Chen et al. 2024), resulting in the presence of various soil types within the same slope. The significant differences in the properties of these soils, combined with changes in stress states, lead to differential deformation, which is the intrinsic mechanical mechanism of landslides. Silty soil and clay are the most widely distributed soil types in the Loess Plateau. Due to their different origins, they exhibit significant differences in particle size, composition, hydraulic properties, and mechanical characteristics (Sun et al. 2024). However, these two soil types often appear as continuous layers. Once the external stress field changes, they are highly susceptible to differential deformation. Numerous studies indicate that loess landslides often exhibit significant creep characteristics (Chang et al. 2020, Lian et al. 2022, Wang et al. 2023, Duan et al. 2024). Compared to rock creep, soil creep deformation is more pronounced at the macroscopic level, resulting in larger deformations. Therefore, numerous fractures can be observed on slopes prior to landslide occurrence. Factors influencing soil creep behavior include not only the inherent properties of the soil but also external conditions such as water content, temperature, and stress. Water content alters the soil's microstructure, affecting its cohesion, internal friction angle, pore water pressure, and viscosity, thereby changing its mechanical behavior (Peng et al. 2022, Li et al. 2023, Duan et al. 2023, Guang et al. 2023).

Temperature indirectly affects soil properties by influencing soil water vapor migration (Kong et al. 2021, Xu et al. 2022, Sun et al. 2022). Stress state is a crucial external factor impacting soil creep behavior, encompassing stress history, stress path, and stress corrosion. In the research, factors such as pre-consolidation stress, loading paths, unloading paths, and cumulative damage of the soil were considered (Zhou et al. 2014, Pei et al. 2017, Yan et al. 2020). During highway excavation, the changes in the soil stress field under unloading conditions are the primary focus. The unloading path varies depending on the excavation method. Additionally, the Loess Plateau has a history of numerous ancient landslides, which are prone to reactivation under excavation influence (Yao et al. 2013, Zhu et al. 2022, Wu 2022). In summary, the excavation of slopes in the loess mountainous regions is characterized by diverse strata, climatic variations, and complex geological conditions. These factors determine the varied disaster mechanisms and failure modes, making it difficult to develop a unified landslide prediction model or method. Therefore, current landslide early warning systems primarily use rainfall as the main threshold.

In conclusion, rainfall is the primary factor inducing loess landslides. Thus, research on landslides triggered by highway excavation is closely linked to rainfall, with some studies also considering the effects of excavation unloading and construction vibration loads. The main research methods include numerical simulations, indoor model tests, and field case analyses (Zhang et al. 2020, Wang et al. 2022, Raouf et al. 2024). However, the majority of the Loess Plateau is located in a semi-arid climate zone, with rainfall

Study on the Landslide Caused by Difference Creep Behavior of Loess under Highway Excavation

concentrated between July and September. Extensive engineering practice has shown that landslides do not exclusively occur during the rainy season; they are also likely to happen in winter and spring (Wu et al. 2021, Xian et al. 2022). Therefore, studying the mechanisms and failure modes of non-rainfall-induced landslides is equally significant and can further enrich the landslide research system. As the period of maximum slope disturbance, the construction process is highly prone to landslides. However, there is relatively little focus on landslides during construction, especially research considering the differential unloading creep behavior of soils.

Therefore, this paper uses the reactivation of an ancient landslide in a silty-clay composite stratum during the construction period in the Loess Plateau as a case study. Through field investigations and laboratory tests, the differential creep behavior of silty soil and clay under different unloading paths was analyzed. Numerical simulations were conducted to invert the deformation of the landslide, proposing the corresponding failure mechanism and disaster evolution model. Based on the soil creep model, a stress attenuation-based landslide prediction model was developed. The research results can provide technical reference for related engineering projects and offer guidance for future studies.

II. LOCATION AND METHODS

2.1 Landslide Location and Characteristic

On December 1, 2022, a slope failure occurred on the Loess Plateau along the route of a highway under construction in Luliang City, Shanxi Province (111.44N, 37.08E), characterized by significant topographical relief. The landslide took place on an ancient landslide body, reactivated due to the impact of highway excavation. The sliding direction, influenced by the ancient landslide and unloading from excavation, developed towards the southeast. Arc-shaped cracks appeared at the rear edge of the ancient landslide, and feather-shaped cracks formed at the top of the excavated slope, indicating signs of reactivation of the ancient landslide. Additionally,

the extent of this landslide has expanded compared to the ancient landslide, indicating that excavation unloading induced new sliding. To investigate the historical disaster characteristics of this area, nearly 20 years of remote sensing images from Google Earth were obtained, as shown in Figure 2b. The images reveal that this area, located at a protruding section of mountain extension, has experienced multiple landslides in recent years, indicating it is an unstable region.

Therefore, it is hypothesized that the current landslide is related to local lithology. To verify this, cores were drilled at different locations of the landslide to obtain rock layer information at various depths, and a cross-section along the main sliding direction was drawn (Figure 2c). The cross-section shows the stratigraphy from top to bottom as follows: silty soil, clay, silty soil, clay, and bedrock. The upper silty soil is yellowish-brown, uniform in texture, and contains mica and oxides. The lower silty soil is impure, interspersed with silty clay. The upper clay is light red, with a rough surface, low ductility, and easily fragmented. The lower clay is reddish-brown, with a smoother surface and fractures within the cores.

The bedrock is mainly sandstone, brownish-yellow in color, with moderate weathering, and the cores appear as fragments.

The sliding zone of the ancient landslide is located at the interface between the lower clay and bedrock, while the sliding zone of the current landslide is within the lower silty soil. The overall slope is moving downward, exhibiting multiple segments of sliding, characteristic of a traction landslide (Figure 2d).
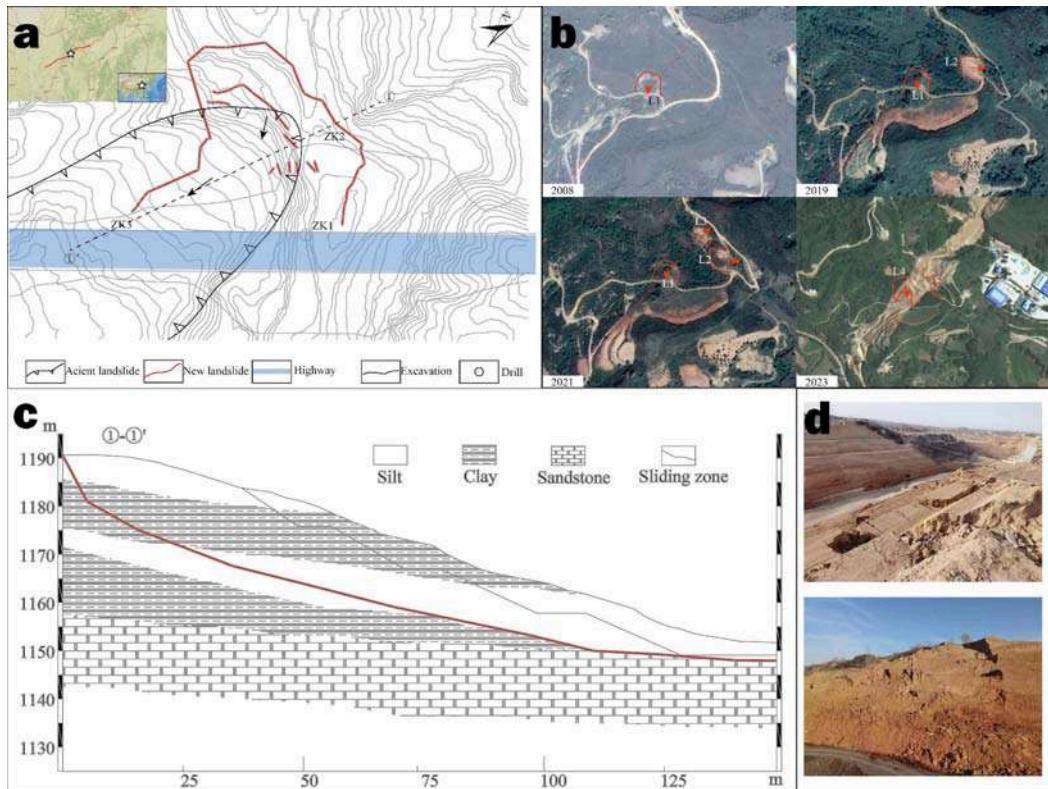
Fig. 2: Landslide Location and Characteristics

Numerous studies have shown that loess landslides are closely related to moisture. However, during the investigation, no significant increase in moisture content was observed near the sliding zone. To further clarify the relationship between moisture and the landslide, rainfall data for 2022 from the landslide location was analyzed. The results indicated that no rainfall occurred at the time of the landslide, which took place in winter when temperatures were low. According to Yang and Chen (2024), low temperatures can slow down moisture migration rates, reducing the likelihood of landslides. Therefore, it can be concluded that rainfall had a minimal impact on the occurrence of this landslide.
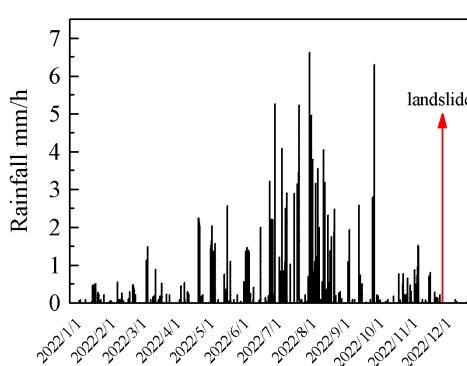
Fig. 3: Rainfall Distribution at Landslide Area

2.2 Materials and Methods

Based on the above analysis, the primary cause of the landslide is the change in slope stress state induced by excavation unloading. However, no landslides occurred on other sections of the same highway using the same excavation method. A comparative analysis revealed that the unique stratigraphic structure of this area might be an intrinsic factor leading to the landslide. Therefore, indoor tests were conducted on silty soil and clay

samples taken from near the sliding zone to further reveal the internal mechanisms by which the stratigraphy controls landslide deformation.

<p align="center">*Tab. 1* Basic properties of soil sample</p>

Sample	Dry Density ρ_d/(g/cm³)	Water Content w/(%)	Specific Gravity Gs	Liquid Limit w_L/(%)	Grain Size		
					>2mm	0.075~ 2mm	<0.075mm
Silt soil	1.63	10.5	2.53	18.6	0.3%	65%	34.7%
Clay	1.74	15.7	2.67	22.3	0%	37%	63%

To simulate the changes in stress state at the site, the indoor tests used a stress path method to study the deformation patterns of the two soil types under different unloading conditions. Soil samples collected from the site were dried and prepared into cylindrical specimens with the field-measured moisture content. First, the specimens were subjected to an axial pressure and confining pressure of 300 kPa for isotropic consolidation. After the deformation stabilized, the axial pressure (Path 1) and confining pressure (Path 2) were unloaded to 0 kPa at a rate of 10 kPa/min, while recording the axial deformation of the specimens.
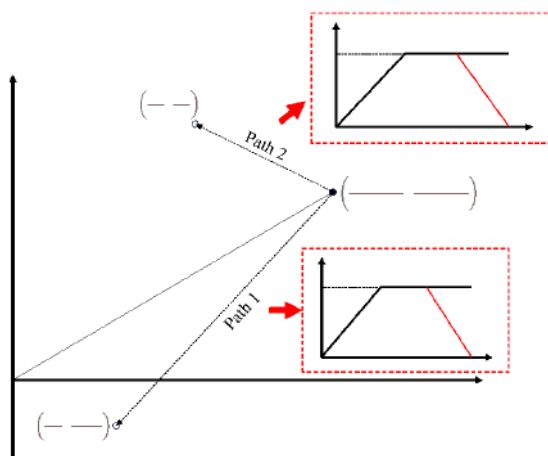
<p align="center">*Fig. 4:* Stress Path Laboratory Test Method</p>

III. RESULTS

3.1 Axial Strain Test Results

The experiment yielded axial deformations of the two soil types under different stress path conditions, as shown in Figure 5. During the experiment, the specimens were compressed, resulting in increased axial deformation, and vice versa, decreased axial deformation. Under stress path condition 1, during the initial isotropic consolidation phase, the axial strain of the soil rapidly increased and then stabilized. Under the same consolidation stress conditions, the axial strain of the silty soil was 14.5%, slightly higher than the clay's 12.5%. Both exhibited similar overall trends in deformation. As the axial stress was gradually unloaded while maintaining confining pressure, the axial strain gradually decreased by approximately 0.5%, indicating some degree of elastic rebound deformation in the specimens. This phenomenon manifests in engineering as slight rebound deformation of the soil due to unloading at the top of slopes, which is negligible and has a minimal impact on overall slope stability.

Under stress path condition 2, with constant axial stress and gradual unloading of confining pressure, significant differences in deformation were observed between the two soil types. Initially

(at 3000 seconds), a slight increase in axial strain of approximately 0.5% was noted. As unloading progressed, the silty soil exhibited a gradual increase in axial strain, while the clay-maintained stability in axial deformation. During the later stages of unloading (4000 to 4800 seconds), the silty soil experienced a sudden and pronounced increase in axial strain, accompanied by severe lateral deformation and eventual failure of the

specimen. Conversely, the clay specimen remained stable with minimal strain and no failure observed. This phenomenon illustrates how lateral excavation of slopes reduces lateral earth pressure, causing differential deformation in distinct strata, which can lead to significant deformation along weak planes of the slope and trigger landslides.

(a) Axial strain of stress path 1 (b) Axial strain of stress path 2
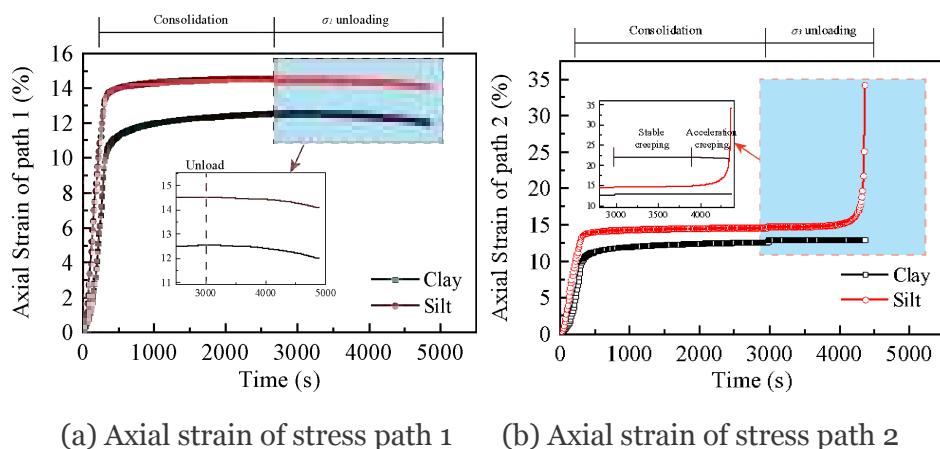
Fig. 5: Axial strain test results

The axial strain results clearly demonstrate the differential deformation behavior of different soil types under the same stress path. Both soil types exhibited a certain degree of creep deformation. The distinction lies in that the clay showed sustained steady-state creep, while the silty soil exhibited initial steady-state creep followed by accelerated creep in later stages. The Nishihara model effectively captures creep behavior and can be expressed as follows:

$$\varepsilon(t) = \begin{cases} \dfrac{\sigma_0}{E_1} + \dfrac{\sigma_0}{E_2}\left[1 - \exp\left(-\dfrac{E_2}{\eta_1}t\right)\right] & \sigma_0 < \sigma_s \\[2ex] \dfrac{\sigma_0}{E_1} + \dfrac{\sigma_0}{E_2}\left[1 - \exp\left(-\dfrac{E_2}{\eta_1}t\right)\right] + \dfrac{\sigma_0 - \sigma_s}{\eta_2}t & \sigma_0 \geq \sigma_s \end{cases} \quad (1)$$

Among formula (1), E_1, E_2 are elastic module; η_1, η_2 are dynamic viscosity coefficient; σ_s is the critical stress at which the sample undergoes plastic deformation and failure. These parameters can all be obtained through uniaxial compression tests. The specific testing procedures are not detailed here; the indicators for silty soil and clay are listed in Table 2.

Tab. 2: Strength parameters of soil

	E (MPa)	η (kPa·s)	σ_s (kPa)
Silt soil (w=10%)	18	0.0026	235
Clay (w=15%)	45	0.0035	561

By incorporating the parameters from Table 2 into the equation, theoretical solutions were computed and compared with experimental results, as shown in Figure 6. The comparison reveals a good fit between experimental and theoretical values, indicating that the model is capable of describing the creep deformation of both silty soil and clay.
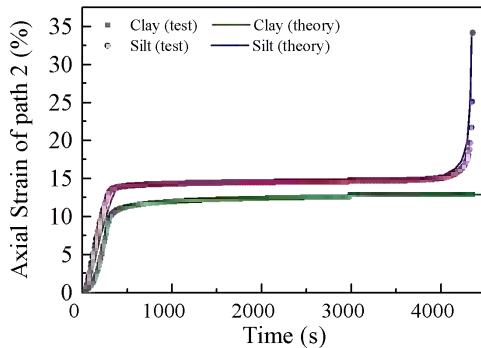
Fig. 6: Compare between Test and Theory Results

It is important to note that the Nishihara model assumes constant stress. However, in this experiment, the deviator stress gradually decreases, indicating a stress relaxation process. Stress relaxation is time-dependent, and thus the Nishihara model can be expressed in the form of Equation (2). When considering stress relaxation effects in three-dimensional space, the soil deformation surface is illustrated as shown in Figure 7. Stress relaxation leads to an increase in soil strain, and greater relaxation amplitudes result in earlier strain increases. By performing a second derivative of Equation (2), inflection points in the curve can be identified, which correspond to sudden changes in strain over time. This characteristic serves as a significant indicator for landslide prediction.

$$\varepsilon(t) = \begin{cases} \dfrac{\sigma_0(t)}{E_1} + \dfrac{\sigma_0(t)}{E_2}\left[1 - \exp\left(-\dfrac{E_2}{\eta_1}t\right)\right] & \sigma_0(t) < \sigma_s \\[3mm] \dfrac{\sigma_0(t)}{E_1} + \dfrac{\sigma_0(t)}{E_2}\left[1 - \exp\left(-\dfrac{E_2}{\eta_1}t\right)\right] + \dfrac{\sigma_0(t) - \sigma_s}{\eta_2}t & \sigma_0(t) \geq \sigma_s \end{cases} \tag{2}$$
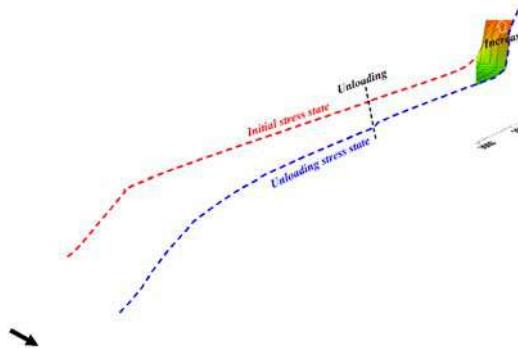
Fig. 7: Nishihara model theory solution by considering stress decrease

The above study mentioned that by performing a second derivative of the stress-strain-time model for critical soil layers, key deformation thresholds for slopes can be determined. Therefore, by solving the second derivative of Equation (2), assuming a homogeneous soil layer where the elastic modulus and viscosity coefficient are constant everywhere, the following results were obtained through calculations:

$$\frac{\partial^2 \varepsilon}{\partial t^2} = \frac{1}{E}\frac{\partial^2 \sigma_0}{\partial t^2} + \frac{1}{E}\frac{\partial^2 \sigma_0}{\partial t^2}(1 - e^{-\frac{E}{\eta}t}) + \frac{1}{E}\frac{\partial \sigma_0}{\partial t}(1 + \frac{E}{\eta}e^{-\frac{E}{\eta}t})$$
$$+ \frac{\sigma_0}{E}(1 - \frac{E^2}{\eta^2}e^{-\frac{E}{\eta}t}) + \frac{1}{\eta}\frac{\partial^2 \sigma_0}{\partial t^2}\cdot t + \frac{1}{\eta}\frac{\partial \sigma_0}{\partial t} \tag{3}$$

Assuming stress attenuation varies linearly with time, the first derivative of stress with respect to time represents the stress change rate, which is a constant value. Consequently, its second derivative is zero. Therefore, the above equation can be simplified to:

$$\frac{\partial^2 \varepsilon}{\partial t^2} = \frac{v}{E}(1 + \frac{E}{\eta}e^{-\frac{E}{\eta}t}) + \frac{\sigma_0(t)}{E}(1 - \frac{E^2}{\eta^2}e^{-\frac{E}{\eta}t}) + \frac{v}{\eta} = 0 \qquad (4)$$

By solving Equation (4), we can obtain the analytical solution for the critical failure time of the soil layer.

3.2 Pore Stress Results

The response characteristics of silt and clay to moisture can be distinguished through pore pressure test results. Clay exhibits strong water retention capabilities; during testing, moisture within the soil mass is difficult to expel, thus resulting in minimal variations in pore pressure.

Under Stress Path 2 conditions, there is a decreasing trend in pore pressure, yet it generally remains at stress levels from earlier consolidation stages. In contrast, silt shows more pronounced changes in pore pressure. Under Stress Path 1 conditions during the initial consolidation phase, pore pressure steadily declines as moisture is expelled. Upon unloading axial stress, the soil experiences rebound, increasing pore size, which slows down the drainage rate of pore water. This leads to a sudden increase in pore pressure, followed by a continued decrease. Under Stress Path 2 conditions, as the confining pressure is unloaded, the soil undergoes compression deformation under axial stress, resulting in smaller pores and accelerated drainage of pore water. Pore pressure rapidly decreases upon completion of unloading, gradually approaching zero, indicating loss of strength in the soil mass.

(a) Pore pressure of stress path 1   (b) Pore pressure of stress path 2
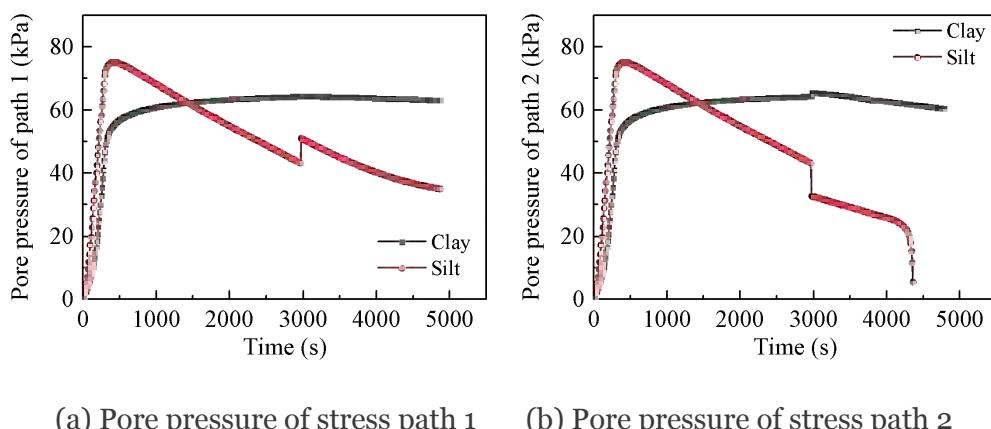
Fig. 8: Pore Stress Result

VI.   NUMERICAL SIMULATION

To further investigate the process of reactivation and deformation of ancient landslides induced by highway excavation, finite element numerical analysis was conducted on-site slopes. Based on 2-meter resolution contour lines from previous surveys, a three-dimensional numerical model was constructed. Different stratigraphic layers (as shown in Figure 9) were defined using borehole data, and soil and rock parameters were assigned based on field surveys and laboratory tests. Both clay and silt were modeled using the modified Cam-Clay constitutive model, while the bedrock was modeled with an elastic constitutive model. The model consisted of 23,071 nodes and 110,815 elements, with boundary displacement constraints applied to the perimeter and base. The numerical simulation was divided into two stages: consolidation and excavation. Initially, the model was subjected to the initial gravitational field, computed until reaching equilibrium to establish the initial stress field of the ancient landslide. Subsequently, displacements of all nodes were reset to zero while maintaining the existing stress state unchanged, simulating the excavation process and recording displacement changes until reaching equilibrium again. The excavation was conducted in stages to reflect engineering practice, divided into three phases. Monitoring points were strategically placed within the rock layers at the shear zones to observe landslide deformation characteristics throughout the construction process.
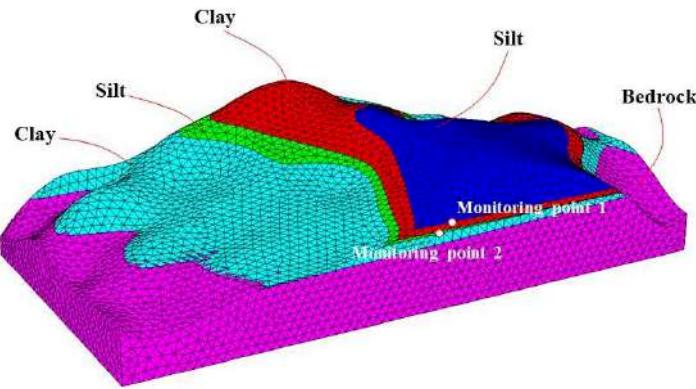
Fig. 9: Three-Dimensional Mesh Division Diagram of Landslide

Displacement contour maps for different stages were obtained through calculations (Figure 10). Under initial stress conditions, the overall deformation of the slope mass occurred towards the direction of the ancient landslide, with the deformation zone located on the ancient landslide mass. The maximum deformation occurred at the front edge of the landslide, reaching up to 2 meters. After the first excavation, lateral unloading resulted in a tendency for the slope to slide towards the open space, with topsoil displacement reaching a maximum of 2 meters.

Following the second excavation, where the excavation reached the clay layer, the slope did not exhibit significant deformation. Upon completion of the third excavation, continued displacement occurred in the silt layer at the top of the slope, with maximum displacements reaching up to 7 meters. Compared to the initial excavation phase, the displacement at the end of excavation exceeded three times, indicating a significant impact of excavation unloading on the landslide.
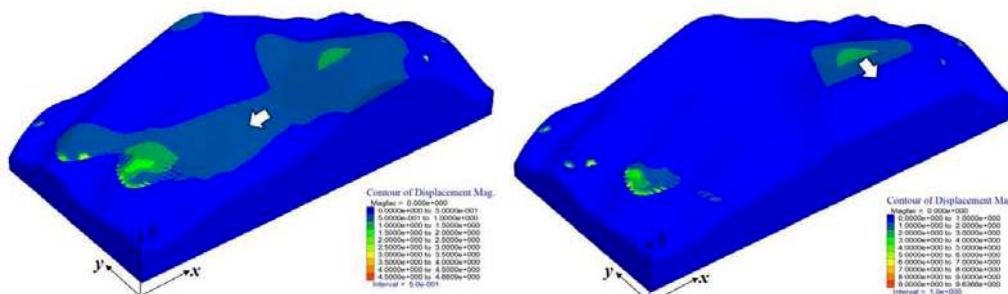
(a) Displacement contour of original slope (b) Displacement contour after first excavation
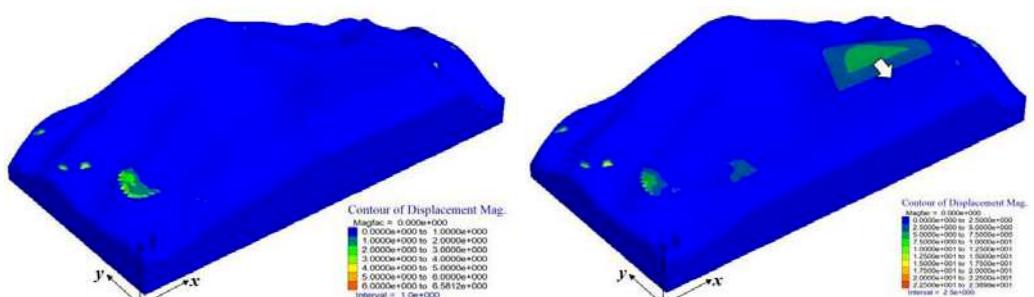
(c) Displacement contour after 2nd excavation (d) Displacement contour after 3rd excavation
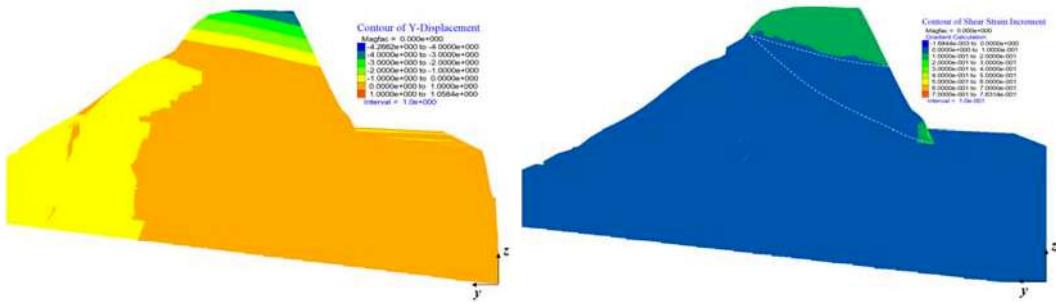
(e) Y Displacement contour of ①-①' profile (f) Shear strain increment of ①-①' profile

Fig. 10: Displacement Contour of Landslide

To further investigate the deformation characteristics of the soil mass within the sliding zone induced by excavation, monitoring of deformations in clay and silt located on the sliding zone was conducted in different directions. The monitoring results are shown in Figure 11.

In the x-direction, during the consolidation stage, silt exhibited greater displacement than clay, with maximum displacements of 0.125 meters for silt and 0.06 meters for clay upon completion of consolidation. This indicates that under the same stress conditions, silt is more prone to significant deformation, potentially leading to the formation of weak interlayers prone to sliding within the landslide mass. After consolidation, excavation simulation began. Following the first excavation, silt and clay exhibited opposite displacement directions, with clay showing larger displacements post-excavation, reaching up to 0.05 meters, while silt exhibited smaller displacements, maximum at 0.01 meters. The displacement curves showed two stages: stable deformation and accelerated deformation. Over time, clay's displacement gradually stabilized, whereas silt continued to show increasing trends. After the second excavation, soil displacement decreased compared to the first excavation, with clay reaching a maximum displacement of 0.025 meters and silt showing negligible deformation.

Following the third excavation, lateral constraints on the slope were completely lost, resulting in significantly increased soil displacements, with silt reaching a maximum of 0.05 meters and silt showing features of accelerated creep deformation.

In the y-direction, overall, clay exhibited smaller overall displacements compared to significant displacements in silt. After initial consolidation, silt exhibited a maximum displacement of 0.8 meters. Post-first excavation, silt moved towards the open face and continued to increase, reaching a maximum of 2 meters. After the second excavation, silt displacement decreased to 0.5 meters compared to the first excavation. Following the third excavation, silt displacement rapidly increased, entering a phase of accelerated deformation, with a maximum displacement of 6 meters.

In the z-direction, settlement deformation occurred in the soil mass, where overall, clay displacement was slightly lower than silt displacement. After the first excavation, silt continued to deform, reaching a maximum displacement of 1 meter, while clay initially deformed with a displacement of 0.75 meters, stabilizing subsequently. Following the second excavation, clay exhibited minimal deformation, while silt displaced 0.25 meters in the z-direction. With the third excavation, silt continued deforming, with a noticeable increase in the slope of the displacement curve, reaching a maximum displacement of 2.7 meters. Clay stabilized after reaching a displacement of 1.75 meters.

Based on the above calculation results, it is evident that during the excavation process, the silt layer near the sliding zone undergoes continuous deformation, whereas the clay layer reaches a stable state after deformation. Additionally, the displacement of clay is significantly lower than that of silt, which is a key factor contributing to the convergence of the calculation results. The

displacement curves indicate that silt exhibits distinct characteristics of unloading creep, including stable creep and accelerated creep processes. Overall, the numerical calculation results align with the patterns observed in indoor unloading creep tests.

(a) Displacement of x direction

(b) Displacement of y direction

(c) Displacement of z direction
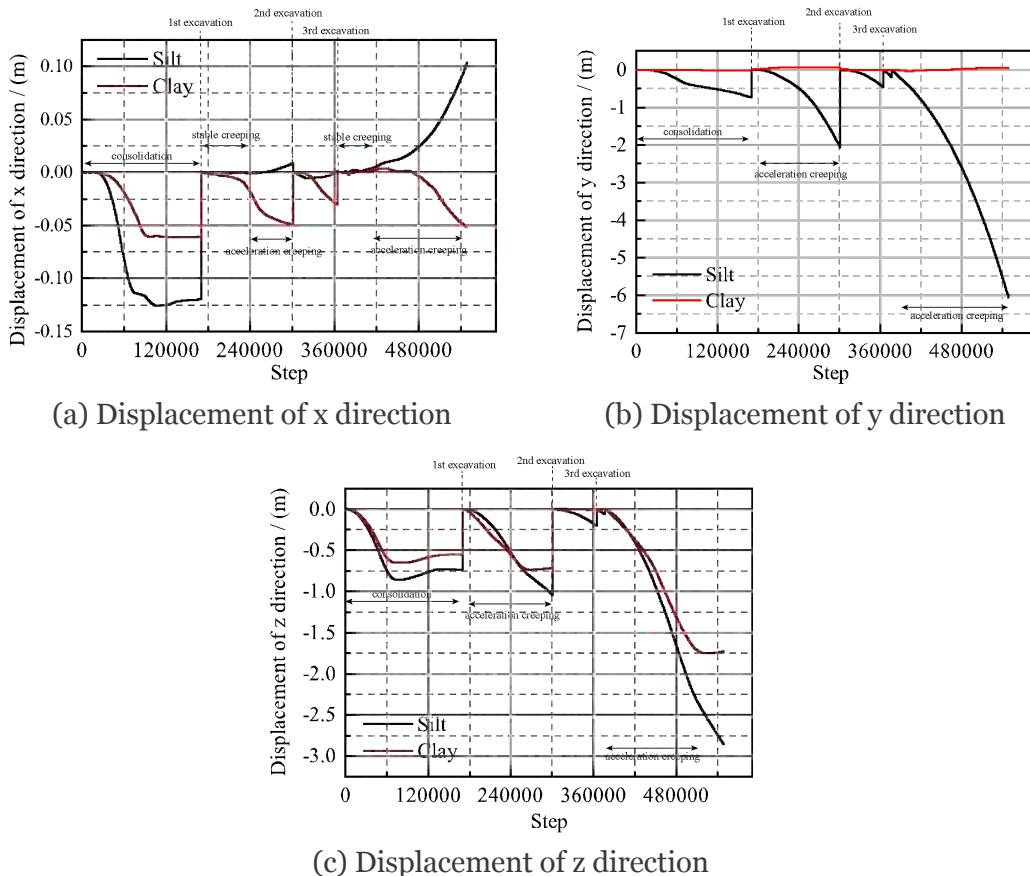
Fig. 11: Displacement Monitoring Results of the Soil Layers in the Sliding Zone

V. DISCUSSION

5.1 Mechanics Mechanism of Landslide under Excavation

During slope excavation, two types of unloading modes are encountered: axial stress unloading and lateral stress unloading, corresponding to Stress Path 1 and Stress Path 2 in this study, respectively. According to the above research, Stress Path 2 has a more significant impact on slope stability, primarily manifesting as deformation and instability induced by excavation unloading. In this paper, the clay and silt layers located in the sliding zone are relatively thin and close to the surface, resulting in their identical initial stress conditions (Figure 12). In practical engineering, excavation progresses downward in stages, initially dominated by axial stress unloading where the lateral stress on the soil remains unchanged. This leads to a gradual decrease in the Mohr circle radius, placing it below the strength envelope, thereby maintaining slope stability. As excavation approaches the sliding zone, lateral stress begins to decrease, transitioning the soil into Stress Path 2. The Mohr circle radius gradually increases, and when it exceeds the strength envelope of silt but not that of clay, the silt fails, resulting in deformation failure along the silt layer. Following slope instability, the stress field redistributes, with the energy accumulated in the upper clay layer slowly released, reducing the likelihood of further deformation failure. Eventually, this process forms a landslide primarily along the silt layer, establishing it as the main sliding zone.

London Journal of Engineering Research
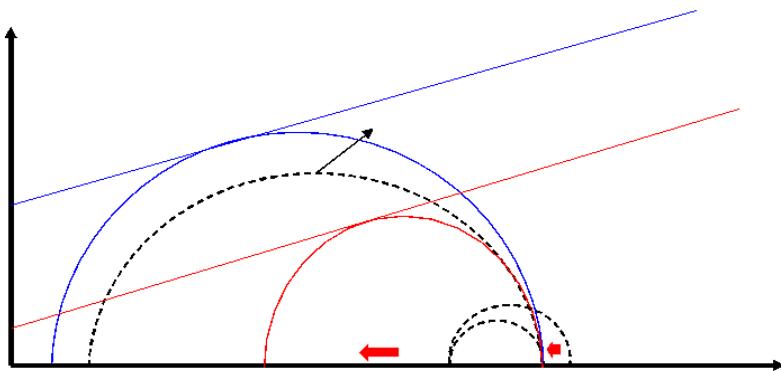
Fig. 12: Changes in Mohr Circles during Excavation Unloading

Furthermore, due to the significantly lower matrix suction of silt compared to clay, its water retention capacity is weaker. During unloading in Stress Path 1, characterized by axial stress release, the soil undergoes minor rebound deformation. At this stage, the lateral stress constraint becomes more pronounced, leading to increased pore water pressure. In Stress Path 2, characterized by lateral stress unloading, the soil undergoes compression deformation under axial stress. However, the loss of lateral constraint causes lateral expansion and dilation of the soil, resulting in increased pore space. As soil particles rearrange, they tend to lose water, leading to a decrease in pore water pressure. Clay, with its higher water retention capacity and larger elastic modulus, experiences less significant changes in pore water pressure.

It is noteworthy that significant time-dependent behavior occurs during deformation. After unloading is completed, immediate failure does not occur, which is closely related to the viscous resistance between soil particles. The dynamic viscosity coefficient of silt is 0.0026, while for clay it is 0.0035. A higher dynamic viscosity coefficient indicates a greater ability of the soil to resist time-dependent deformation. Therefore, time-dependent deformation is more pronounced in silt. The viscosity coefficient is not constant during stress changes but varies with the moisture content of the soil. As natural unloading creep occurs under drained conditions, the soil moisture content gradually decreases, leading to a reduction in the viscosity coefficient. This reduction is also a factor contributing to significant late-stage deformation.

5.2 Evolutionary Pattern of Landslide Triggered by Excavation

This study examines the multi-scale deformation characteristics of slope soil during the entire excavation process using a specific landslide as a case study. Initially, at the onset of excavation, the topsoil undergoes unloading, resulting in slight rebound deformation in the silt layer due to the unloading process. This redistribution of stress fields on the slope indicates initial stability (Figure 13a). As excavation progresses to the second terrace phase, reduced lateral stress in the rear silt layer causes it to extrude towards open space. Simultaneously, the front silt layer exhibits some rebound deformation under top unloading. Differential deformation patterns between the front and rear soils contribute to an uplift trend towards the slope's leading edge. Consequently, potential sliding zones become evident on the second terrace, accompanied by tension cracks appearing at the rear (Figure 13b).

Excavation through the silt layer induces lateral squeezing deformation in the front silt layer under lateral stress unloading, resulting in tension cracks and potential sliding surfaces on the first terrace (Figure 13c). Post-excavation, exposure of slope soil to atmospheric conditions triggers changes in soil properties influenced by rainfall and temperature variations. The critical interface depth between loess and the atmosphere, typically around 3 meters (Hou et al., 2019; Huang et al., 2019), is extended by the development of tension cracks, providing a basis for deep-seated sliding.

Following excavation, the silt layer remains unsaturated, with voids filled by water and air between soil particles. Evaporation of soil moisture due to changing dry climates leads to structural alterations among soil particles, forming interconnected voids within the soil matrix (Yang and Wang, 2020; Mu et al., 2023).

This substitution of water with air reduces the viscosity coefficient, accelerating soil creep deformation. Shear deformation along interconnected voids among soil particles leads to lateral expansion and vertical compression, observed macroscopically as squeezing creep deformation of the silt layer. Subsequently, this process induces the development of slope cracks, with stress concentrating at crack tips, thereby forming interconnected sliding surfaces and triggering deep-seated sliding (Figure 13d).
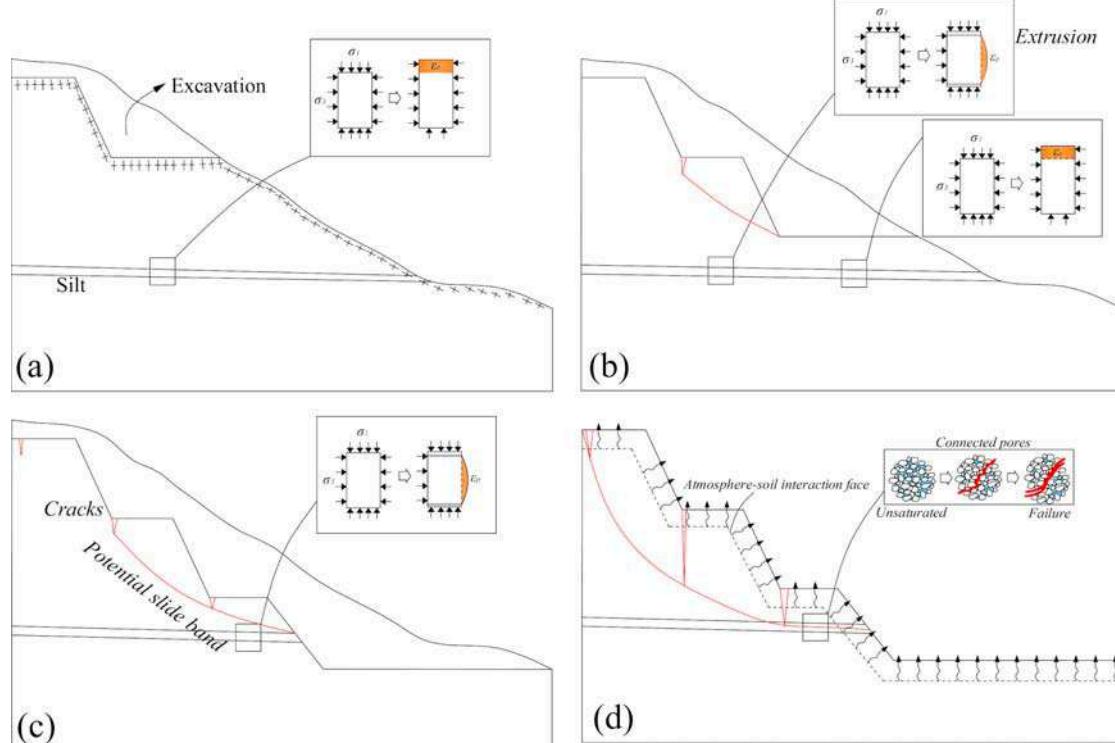
Fig. 13: Schematic diagram of landslide induced by excavation unloading

N engineering construction involving excavation and unloading of slopes containing weak interlayers, it is advisable to conduct comprehensive monitoring of dynamic deformations throughout the construction process. Concurrently, continuous on-site tracking of post-excavation crack development on the slopes is essential. Timely implementation of temporary support measures such as toe pressure, crack sealing, and anchoring reinforcement is recommended upon crack formation. After excavation completion, covering the slope's surface with geogrid can effectively mitigate water, vapor, and heat exchange between the soil and atmosphere. This practice helps maintain soil stability and reduces construction-related dust emissions, thereby improving on-site air quality.

IV. CONCLUSION

The study focuses on a landslide along a highway in the Loess Plateau, field surveys, laboratory experiments, and numerical simulations were conducted to investigate triggering factors and deformation mechanisms. The findings are summarized as follows:

1) The highway landslide was primarily triggered by excavation-induced reactivation of an ancient landslide, with the slip zone located within deep layers of silt. Differential soil

properties led to varying deformations, particularly with silt experiencing significant extrusion deformations under unloading stress paths, resulting in extensive deformations in the upper soil layers and triggering the landslide.

2) Two stress paths were identified during excavation: axial stress unloading and lateral stress unloading. Lateral stress unloading was identified as the primary cause of landslide occurrence. The Westergaard creep constitutive model, accounting for stress relaxation, effectively described soil deformation under unloading conditions.

3) Sudden changes in pore water pressure and soil deformation were critical precursors to landslide occurrence. For accurate prediction of landslides induced by excavation and unloading, monitoring pore water pressure changes in high-risk areas of the slope is crucial. This should be integrated with evaluations of soil elastic modulus, viscosity coefficient, critical plastic stress, and theoretical failure time to facilitate scientifically grounded early warnings.

ACKNOWLEDGEMENT

REFERENCES

1. Chang Zhilu, Gao Huanxiang,Huang Faming, et al. (2020) Study on the creep behaviours and the improved Burgers model of a loess landslide considering matric suction. Natural Hazards, 103(1):1479-1497.

2. Chang Zhilu,Huang Faming,Huang Jinsong, et al. (2021) Experimental study of the failure mode and mechanism of loess fill slopes induced by rainfall. Engineering Geology, 280, 105941: 1-16.

3. Chen Xuanyi, Xu Ling, Wei Xin, et al. (2024) Study on characteristics of microstructure variations along with the depth of taiyuan collapsible loess. Journal of engineer geology, 032(001):8-18. (In Chinese)

4. Duan G, Song F, Wang H, et al. (2024) Stability analysis of unsaturated loess slopes subjected to extreme rainfall incorporating creep effects. Computers and geotechnics, 169(May): 1.1-1.17.

5. Duan Zhao, Li Zhen-Yan,Wu Yan-Bin, et al. (2023) Mechanical and microscopic properties of soil according to the rate of increase in pore water pressure. Soil & Tillage Research, 225: 105530.1-105530.14.

6. Guang Li, Minggao Tang, Mingli Zhang, et al. (2023) Slope stability under the influence of irrigation and frozen stagnant water effect in Heifangtai. Bulletin of engineering geology and the environment, 82(7):254.1-254.18.

7. Hanxun Wang, Bin Zhang, Yadong Zhou, et al. (2022) Stability analysis of road slope cut in cemented conglomerate based on DEM, PSO, and GIM. Bulletin of engineering geology and the environment, 81(9):387.1-387.13.

8. Hou Xiaokun, Li Tonglu, Vanapalli Sai K, et al. (2019) Water percolation in a thick unsaturated loess layer considering the ground‑atmosphere interaction. Hydrological processes, 33(5):794-802.

9. Huang Laiming, Shao Ming'an. (2019) Advances and perspectives on soil water research in China's Loess Plateau. Earth-Science Reviews: The International Geological Journal Bridging the Gap between Research Articles and Textbooks, 199: 1-22.

10. Jun-Jie Wang,Yue Liang, Hui-Ping Zhang, et al. (2014) A loess landslide induced by excavation and rainfall. Landslides, 11(1):141-152.

11. Kong Jia-xu, Zhuang Jian-qi, Zhan Jie-wei, et al. (2021) A landslide in Heifangtai, northwest

of the Chinese Loess Plateau: triggered factors, movement characteristics, and failure mechanism. Landslides, 18(10):3407-3419.

12. Li Zhe, Zhao Jinpeng, Guan Chenhui, et al. (2023) A field test study on the effect of artificial rainfall on instability characteristics of loess slopes. Arabian journal of geosciences, 16(6): 1-5.

13. Lian B, Wang X, Zhan H, Wang J, et al. (2022) Creep mechanical and microstructural insights into the failure mechanism of loess landslides induced by dry-wet cycles in the Heifangtai platform, China. Engineering Geology, 300: 106589.1-106589.19.

14. Meng Zhen-jiang, Ma Peng-hui, Peng Jian-bing. (2021) Characteristics of loess landslides triggered by different factors in the Chinese Loess Plateau. Journal of mountain science, 18(12):3218-3229.

15. Pei Xiangjun, Zhang Xiaochao, Guo Bin, et al. (2017) Experimental case study of seismically induced loess liquefaction and landslide. Engineering Geology, 223: 23-30.

16. Peng Taixin, Chen Ningsheng, Hu Guisheng, et al. (2022) Failure mechanism of Dege landslide in western China, March, 2021: the loess interlayer and multiple water resources. Landslides, 19(9):2189-2197.

17. Qingyi Mu, Longlong Meng, Yanqian Shen, et al. (2023) Effects of clay content on the desiccation cracking behavior of lowplasti city soils. Bulletin of engineering geology and the environment, 82(8):317.1-317.12.

18. Raouf Arif, Feng Tugen, Zhang Kunyong, et al. (2024) Field and Numerical Investigation of Taihu Resort Cut Slope Failure in Suzhou, China. Applied Sciences, 14(7): 1-26.

19. S Zhang, X Pei, S Wang, et al. (2020) Centrifuge Model Testing of Loess Landslides Induced by Excavation in Northwest China. International journal of geomechanics, 20(4):4020022.1-4020022.18.

20. Sun Youbin, Lu Hongxuan, Zhang Zeke. (2024) New progress in quantitative reconstruction of paleoclimate changes in the Chinese Loess Plateau. Acta geological sinica, 098(003):1006-1023. (In Chinese)

21. Sun Zhijie, Yang Xuanyu, Zhao Ziyang, et al. (2022) Study on deformation characteristics of different angle loess slopes under wet-dry alternation. Arabian journal of geosciences, 15(12): 1-5.

22. Wang Haojie, Sun Ping, Ren Jian, et al. (2022) Reactivation mechanism and run-out processes of the Wangqi landslide induced by water leakage on April 30, 2022, in Tianshui City, Gansu Province, China. Landslides, 20(5):999-1011.

23. Wu Kanglin, Chen Ningsheng, Hu Guisheng, et al. (2021) Failure mechanism of the Yaoba loess landslide on March 5, 2020: the early-spring dry spell in Southwest China. Landslides, 18(9):3183-3195.

24. Wu Xiaohua. (2022) Study on Stick-Slip Characteristics of Loess-Bedrock Interface of Ancient Landslide. Shanxi Transportation Technology, 000(004):17-21.(In Chinese)

25. Xian Yu, Wei Xueli, Zhou Haibo, et al. (2022) Snowmelt-triggered reactivation of a loess landslide in Yili, Xinjiang, China: mode and mechanism. Landslides, 19(8):1843-1860.

26. Xu Panpan, Qian Hui, Zhang Qiying, et al. (2022) Response mechanism of permeability change of remolded loess to seepage parameters. Journal of Hydrology, 612(Pt.B): 128224.1-128224.13.

27. Yan Rui-Xin, Peng Jian-Bing, Zhang Jin-Yuan, et al. (2020) Static Liquefaction Capacity of Saturated Undisturbed Loess in South Jingyang Platform. Water, 12(8): 1-24.

28. Yang X., Chen Y. (2024) Characteristics and mechanism of landslides on highway landfill along Xiaolangdi Reservoir of the Yellow River: a case study. Natural Hazards. https://doi.org/10.1007/s11069-024-06607-z.

29. Yang Xuanyu, Wang Yanchao. (2020) Study on the surface particle distribution characteristics of silt with different moisture content. Arabian journal of geosciences, 13(1): 1-9.

30. Yao Hai-lin, You Hui-jie, Fan Yong-feng, et al. (2013) Study of sliding mechanism of Liujiaao loess landslide. Rock and soil mechanics, 34(1):182-188.(In Chinese)

31. Zhou Y F, Tham L G, Yan W M, et al. (2014) Laboratory study on soil behavior in loess slope subjected to infiltration. Engineering Geology, 183: 31-38.

32. Zhu Rongsen, Xie Wan-li, Liu Qiqi, et al. (2022) Shear behavior of sliding zone soil of loess landslides via ring shear tests in the South Jingyang Plateau. Bulletin of engineering geology and the environment, 81(6):244.1-244.15.

Towards an Epistemology of Structural Theory

I. González

ABSTRACT

This article summarizes, partly as a glossary and partly as a compilation, the main concepts involved in the theory of architectural structures. It contains a holistic arrangement of the theoretical foundations of the main components of materials mechanics and, above all, their interaction with architecture, in the exercise of the so-called structural calculation. In thematic literature, it is not easy to find all this information gathered in simple, plain language. Hence the importance of reviewing, in a relatively simple and quick reading, the principles that lead to the epistemology of structural theory.

Keywords: architecture material mechanics structures theory.

Classification: DDC Code: 624

Language: English

Towards an Epistemology of Structural Theory

I. González

ABSTRACT

This article summarizes, partly as a glossary and partly as a compilation, the main concepts involved in the theory of architectural structures. It contains a holistic arrangement of the theoretical foundations of the main components of materials mechanics and, above all, their interaction with architecture, in the exercise of the so-called structural calculation. In thematic literature, it is not easy to find all this information gathered in simple, plain language. Hence the importance of reviewing, in a relatively simple and quick reading, the principles that lead to the epistemology of structural theory.

I.   INTRODUCTION

Given the relative ease that cybernetic modernity provides, regarding the way of facing the participation of the structure in architecture, it is known of the enormous lack of theoretical foundations of said interaction, both in the professional and academic fields. In order to facilitate the acquisition of knowledge and the understanding of the structures, listed in the author's opinion, are the main qualities, grouped by the following titles:

1. Basic characteristics and qualities
2. Tools and properties
3. Resources
4. Mechanical classification
5. Management over time
6. Process and representation

II.   OBJECTIVES

- Based on stability, geometry and tolerable deformability, specify basic characteristics and qualities of the structural system.
- In attention to the quantitative analysis, both the internal and external efforts, as well as the materiality and its behavior, determine the measurement tools, based on their properties.
- Depending on cognitive availability, formulate solution strategies, through interpretation and construction of models.
- Classify the mechanical participation of the structural components that intervene in structural systems.
- Locate, in terms of the procedural moment, the appearance or management of the structural.
- Define the components of the process, as well as their representation, in order to clarify the tasks of the professional areas involved.

III.   METHODOLOGICAL DEVELOPMENT

3.1   Basic Characteristics and Qualities of the Structural System

Balance: Fundamental condition for a building to remain standing. (Thornton & Marion, 2004, 49) It is the ability of a body to remain in a state of rest or minimal displacement, in relation to a given position, as well as with moderate permissible movement, if applicable, with respect to the base of the object. (Tipos De Equilibrio 2024, n.d.) (see figure 1)

Of the multiple existing classifications, Figure 2 shows 5: static, dynamic, stable, indifferent and unstable. (see figure 2)

Static Balance: When they do not act, in any direction, alterations, accelerations, translations or rotations. Absence of movement of the body, as well as any type of rotation.

Dynamic Balance: The body tends to maintain the same posture, despite the action of all types of forces (external and internal).

Stable Balance: It occurs when the force that could have taken it out of its state of balance ceases. The body then returns to its original position.

Indifferent Balance: When the body maintains balance, even if it finds other positions.

Unstable balance: When, once the force that could have taken it out of its state of equilibrium ceases, the body cannot return to its original position of equilibrium.

Of the last three classifications, only stable equilibrium can be accepted in architectural structures.

Endurance: Characteristic that determines the mechanical stress capacity of the structural object. It could be said that it is a determining factor in terms of the resistance or support of a structural material (Francis, 1980, 15). Resisting is preventing rupture, even if the element suffers deformations generated by external demands and their internal repercussions.
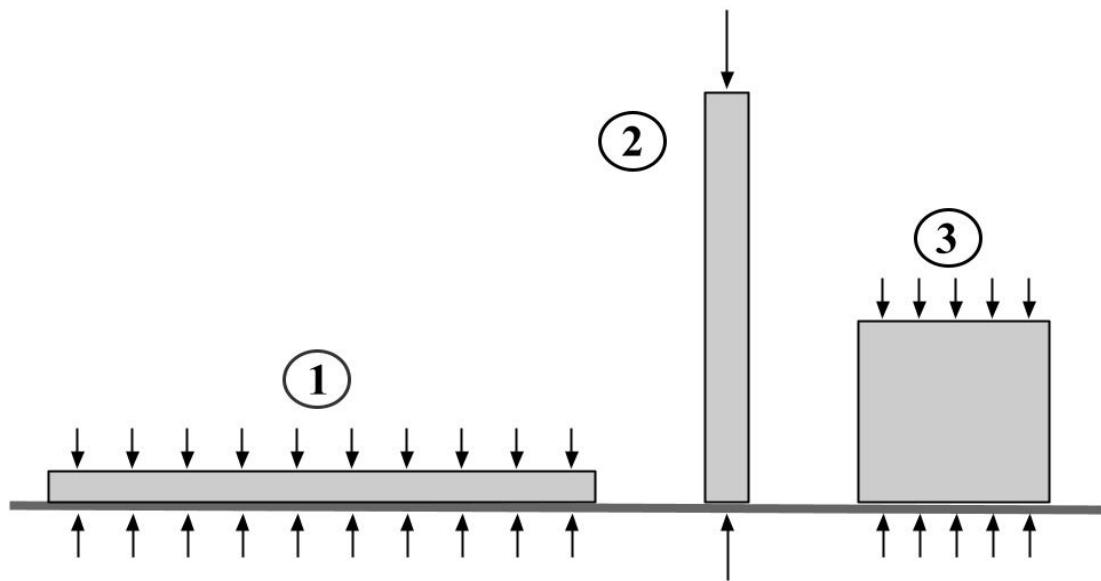
Figure 1: Considerations for rest (minimal mobility) and balance (moderate allowable movement). 1. Consideration of resting state. 2 Consideration of balance. 3. Intermediate classification
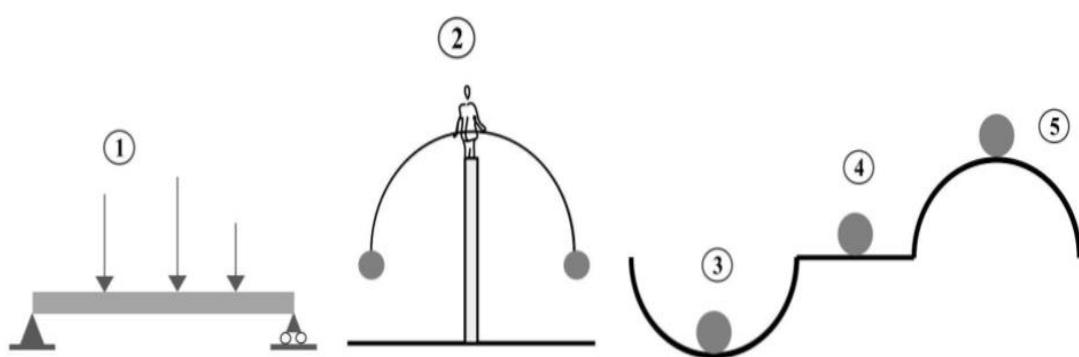
Figure 2: 5 types of balance or moderate permissible displacement. 1. Static. 2. Dynamic. 3. Stable ($\delta^2\varphi > 0$). 4. Indifferent ($\delta^2\varphi = 0$). 5. Unstable ($\delta^2\varphi < 0$). Nomenclature: δ is displacement or linear deformation and φ, slope (Magdaleno Domínguez, 2018, 55)

Towards an Epistemology of Structural Theory

3.2 Tools

Demands over Structures: It is convenient to know that the loads or requests acting on a structure can be modified gradually over time or change quickly from one moment to the next (Salvadori & Heller, 1998, 18). Based on the particular regulations, basically two types of demanding actions can be determined: permanent and variable.

Distribution of External Forces: Depending on the partition of the structural system, loads are applied to each and every element. These are aided by interpretations, both of their trajectories and the times in which they are executed.

Internal Flow of Efforts: All the loads participating in the structural elements move internally, driven mainly by gravitational attraction. This produces various deformations and behaviors that materials mechanics knows and interprets as quantitative data, which are the starting point for the numerical analysis of structural calculations.

3.3 Quantifiable Properties

The efforts depend on their materiality and geometric proportion. The deformations and various behaviors produced are interpreted as quantitative data, which contribute to the numerical analysis of structural calculations.

Compression: Effect of reduction or crushing of particles, produced by parallel collinear forces that tend to join.

Mechanical Tension or Traction: Effect of stretching or elongation of particles, produced by parallel collinear forces that tend to separate.

Flexion: The bending or arching in the same direction as the central longitudinal axis of the element produces compression on one side and tension on the other in the structural component.

Twist or Torque: The bending or bowing in the direction of the transverse axis of the element. Displacements of particles occur in every possible direction, so their quantification is highly difficult. In most calculation processes, overlapping coplanar models are assumed.

Stiffness (robustness) and Flexibility (slenderness): The materiality and fastening, as well as the geometric proportions of the components that make up both the system and each structural element, determine these properties, which contribute to evaluating the greatest or least possible displacement, prior to rupture or destruction. In Figure 3, both linear and angular rigidity are explained graphically (See Figure 3), while

Stiffness = force or moment necessary to produce a unitary movement (displacement or rotation) (Quispe Panca, 2015, 22) and

Flexibility = movement necessary to produce a unit force.

Most contemporary numerical calculations base their models and strategies on this pair of quantifiable concepts.

Elasticity and Plasticity: Both properties are ruled by very different laws, which have to do with the return or not to the original shape of the structural element, once the loads that caused its possible deformation have been removed. (See figure 4)

In the stress and strain diagram they are represented in technical language (see figure 5).

Ductility: Extension capacity, forming cables or wires, without breaking. (DF Complementary Technical Standards, 2023, 245)

Fragility: Property that bodies have of breaking easily when being hit.

In the regulation, the requirements to evaluate the limit states of brittle failure can be found, (Complementary Technical Standards DF, 2023, 507 and 510)

Malleability: The Ease of a material to be spread into sheets or plates. Hardness. It is the resistance that one material offers when being scratched by another.

Tenacity: Resistance offered by a material to breaking when hit. Fragile, therefore, would be the opposite of tenacious.

The Metal is Ductile and Tough: The concrete, fragile; glass is fragile and hard.

Notes towards a new modernity: The robustness of the system can refer to the mechanical circumstance of a property; It refers, then, to both a single (isolated) structure and a set or complex of these. In this sense, it is located within technical or engineering analysis, with the concepts related to resistance and rigidity, in a geometric context. (González Tejeda, 2021, 110)

With the understanding that slenderness can correspond to the fragile and robustness to the antifragile, it is possible to make some rearrangements, which could lay the foundations for new lines of research. (González Tejeda, 2021, 115) Slender area. The fragile and its possible failures.

Robust Area: The antifragile and possible ductile (or tenacious) failures (González Tejeda, 2021, 115).
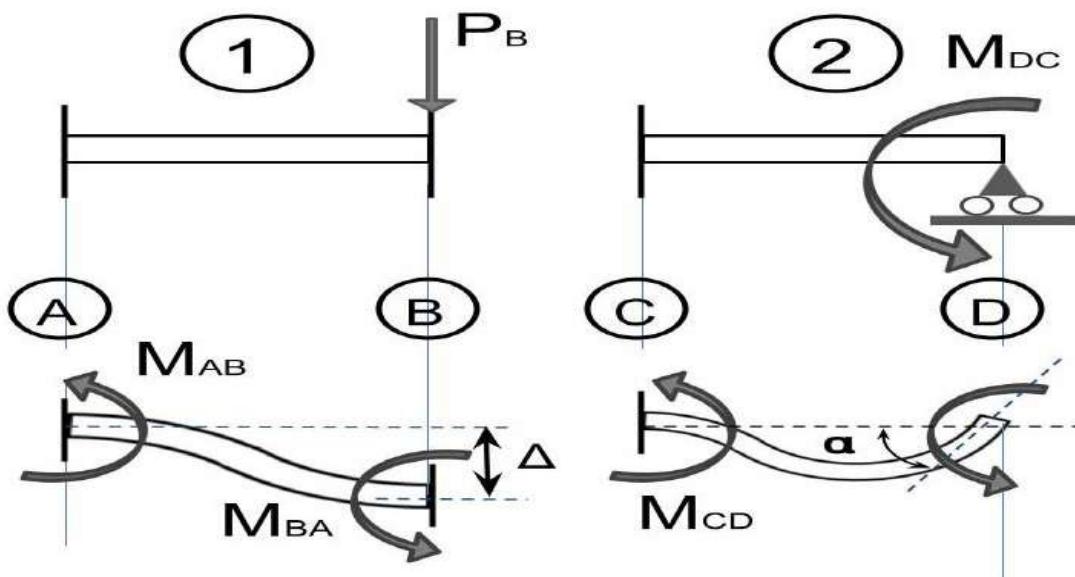
Figure 3: Graphic representation of 1. Linear stiffness (due to displacement) and 2. Angular stiffness (due to rotation). The force P_B produces a displacement Δ and the moment M_{DC} produces an angle α. In both cases, similar deformations occur, depending on the quantitative stiffness of the nodes, in which the materiality and the geometric proportion of the element (length and section) also intervene.
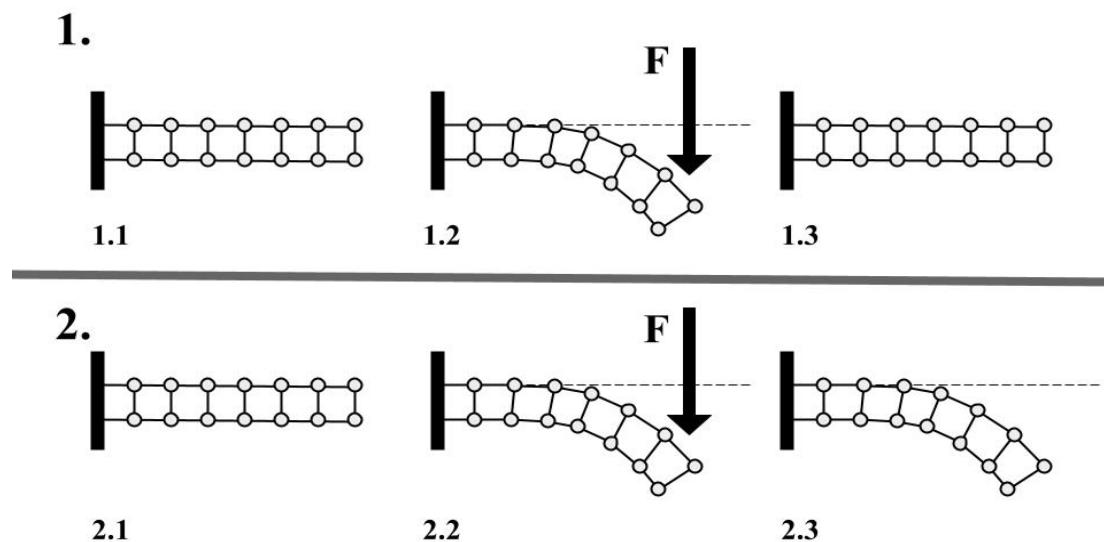
Figure 4: Case 1. Elastic behavior. 1.1 Element with its original shape. 1.2 Element deformed by application of force F. 1.3 Element that recovers its original shape, upon removal of force F. Case 2. Plastic behavior. 2.1 Element with its original shape. 2.2 Element deformed by application of force F. 2.3 Element that does not recover its original shape when force F is removed.
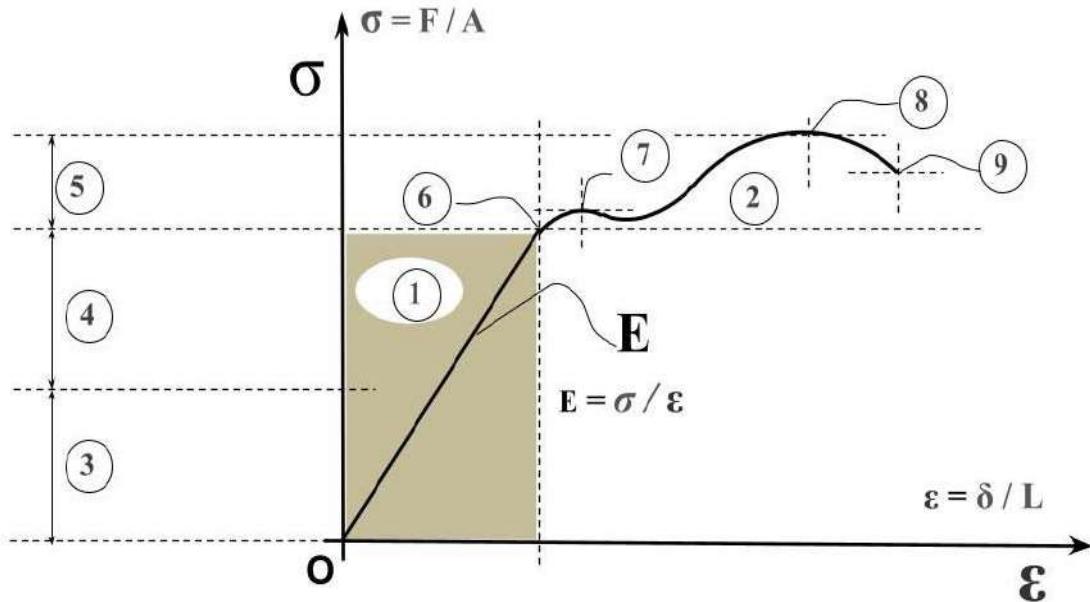
Figure 5: Diagram of stresses and unitary deformations. Nomenclature: σ=effort (PSI). F=applied force (P). A=area of the structural element (SI). ε=unit strain. δ=absolute deformation (I). L=length of the structural element (I). E = modulus of elasticity or slope of the elastic zone (PSI). 1. Elastic zone. 2. Plastic zone. 3. Allowable efforts (depending on the material). 4. Safety factor. 5. Plastic capacity. 6. Elastic limit. 7. Yield limit. 8. Ultimate resistance. 9. Breaking point. (González Tejeda, 2023, 17)

IV.   DiSCUSSION

4.1 Resources

Information: Important action in the discussion. The accumulation of knowledge and, above all, its ideal interpretation, will be determining factors in decision making, as explained below.

Strategies: The best path to manipulate the data must be established; each particular case requires specific responses. The choice of elastic and plastic methods, presumed of rigidity or flexibility, as well as coplanar or spatial interpretations, determine the construction of the mechanical and calculation models.

Model Construction: Based on the determined strategy, whether by choice or because regulations dictate it, we proceed to the configuration itself. It could be said that it is the starting point of any structural calculation process.

Coplanar configuration: Based on the "x", "y" and "z" axes. Each plane is solved independently to a certain extent, which then configures the spatial reality, creating superimpositions of effects.

Spatial Configuration: These are the models most attached to the construction of the truth.

Currently, these spatial interpretations are required to obtain increasingly accurate and precise results in a real environment.

4.2 Mechanical Components

The component parts of the structure result from the interpretation carried out, in such a way that these components could, in a given case, belong to all possible items. But, there are occasions, most of them, in which each of them performs more defined work towards one of the following classifications: load-bearing, transmitters and stiffeners (or auxiliary reinforcements).

Load-bearing: This is probably the most observed component of a structural system. It receives or carries all types of demands. There are those that directly support the loads and those that receive them in an inverse way.

Transmitters (Nodes or supports): They are the components that generally connect the load-bearing elements to each other. Its function is to restrict the degrees of freedom of the structure, appearing reactions in the direction of the inhibited movements. The main nodes are:

Towards an Epistemology of Structural Theory

London Journal of Engineering Research

free support, fixed support or articulation, embedded and stiff or continuous support.

Stiffeners or auxiliary reinforcements: Structural component, considered auxiliary, in principle, used to reinforce another element or to increase the safety of the entire system.

4.3 Temporality of Structures

During all processes, the correct behavior of the structural systems must be guaranteed, from a scaffolding or traveling crane, until the care to be observed in all objects in all types of repair.

Manufacturing plants and workshops: Although it is not strictly part of the construction process, it is important to establish that, as long as there is greater quality control in production, there will be greater safety in all aspects. Each production plant establishes its own measures regarding the manufacturing of solid components and fluid structural aggregates.

Transportation: This temporal concept has to do with the work itself, rather than with calculation processes, the hauling and elevations within the constructions represent many structural risks. Many times it is convenient to reinforce the structural elements for their transfer inside (and outside) the construction, especially in the elevations.

Stacking and Assembly: Bulks of granular materials and stone aggregates, for example, when stacked, should be considered as extra ephemeral loads for the supporting surface; so it must be reinforced. The same thing happens with overloads that occur during assembly, mainly due to sudden movements and even unexpected impacts.

Construction: Almost all literature, both constructive and structural, is focused on the process of the construction itself. The new construction is the ideal time where all the methods and interpretations presented here are applied.

Use and Occupation: Given the particularities of each structural system, a periodic review of both the use and the actions of all mechanical elements is necessary. On the other hand, it is considered

very important to deliver the buildings with an accompanying guide that explains the behavior of the structural elements themselves, as well as the protection and/or prevention areas, in case of any type of adversity or accident. Unfortunately, when the culture of prevention is lacking, check-ups, most of the time, are carried out after some physical tragedy has occurred.

Change of Destination: It is common that, in real estate purchase and sale operations, no relevance is given to the land uses defined by the authority; very important data that must have contributed to the calculation coefficients required by the regulations. Therefore, it is absolutely necessary that, when a building is used for purposes other than that for which it was created, a structural inspection should be carried out, which must consist of reviewing plans and reports and updating, given the case, certain structural characteristics.

Damage Repair: In emerging economy countries, the majority of existing buildings must be preserved. Properties are rarely demolished. Therefore, there must be an entire methodology to analyze the best way to deal with possible repairs, especially after the property has suffered any type of stressor, such as, for example, an earthquake, fire or flood. (González Tejeda, 2019, 41-60)

V. RESULTS

5.1 Abstraction of Structure in Architecture

Every architectural object subsists, thanks to its framework or skeleton. Structural systems fundamentally deal with the general architectural supports, that is to say, the essential parts that guarantee the mechanical stability of a property.

The structure is made up of a set of load-bearing, stiffening and stress-transmitting elements, which allow the stability of a building without excessive deformation.

The structure is not an isolated or independent problem. It can be abstracted to deepen and optimize its resolution, but without forgetting the interaction that is maintained, especially with the constructive and morphological requirements (González Tejeda, 2023, 11)

In addition to resolving the need to be mechanical, its function must encompass responses to the intended architectural objective and work together with all the areas involved to achieve this goal.

The "structural criterion" should not be based on the primitive definition of axes, generally orthogonal, determined to place vertical supports at each intersection; which, by the way, would be a very good geometric network, but NOT necessarily a structural framework.

For this reason, it is better suggested to use (and in fact, is used) the term structural composition or structuring, carried out based on the set of requirements that make up the architectural entity.

5.2 Process and Representation

Starting from the statement of requirements, every structural process consists of three substantial stages: 1. Structural composition or Structuring; 2. Mechanical analysis; and 3. Design or review. See figure 6 for the structural process roadmap. In the end, its results are poured into memories and plans.

Structuring: It can be defined as the way of accommodating and sizing load-bearing, stress-transmitting and stiffening elements within the architectural space and even within the boundaries.

The structuring responds to the architectural duty, with almost equal weighting as the mechanical one.

Structural composition goes far beyond a network or plot; It should always be in the company of architectural spatiality. So, structural logic in architecture does not necessarily correspond to mathematical or mechanical logics.

The objectives of structures in architecture have historically sought to reduce the sections of the participating elements and increase spans or spans between load-bearing elements. Architecture, however, throughout its entire existence, has expressed many more pretensions.

It is always sought that specialists offer bold solutions, through the procedures that technology and science have used or, where appropriate, through innovative proposals that show their effectiveness.

The structure can participate in two ways in the architectural proposal: A). As an essential form and B). As a mechanical assistant.

In most of the architectural work of cities, the structure is not shown, it is used only as a mechanical auxiliary.

When the structure, in some way, is the essential generator of the architectural form, the integration of skills during the project management process is essential, with extensive mechanical and constructive knowledge of the proposed techniques and materials.

The architectural form is the expected result of a specific process that involves all the requirements that participate in the corresponding program. With this, a meticulous search and investigation work is generated that must necessarily reach a morphological end.

For structuring (or structural composition) to be the guiding axis of the definitive form, time and effort must be allocated to the study of the mechanical behavior of materials and structural systems, as well as their interaction with the constructive and morphological requirements themselves.

That is why it is important to manage the information very well, as well as an appropriate methodology for resolving the architectural event.

Analysis: It refers to knowing the quantifiable effects (mainly stresses) that cause the loads or requests in the structural elements (bearings, stress transmitters and stiffeners), based on mechanical modeling.

The theoretical interpretations for the analytical resolution are found in the stress and strain diagram (see Figure 5).

In this diagram you can see Robert Hooke's Law of Elasticity (1635–1703) or Hooke's Law, which

Towards an Epistemology of Structural Theory

establishes the direct proportionality between force and longitudinal deformation, applied up to the elastic limit. (González Tejeda, 2023, 17).

Also represented is Thomas Young's (1773–1829) modulus of elasticity or Young's Modulus, which is the slope of the elastic zone.

On the other hand, it is known that the displacement coefficient of Siméon Denis Poisson (1781–1840) or Poisson's coefficient μ (the transverse linear displacement), is a percentage of the longitudinal linear unit strain $\varepsilon_T = \mu \varepsilon_L$

It is necessary to carry out gravity analysis, as well as sismic and eolic analysis, among others, in order to make or design the definitive structural elements, always for the integral case that is most unfavorable in the numerical calculations.

In order to guarantee the theoretical behavior of the systems, the applicable technical standards provide for safety factors, both in the resistance of the materials and in the load of the structural elements.

Design: This is the part of the process where epistemology is clearly manifested, by applying a

series of questions with their possible answers, in a holistic or joint context.

Basically, a comparison is made between the internal forces of the materials with those requested or produced by the loads, in order to adjust, if necessary, their measurements or physical proportions. As stated in the roadmap presented in Figure 6 (see Figure 6), the objective of the review is to ensure, in theory, that the materials proposed in the (pre-sized) models of a structural system resist.

Structural analysis and design are tasks carried out by specialists. The degree of difficulty experienced indicates the degree of specialization required.

It is important that architectural designers and builders in general should be familiar with the behavior and resistance of materials, in order to correctly interpret the results of the structural design, reflected in the corresponding plans.
With this activity the structural process itself ends.
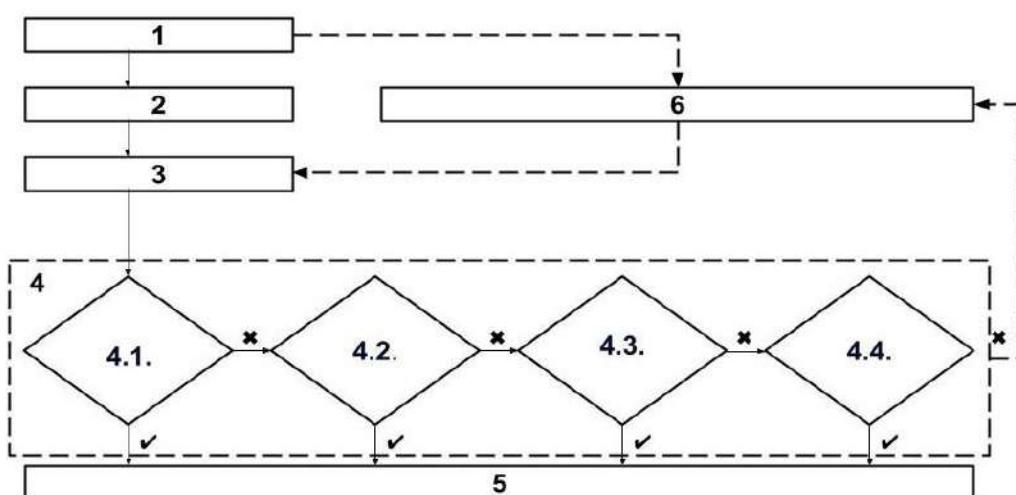
Figure 6: Structural process roadmap. 1. Structural requirements. 2. Structuring. 3. Mechanical analysis. 4. Design or review. 4.1. Admissible σ ≥ requested σ? 4.2. With additions or special hypotheses, does it comply? 4.3. With the increase in the resistance of the materials, does it comply? 4.4. With an increase in the section(s), does it comply? 5. Design completed. 6. Rethinking (alternative) of the structuring, rearrangement or structural composition. ✔ = meets. ✖ = does not comply.

Memoirs: As an analytical result of the structural calculation process, the corresponding report is prepared, which is generally supported or assisted

by graphic instruments that, in turn, are the basis of the structural plans and, where appropriate, workshop plans. The information used must be

recorded, mainly regarding the estimated models, both in the mechanical components and in the loads or demands and their transmission.

It is common for the authority to request this document to authorize construction.

Plans: One of the main products of the process is the set of structural plans.

Throughout the history of architecture, it has been agreed that the most used instrument in construction is, precisely, the plan. It serves to indicate the measurements and procedures for the execution of three-dimensional objects. It should contain limited graphic representations (with very well planned measurements) and, preferably, with scale drawings, as well as notes and specifications that provide all the basic and additional information that is necessary. The plans and calculation report must be presented with sufficient detail so that they can be reviewed in accordance with the requirements, scope and procedures established in current legislation. In the Mexican case, they must adhere to the Complementary Technical Standards for the Review of the Structural Safety of Buildings (Normas Técnicas Complementarias DF, 2023)

Every executive project must contain, in addition to the architectural plans, the general structural plans, as well as the workshop/assembly plans and the necessary detail plans.

The orthogonal drawing, as is known, is the main resource used to interpret architectural and, above all, structural components. In this way, the arrangement and magnitude of the physical elements that participate in the arrangements can be known.

There are two basic observation planes: The floor plan and the elevations. The latter, in turn, are subdivided into longitudinal and transverse elevations or sections. The floor plan is the ideal realization of a cut in space, perpendicular to the height line and parallel to the width and depth lines. It is a quite logical representation, since its drawing is an adequate approximation to the lines that are made on the real terrain or on a certain level of the building.

The structural plan, unlike the architectural plan, is generally carried out below (or inside) the represented level, in order to know the lower bearings up to said height (see figure 7). Thus, the load-bearing walls and beams, if applicable, that support the slab in question are known, the same of which its reinforcement or structural composition is also outlined, especially if it is composed of several materials.

Structural elevations generally represent elements developed in their entire length, with their respective reinforcements and/or stiffness reinforcements.

In the transversal case, in the same way, the interior of the 'cut' element is detailed, as far as possible, with all its fastening characteristics and with the notes and specifications that facilitate its understanding.

The plan is the two-dimensional object used in architecture, design and engineering, which is used to describe or diagram other objects, generally three-dimensional. It could be said that they become a kind of notebook of notes and images, whose objective is to graphically expose (to facilitate understanding) the organization and arrangement of the elements that are part of the spatial composition.
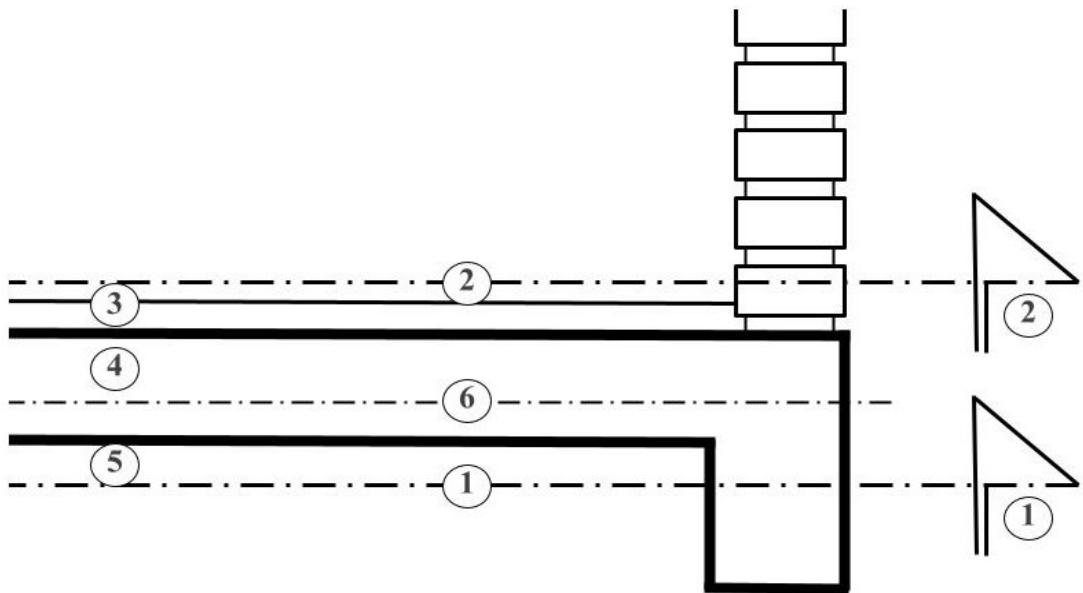
Figure 7: Approximate representation of the ideal horizontal cuts where the architectural plan and the structural level are located. 1. Structural level. 2. Architectural plan. 3. Finished floor. 4. Slab. 5. Low bed. 6. Another possible location of the structural level, inside the slab. (González Tejeda, 2023, 34)

VI.   CONCLUSIONS

The paper emphasizes the architectural nature of the structural activity, given that the ultimate goal of the mechanical analytical component of the process, without a doubt, it must collaborate in the architectural creation.

Bringing together most of the terms involved in the structural fact here, allows, on one hand, to appreciate the conceptual totality, even with the delimitation of their respective borders and, on the other, to holistically recognize each and every one of the elements participating in the wonderful concert that describe structural systems in architecture.

A text with these characteristics participates as an introduction to the adventure that the cognition of structural mechanics represents and encourages interested readers to delve deeper into those topics that, in their opinion, deserve greater depth and analytical development.

The initial classification of balance served to distance the imprecision and ambiguity of rest, with what is known in modernity as stability, while the graphic aids could contribute to clarify the borders.

The principle of resistance is present throughout the entire article, just as it should always be considered in any structural calculation process.

It has been explained that the loads or demands on the structures and their internal distribution in the structural system produce the accumulation of quantifiable properties, some described in this article, with sufficient content to allow the understanding of very simple systems up to those of high degree of difficulty.

Regarding resources or interpretation, it is hoped that the fact that modeling is vital for mechanical approaches and their numerical resolutions has been clarified. With respect to temporality, it is worth highlighting that this breakdown appears very infrequently in specialized literature, so it is extremely important to know about the existence of structural applications not only in the construction processes of new construction.

Finally, it is clear that the results obtained serve to organize the roadmap of the process, with all its possible implications, from the discipline itself of numerical calculations, to the deliverables, in descriptive reports and in general and detail plans.

Towards an Epistemology of Structural Theory

It is hoped that this compilation will be useful to professionals and scholars of the fascinating world of structures in architecture.

REFERENCES

1. Análisis estructural. (2012). Pearson.
2. Askeland, D. R., & Wright, W. J. (2016). Science and Engineering of Materials, SI Edition. Cengage Learning.
3. Engel, H. (1997). Sistemas de Estructuras: Sistemas Estructurais. Gili.
4. Francis, A. J. (1980). Introducing Structures: A Textbook for Students of Civil and Structural Engineering, Building, and Architecture. Pergamon Press.
5. González Tejeda, I. (2019). Sismos. Información práctica. Instituto Politécnico Nacional.
6. González Tejeda, I. (2021). Antifragilidad. Propuesta de aplicación convergente y vinculante, en procesos arquitectónicos para la gestión de riesgos sísmicos. Ciudad de México, México. Obtenido de Tesis UNAM: http://132.248.9.195/ptd2021/septiembre/08 15558/Index.html
7. González Tejeda, I. (2023). Análisis de estructuras arquitectónicas: Mecánica de materiales y análisis de sistemas hiperestáticos. Editorial Trillas.
8. MacDonald, A. J. (2001). Structure and Architecture. Architectural Press.
9. Magdaleno Domínguez, C. (2018). Análisis matricial de estructuras. Editorial Trillas.
10. Normas Técnicas Complementarias DF, 2023. (2023). Norma Técnica Complementaria sobre criterios y acciones para el Diseño Estructural de las Edificaciones. Retrieved October 27, 2024, from https://data.conse-jeria.cdmx.gob.mx/portal_old/uploads/gaceta s/b3c4f4ff37241d0a93cc6742a8b0bf2f.pdf
11. Quispe Panca, A. J. (2015). Análisis matricial de estructuras: introducción al método de elementos finitos. Editorial Macro.
12. Salvadori, M., & Heller, R. (1998). Estructuras para arquitectos. CP 67.
13. Thornton, S. T., & Marion, J. B. (2004). Classical dynamics of particles and systems. Brooks/Cole.
14. Tipos de equilibrio 2024. (n.d.). 10 tipos. Retrieved September 4, 2024, from http://10tipos.com/tipos-de-equilibrio/

This page is intentionally left blank

Evaluation of the Connection Line in Dissimilar Welding with Low Alloy and Low Carbon Wire using the Gmaw Process

Henrique Cechinel Casagrande, Gilson de March, Hadrian Martins, Anderson Daleffe, Joélson Vieira da Silva, Carlos Antônio Ferreira & Lírio Schaeffer

Prof. do Centro Universitário UniSATC

ABSTRACT

The use of welds with dissimilar characteristics is applied when it is necessary to join two materials that are considered metallurgically, mechanically, and chemically different. This study aims to understand the metallurgical effects on dissimilar joints between a low-carbon steel SAE 1015 and the AWS A5.36 E110C-MG low-alloy welding wire and the AWS A5.18 ER70S-6 low-carbon steel electrode, using the Gas Metal Arc Welding (GMAW) process. To characterize the bonding line between the materials, the chemical composition of both metals was evaluated through optical emission spectroscopy, and metallurgical characterization was carried out using an optical microscope, also assessing the Vickers microhardness. In order to map the thermal behavior, thermographic images were obtained during the welding process. In the microstructural evaluation of the bonding zone between the base material and the deposited material, the presence of Widmanstätten ferrite was observed, with a refined grain size microstructure in the weld region, which explains the increase in microhardness by approximately 24%.

Keywords: dissimilar welding. AWS A5.36 E110C-MG wire. widmanstätten ferrite. AWS A5.18 ER70S-6 wire.

Classification: DDC Code: 671.52

Language: English

Evaluation of the Connection Line in Dissimilar Welding with Low Alloy and Low Carbon Wire using the Gmaw Process

Avaliação da Linha de Ligação em Soldagem Dissimilar Com Arame de Baixa Liga e Baixo Carbono Utilizando o Processo Gmaw

Henrique Cechinel Casagrande[α], Gilson de March[σ], Hadrian Martins[ρ], Anderson Daleffe[ᴄᴏ], Joélson Vieira da Silva[¥], Carlos Antônio Ferreira[§] & Lírio Schaeffer[χ]

SUMMARY

The use of welds with dissimilar characteristics is applied when it is necessary to join two materials that are considered metallurgically, mechanically, and chemically different. This study aims to understand the metallurgical effects on dissimilar joints between a low-carbon steel SAE 1015 and the AWS A5.36 E110C-MG low-alloy welding wire and the AWS A5.18 ER70S-6 low-carbon steel electrode, using the Gas Metal Arc Welding (GMAW) process. To characterize the bonding line between the materials, the chemical composition of both metals was evaluated through optical emission spectroscopy, and metallurgical characterization was carried out using an optical microscope, also assessing the Vickers microhardness. In order to map the thermal behavior, thermographic images were obtained during the welding process. In the microstructural evaluation of the bonding zone between the base material and the deposited material, the presence of Widmanstätten ferrite was observed, with a refined grain size microstructure in the weld region, which explains the increase in microhardness by approximately 24%.

Keywords: dissimilar welding. AWS A5.36 E110C-MG wire. widmanstätten ferrite. AWS A5.18 ER70S-6 wire.

Author α: Mestrando em Engenharia Metalúgica.
σ ρ: Prof. do Centro Universitário UniSATC.
ᴄᴏ: Graduando em Eng. Mecânica.
¥: Prof. do Centro Universitário UniSATC.
§: Prof. do Centro Universitário UniSATC.
χ: Prof. do Centro Universitário UniSATC. Professor da Universidade Federal do Rio.

I. INTRODUÇÃO

A união entre materiais é uma prática muito comum em diversos seguimentos e atividades industriais, contudo, há setores como petroquímicos, plantas eólicas e reatores nucleares que necessitam de soldagem com materiais de diferentes características [1] [2].

Adotando esses conceitos, tem-se tornado comum estudos com soldagem em aço carbono utilizando arame de aço inoxidável, aplicando-se essa técnica em situações onde há locais que sofrem com corrosão e umidade, por exemplo, na indústria petroquímica [1] [2] [3] [4].

No entanto, quando realizado o processo de soldagem, as propriedades do material de base são alteradas devido as temperaturas de fusão, que ocorre com alto ciclo térmico de soldagem, o que resulta em mudanças microestruturais na zona de ligação (ZL) e na zona termicamente afetada pelo calor (ZTA) [1] [5].

Com a soldagem dissimilar, tem-se oportunidades promissoras relacionadas ao design dos produtos com diferentes combinações bimetálicas, capaz de aproveitar com efetividade as propriedades e características únicas de cada material [2] [6].

A soldagem de metais dissimilares tem sido cada vez mais adotada em diversos setores para aprimorar a funcionalidade e a eficiência

London Journal of Engineering Research

estrutural. Para obter juntas soldadas de alta qualidade e sem defeitos, é fundamental compreender de forma abrangente as inter-relações entre as alterações microestruturais causadas pela soldagem e as características de desempenho do material, especialmente suas propriedades mecânicas [7].

Pesquisas mostram que a soldagem a arco elétrico a gás (GMAW) com transferência de curto-circuito é eficaz para unir aços de baixo carbono e martensíticos em aplicações automotivas [8].

A interface entre materiais diferentes em juntas soldadas é frequentemente a região mais crítica devido à presença de fases duras perto da linha de fusão. Procedimentos de soldagem adequados, podem ajudar a minimizar problemas de fragilização da junta [9]. No geral, a soldagem de materiais diferentes oferece vantagens em várias aplicações, mas requer consideração cuidadosa das propriedades do material e técnicas de soldagem para garantir a confiabilidade da junta e a resistência mecânica.

II.   MATERIAIS E MÉTODOS

A seguir serão apresentados os materiais utilizados nessa pesquisa e os métodos para preparação e ensaios das amostras.

2.1 Soldagem das Chapas

As peças foram unidas em um único passe, com junta de topo e passe raiz, conforme pode ser observado na Fig. 01, na versão utilizando o eletrodo AWS A5.18 ER70S-6 e eletrodo AWS A5.36 E110C-MG.
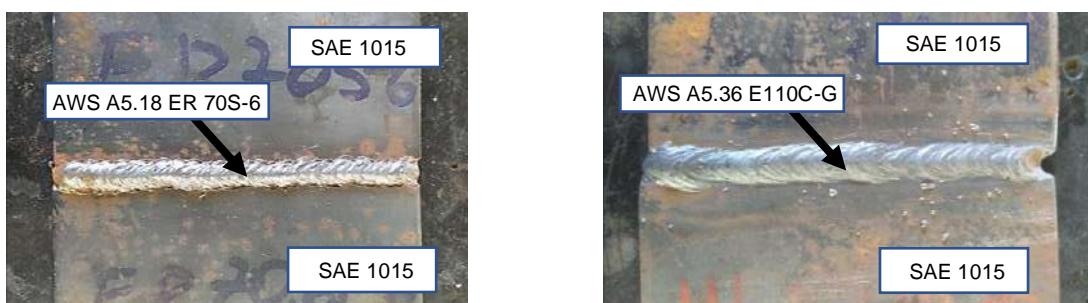
Fonte: Do autor

Figura 1: União das peças por solda

2.2 Espectrometria De Emissão Óptica

Para caracterização química das amostras utilizou-se o espectrômetro da fabricante BRUKER modelo Q2 ION. No ensaio em questão, foi utilizado potência de 400 Watts por um período de 30 segundos. Salienta-se o ensaio em triplicata para validação do método.

A Tab. 1 traz os resultados obtidos para caracterização química do arame AWS A5.36 E110C-MG. Conforme detalhado, este material é empregado para soldagens de aços de baixa liga, com um valor de aproximadamente 0,567% para o elemento cromo, bem como 0,386% para molibdênio.

Tabela 1: Análise química AWS A5.36 E110C-MG

Elementos:	Quantidade em massa (%):	Referenciado [10]
Carbono (C)	0,094	0,07
Silício (Si)	0,359	0,40
Manganês (Mn)	1,499	1,40
Fósforo (P)	0,013	<0,025
Enxofre (S)	0,008	<0,025
Cromo (Cr)	0,567	0,50
Molibdênio (Mo)	0,386	0,40

Níquel (Ni)	1,782	2,20
Cobre (Cu)	0,007	-
Ferro (Fe)	Bal.	Bal.

Desta forma, conforme o fabricante e norma AWS A5.36, o arame em estudo fica próximo ao recomendado. Salienta-se o baixo teor de carbono que compõe este arame [10] [11].

A Tab. 2 traz os resultados obtidos para o arame de soldadura AWS A5.18 ER70S-6.

Tabela 2: Análise química AWS A5.18 ER70S-6

Elementos:	Quantidade em massa (%):	Referenciado [12]
Carbono (C)	0,097	0,06 − 0,15
Silício (Si)	0,450	0,8 − 1,15
Manganês (Mn)	0,898	1,4 − 1,85
Fósforo (P)	0,014	<0,025
Enxofre (S)	0,013	<0,035
Cromo (Cr)	0,023	0,15
Molibdênio (Mo)	0,013	0,15
Níquel (Ni)	0,026	0,15
Cobre (Cu)	0,102	0,50
Ferro (Fe)	Bal.	Bal.

Conforme pode ser observado, os valores de silício (Si) e manganês (Mn) estão abaixo do recomendado conforme norma. Entretanto, este arame fica com características próximas do arame ER70S-3.

A Tab. 3 detalha a composição química para o material de base. Ressalta-se o uso deste material devido à alta demanda de consumo na indústria, como no setor civil [14], construções estruturais [15], entre outros

Tabela 3: Análise química SAE 1015

Elementos:	Quantidade em massa (%):	Referenciado [13]
Carbono (C)	0,150	0,13 − 0,18
Silício (Si)	0,017	-
Manganês (Mn)	0,454	0,3 − 0,6
Fósforo (P)	0,0098	0,04 - 0,05
Enxofre (S)	0,0096	-
Cromo (Cr)	0,013	-
Molibdênio (Mo)	0,0088	-
Níquel (Ni)	0,011	-
Cobre (Cu)	0,0051	-
Ferro (Fe)	Bal.	Bal.

Fonte: Do autor (2024)

Os valores dos elementos químicos para o material de base SAE 1015 ficaram conforme indicado pela norma, exceto para o fósforo (P), que apresentou um valor inferior.

2.3 Soldagem e aquisição de dados

Para soldagem das amostras foi utilizada a máquina de soldagem da marca IMC modelo

DIGplus A7, paralelamente foi feito uso de uma ferramenta de aquisição de dados denominada SAP 3SR.

A Tab. 4 traz os parâmetros utilizados para soldagem dos arames em estudo.

Tabela 4: Parâmetros de Soldagem para Arame ER70S-6 e E110C-MG

Variável:	ER70S-6	E110C-MG
Tensão (V)	18,5	18,9
Corrente (A)	165	161
Vazão do gás (L/min.)	16	16
Velocidade do arame (m/min.)	4,5	4,4
Potência (kw)	3	3
Argônio (%)	85	85
Dióxido de carbono (CO_2) (%)	15	15

2.4 Microdureza Vickers

A fim de se obter os dados referente a caracterização mecânica, foram realizados ensaios de microdureza Vickers, utilizando o microdurômetro da marca SHIMADZE®, modelo HMV-2TADW, com cargas de 4,903 Newtons para ambos os arames. O tempo de aplicação foi de 10 segundos, com um total de 15 indentações. A Fig. 2 demonstra a estratégia do ensaio de microdureza Vickers, onde iniciou- se a endentação no metal de base (SAE 1015), na sequência passando na zona termicamente afetada pelo calor até chegar na região de soldagem.
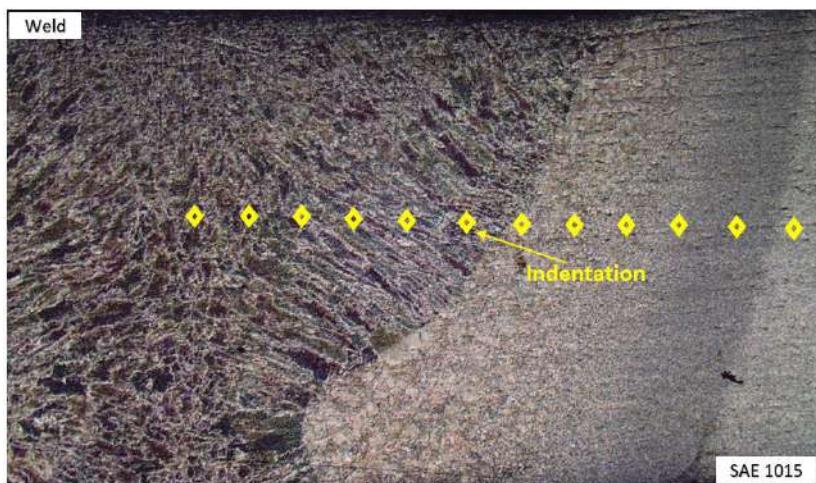
Fonte: Do autor

Figura 2: Estratégia do Ensaio de Microdureza Vickers

2.5 Câmera Termográfica

Durante o processo de soldagem, as temperaturas de trabalho podem variar dependendo das condições de deposição e do ambiente. Para controlar o processo e analisar as propriedades mecânicas, foi optado por monitorar a temperatura durante a deposição do material. A coleta de dados foi feita por meio de uma câmera termográfica, possibilitando a análise das informações capturadas, como ilustrado na Fig. 3 que mostra a peça em soldagem com destaque para a poça de fusão.
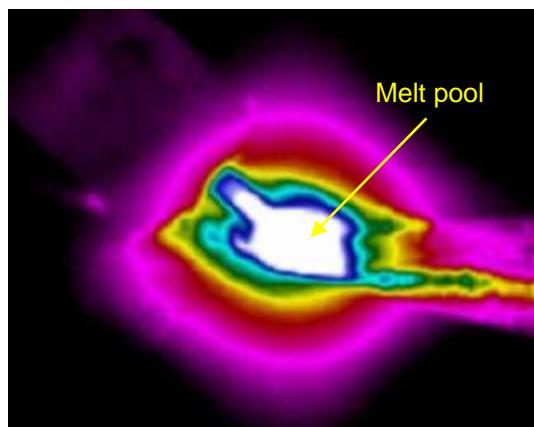
Figura 3: Avaliação Térmica da Poça de Fusão no Momento da Soldagem

Dessa forma para a aquisição da temperatura durante o processo de solda, foi utilizada uma câmera termográfica OPTRIS, modelo PI 08M, com capacidade de capturar imagens térmicas na faixa de 575 a 1900 ºC, permitindo monitorar e registrar as variações de temperatura durante o processo de solda.

Os pontos de medição de temperatura iniciaram na poça de fusão e seguiram em sentido linear em direção a soldagem.

2.6 Metalografia

Para realizar o ensaio de metalografia foi utilizado um microscópio Olympus modelo SC30, seguindo a norma ABNT NBR 15454. O ácido utilizado foi o Nital com 2 %. Para o arame de soldadura AWS A5.36 E110C-MG foi adotado o tempo de 10 segundos de ataque químico, e para o arame AWS A5.18 ER70S-6 foram considerados 5 segundos de ataque ácido.

III. ANÁLISE DOS RESULTADOS

A seguir serão discutidos os resultados obtidos com essa pesquisa.

3.1 Análise Metalográfica Junta Soldada Com Arame de Baixo Carbono ER70s-6

A Fig. 4 demonstra a linha de ligação entre material soldado ER70S-6 e aço SAE 1015.
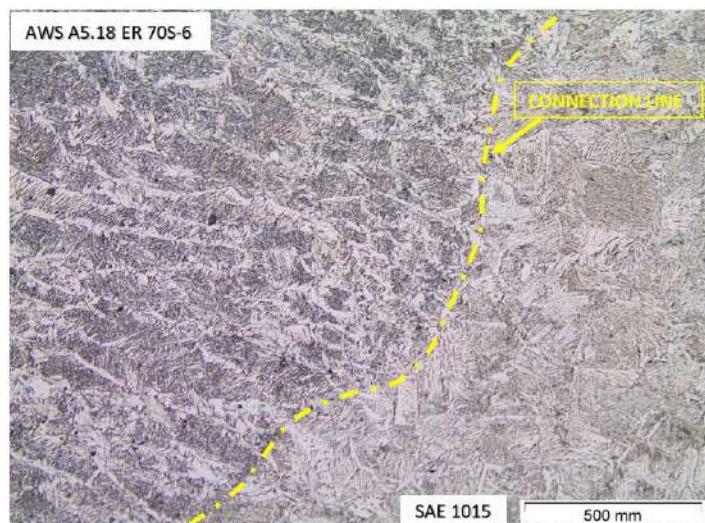
Figura 4: Metalografia da linha de ligação entre aço SAE 1015 e arame de soldagem AWS A5.36 ER70S-6

Evaluation of the Connection Line in Dissimilar Welding with Low Alloy and Low Carbon Wire using the Gmaw Process

A Fig. 5 detalha a linha de ligação e destaca a estrutura presente na região da solda, que é constituída de ferrita de Widmanstätten (FW).
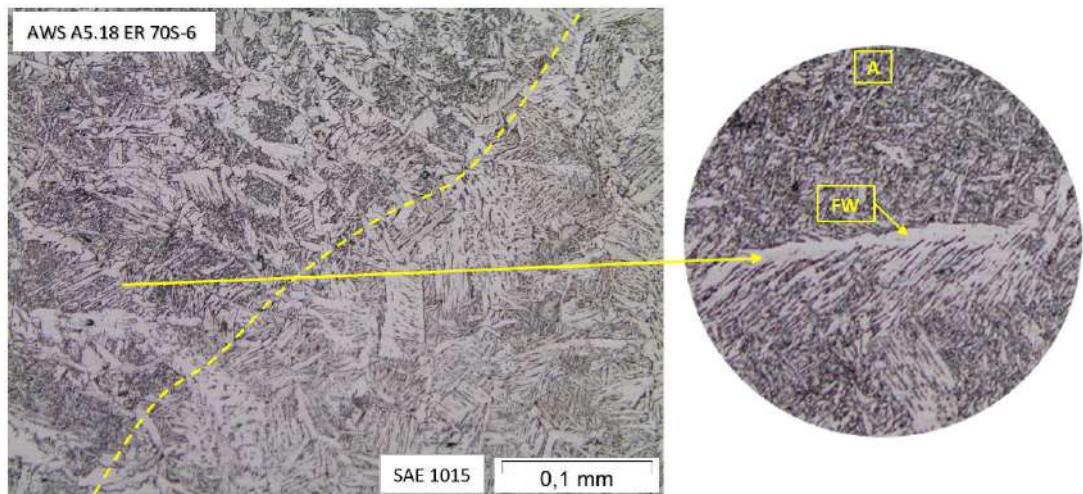
Figura 5: Ferrita de Widmanstätten (FW) Na Região de Solda

3.2 Análise Metalográfica Junta Dissimilar com arame de baixa liga AWS A5.36 E110C-MG

A Fig. 6 traz a soldagem do arame de baixa liga AWS A5.36 E110C-MG. Nota-se que há diferença significativa entre a região de solda e o material de base. O material adicionado possui tamanho de grãos finos, o que aumenta a dureza do material. Já a região que foi afetada pelo calor, é constituída de ferrita de Widmanstätten (FW).
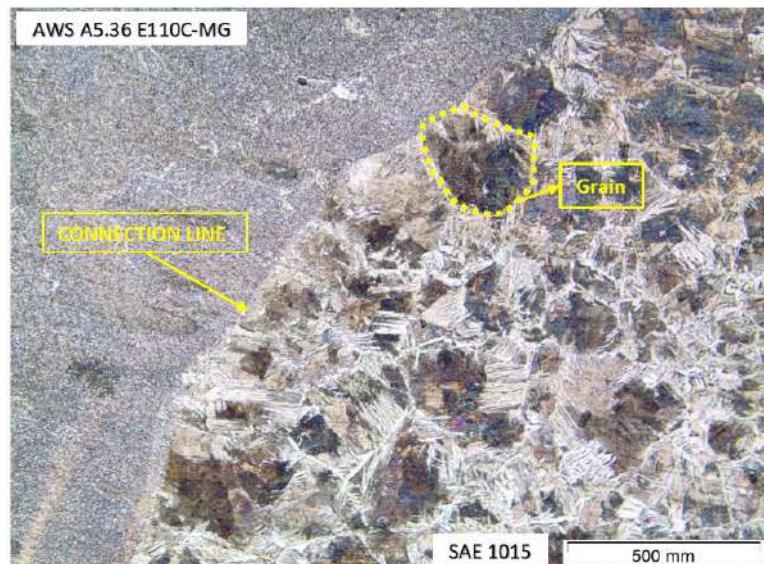
Figura 6: Região de ligação entre material soldado AWS A5.36 E110C-MG, e material de base SAE 1015

A Fig. 7 demonstra a ferrita de Widmanstätten (FW) na zona termicamente afetada pelo calor.
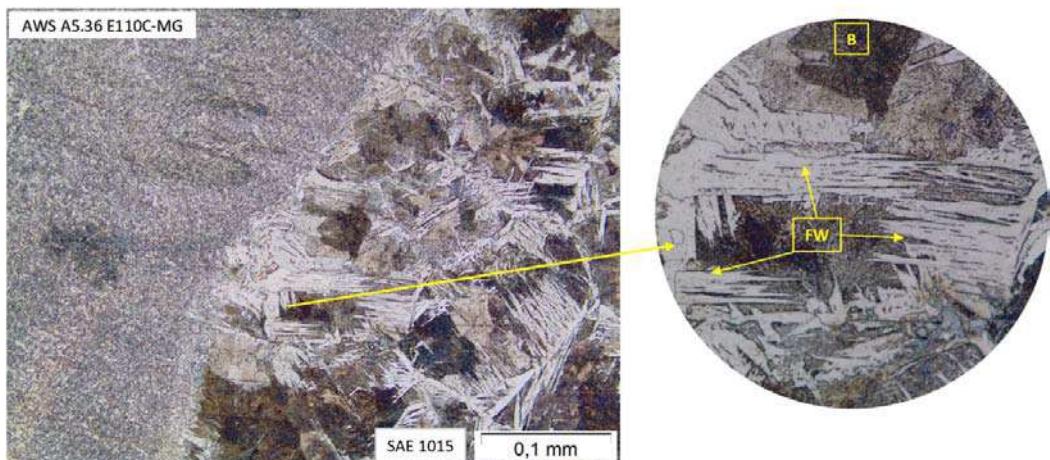
Figura 7: Ferrita de Widmanstätten (FW) na zona termicamente afetada pelo calor

3.3 Análise de microdureza Vickers para junta dissimilar com arame de baixa liga E110C-MG e junta com arame de baixo carbono ER70S-6

A Fig. 8 traz os resultados de microdureza para os arames em estudo. De acordo com a análise, para o arame AWS A5.36 E110C-MC, nota-se um aumento acentuado de dureza ao chegar na zona termicamente afetada pelo calor (ZTA).
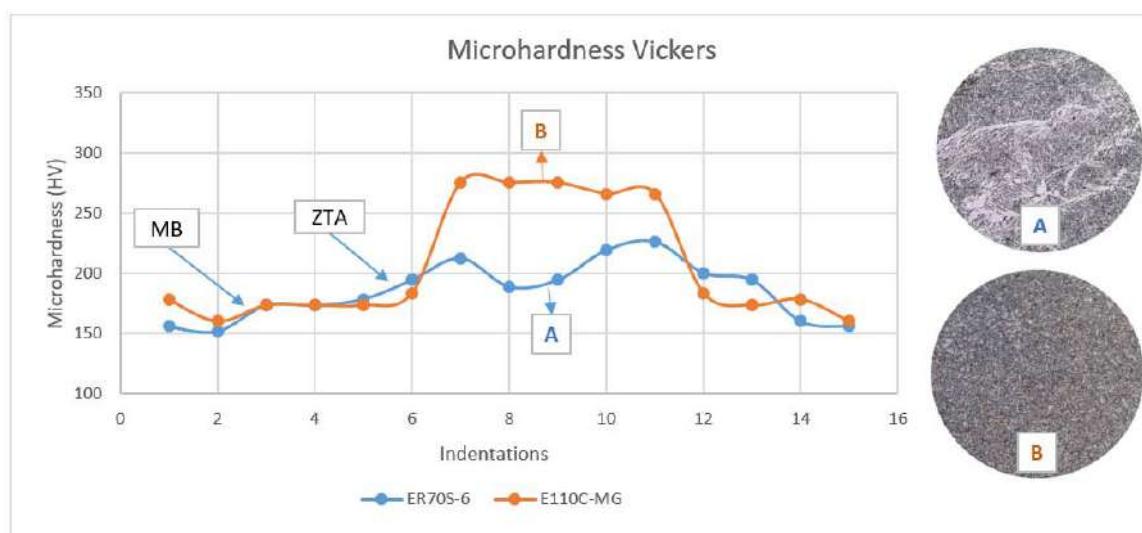
Figura 8: Gráfico de microdureza Vickers para ambos os arames em estudo. (ZTA) Zona Termicamente Afetada pelo calor, (MB) Material de Base

Para o arame AWS A5.36 E110C-MG, a média de microdureza na região de soldagem "B" apresentou valores de 272 ± 5 HV, entretanto, para a região do material de base (MB), o resultado foi de 172 ± 7 HV.

Contudo, ao se tratar do arame de soldadura AWS A5.18 ER70S-6, na região do material de base a microdureza ficou muito próximo, com 164 ± 11 HV, e para região de soldagem obteve-se um aumento, ficando em 206 ± 15 HV.

3.4 Análise termográfica para junta dissimilar com arame de baixa liga E110C-MG e junta com arame de baixo carbono ER70S-6.

A Fig. 9 detalha a avaliação térmica para os arames em estudo. Conforme figura, o primeiro

London Journal of Engineering Research

ponto traz as temperaturas para a poça de fusão, onde chega a 1650,2 °C e 1618,4 °C para os arames E110C-MG e ER70S-6, respectivamente.
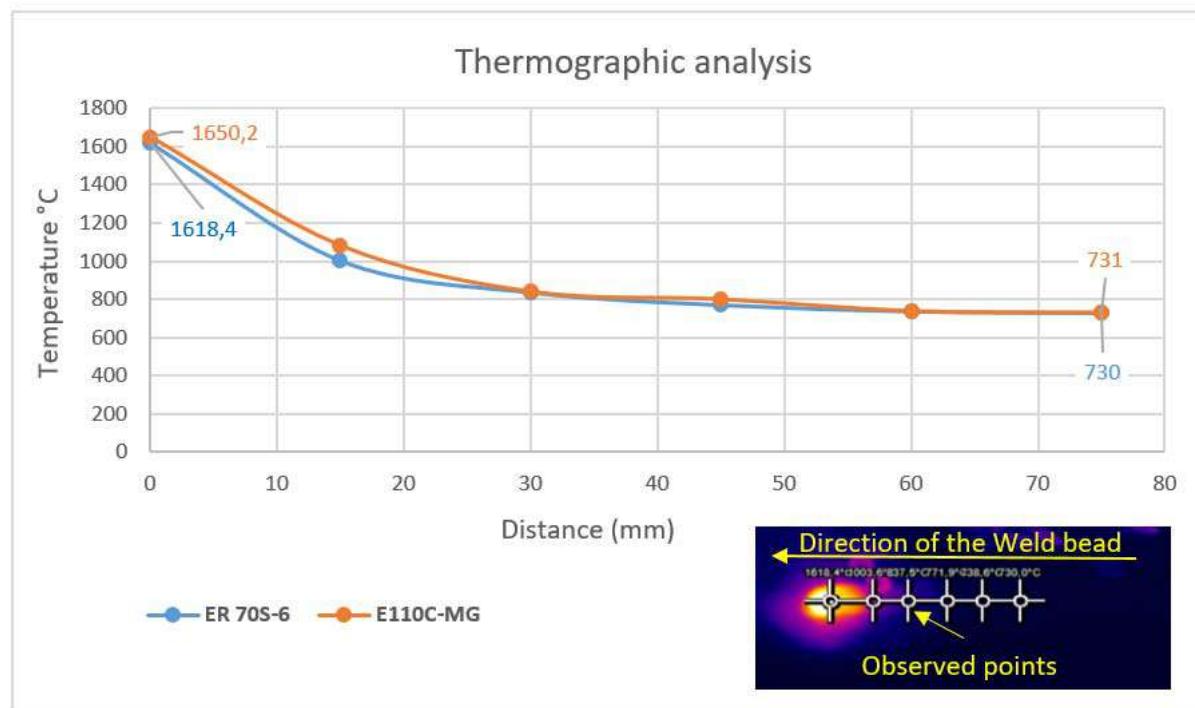
Fonte: Do Autor

Figura 9: Análise Termográfica do Momento da Solda

VI. CONSIDERAÇÕES FINAIS

Conforme literatura, soldas com diferentes características estão se tornando essenciais para atender a área de metalurgia. Dessa forma, conforme comparação entre a soldagem com arame AWS A5.18 ER70S-6 e a soldagem com arame AWS E110C-MG, há diferenças entre microestrutura e microdureza. Contudo, ressalta-se às elevadas temperaturas para poça de fusão, bem como para fundir os materiais. Dessa forma, ao comparar as microdureza na região de soldagem, obteve-se um aumento de 24 % para o arame AWS A5.36 E110C-MG, o que pode ser explicado por este material possuir cromo e molibdênio em sua estrutura. A avaliação metalográfica demonstrou tamanho de grão fino para o arame AWS A5.36 E110C-MG, sendo o refino de grão outro fator de aumento de microdureza. Contudo, a região da zona termicamente afetada pelo calor demonstra grãos grosseiros, bem como ferrita de Widmanstätten, o que ocorre quando se possui elevadas temperaturas seguidas de resfriamento moderado.

AGRADECIMENTOS

REFERÊNCIAS

1. RIBEIRO, Jorge.; FERREIRA, Carlos.; SOUZA, Mauro.; MONINE, Vladimir. *Estudo estrutural da junta soldada dissimilar entre o aço inox austenítico AISI 347 e o aço carbono ferrítico ASTM A36.* BrazilianJournal of Developmen. 2020. Disponível em: https://doi.org/10.34117/bjdv6n9-098. Acesso em: 06 de setembro de 2024.

2. KUMAR, Niraj.; KUMAR, Prakash. *Investigation on microstructural and mechanical integrity of GTAW dissimilar welded joint of IN 718/ASS 304L using Ni-based filler IN 625 using EBSD and DHD techniques.* International Journal of Pressure Vessels and Piping. Volume 209, junho de 2024. Disponível em: https://doi.org/10.1016/j.ijpvp.2024.105213. Acesso em: 06 de setembro de 2024.

3. SANTOS, Pedro.; CARVALHO, Derek. *Caracterização microestrutural de solda dissimilar entre aço carbono e inox pelo processo s.m.a.w.* Disponível em: https://www.fucap.edu.br/dashboard/biblioteca_repoisitorio/0f416c2a28f6c19e4db80feb1790f57b.pdf. Acesso em: 06 de setembro de 2024.

4. ZHOU, Xiaohui.; LI, Ruihan.; WANG, Binggiu.; WEI, Lianfeng.; TIAN, Lei.; YANG, Mingrui.; SONG, Xiaoguo.; TAN, Caiwang. *Microstructure evolution and corrosion behavior improvement of oscillation laser welded 2205/316L dissimilar joints used in offshore platform.* Ocean Engineering. Volume 311, Part. 1, 1 November 2024. Disponível em: https://doi.org/10.1016/j.oceaneng.2024.118833. Acesso em: 06 de setembro de 2024.

5. SURKAR, Hardik.; KUMAR, Amit.; SIROHJ, Sachin.; PANDEY, Shaijesh.; ŚWIERCZYŃSKA, Aleksandra.; FYDRYCH, Dariusz. PANDEY, Chandan. *A dissimilar welded joint of grade 92 steel and AISI 304L steel obtained using IN82 buttering and IN617 filler: relationship of microstructure and mechanical properties.* Volume 24, article number 109, (2024). Disponível em:https://link.springer.com/article/10.1007/s43452-024-00920-x. Acesso em: 06 de setembro de 2024.

6. RAMKUMAR, D.; OZA, S.; PERIWAL, S.; ARIVAZHAGAN, N.; SRIDHAR, R.; NARAYANAN, S. Characterization of weld strength and toughness in the multi-pass welding of Inconel 625 and Super-duplex stainless steel UNS S32750. Ciência & Tecnologia dos Materiais Volume 27, Issue 1, January–June 2015, Pages 41-52. Disponível em: https://doi.org/10.1016/j.ctmat.2015.04.004. Acesso em: 06 de setembro de 2024.

7. DAS, Rajkumar., SILVASWAMY, Giribaskar., LALVANI, Himansgu., SINGH, Ajit. Fracture toughness and microstructural analysis of rotary friction welded S355J2 and SS316L steels for critical applications. Journal of Advanced Joining Processes Volume 10, November 2024, 100244. https://doi.org/10.1016/j.jajp.2024.100244.

8. GOMORA, Cesar Mendoza; ORTIZ, Jesús Reyes; CEREZO, Erick Torres; SOTO, Carlos Ernesto Borja, SILVA, Jorge Zuno. Especificación y calificación de un procedimiento de soldadura disímil (wps) con proceso gmaw, para láminas de acero de bajo carbono y acero martensítico. Ingenio y Conciencia. pg. 11-17. 2020.

9. AGUIRRE, Humberto Vinicius Muñoz; TEIXEIRA, Felipe Ribeiro; MOTA, Carlos Alberto Mendes; NASCIMENTO, Alexandre Saldanha. *Avaliação de Soldas Dissimilares com a Técnica da Dupla Camada Utilizando os Arames-Eletrodos AWS ER 316L e ER NiCrMo-3 sobre o Aço ASTM A182 F22.* Matéria (Rio J.) 26 (03). 2021.

10. BÖHLER HL 85 T-MC-B: *Arame tubular metalcored, aço baixa-liga, alta resistência.* Abril de 2008.

11. AWS A5.36/A5.36M:2016. Specification for Carbon and LowAlloy Steel Flux Cored Electrodes for Flux Cored Arc Welding and Metal Cored Electrodes for Gas Metal Arc Welding. 2º edição. Pág. 23.

12. AWS A5.18/A5.18M:2021. Specification for Carbon Steel Electrodes and Rods for Gas Shielded Arc Welding. 8º Edição. Pág. 11.

13. merican Society for Testing and Materials. *A 29/A 29M – 05. Standard Specification for Steel Bars, Carbon and Alloy, Hot-Wrought, General Requirements for.* Nova York. Pág. 3. 2005.

14. SILVA, Thiago. Efeito dos parâmetros de trefilação nas propriedades mecânicas e microestruturais do aço sae 1015 trefilado. Universidade Federal do Ceará. Departamento de Engenharia Metalúrgica e Materiais curso de Engenharia Metalúrgica. https://www.repositoriobib.ufc.br/000020/00002032.pdf.

Evaluation of the Connection Line in Dissimilar Welding with Low Alloy and Low Carbon Wire using the Gmaw Process

15. Aços Especiais Iguatemi. *AÇO CARBONO*. São Paulo, 2024. https://www.acosiguatemi.com.br/produtos/aco-carbono/

Evaluation of the Connection Line in Dissimilar Welding with Low Alloy and Low Carbon Wire using the Gmaw Process

Tracking Control using Sensor Technology Solar Cell: In Real Time Domain Analysis

Summera Shamrooz & Muhammad Shamrooz Aslam

University of Mining and Technology

ABSTRACT

Solar Tracking (ST) is employed to maximize output power due to the nonlinear characteristics of renewable energy sources. Sunlight is considered the most reliable traditional source of energy when energy emergencies arise. First, we present some basic characteristics of the motor in the form of Tables and Figures. Solar panel tracking is, therefore, necessary to enhance their efficiency. In this article, we present the sensor based viz. STM32 microcontroller has been implemented in real-time using the PV arrays. In addition, we did an analysis of stateof-the-art reviews of solar photo-voltaic systems for this research article. Researchers have developed sensor-based techniques to improve renewable energy systems. This technique performs better than other traditional methods.

Keywords: solar panel; tracking control, sensor technology.

Classification: DDC Code: 621.312

Language: English

Tracking Control using Sensor Technology Solar Cell: In Real Time Domain Analysis

Summera Shamrooz[α] & Muhammad Shamrooz Aslam[σ]

ABSTRACT

Solar Tracking (ST) is employed to maximize output power due to the nonlinear characteristics of renewable energy sources. Sunlight is considered the most reliable traditional source of energy when energy emergencies arise. First, we present some basic characteristics of the motor in the form of Tables and Figures. Solar panel tracking is, therefore, necessary to enhance their efficiency. In this article, we present the sensor based viz. STM32 microcontroller has been implemented in real-time using the PV arrays. In addition, we did an analysis of stateof-the-art reviews of solar photo-voltaic systems for this research article. Researchers have developed sensor-based techniques to improve renewable energy systems. This technique performs better than other traditional methods.

Keywords: solar panel; tracking control, sensor technology.

Author α: Artificial Intelligence Research Institute, China University of Mining and Technology, Xuzhou, 221116, China.
σ: School of Mechatronic Engineering, China University of Mining and Technology, Xuzhou, 2211106, China.

I. INTRODUCTION

The demand for alternative energy sources has increased significantly due to environmental concerns and rising oil prices. Studies have been carried out in the last decade on alternative sources of energy and their applications. Renewable energy has a number of applications that make it competitive. Several feasible applications have brought attention to solar, wind, *fuel cells (FC)*, and *hybrid renewable energy systems* (*HRES*). Nevertheless, *photovoltaic* (*PV*) and *wind turbine* (*WT*) systems differ according to their characteristics, which depend on solar radiation, ambient temperature, wind speed, hydrogen fuel rate, and load impedance. There are two main ways to utilize solar energy. As a first method, the captured heat is used for space heating, which is a solar thermal energy source. Using the *PV* effect, incident solar irradiance can be converted into electrical energy. The *PV* panel can be imitated by *DC* sources that have the same characteristics as current to voltage (Li et al., 2019). Another technique uses programmable *DC* sources for this purpose. There have been discussions about the *Maximum Power Point (MPP)*, referred to as *MPPT* (Garcia-Blanco et al., 2018; Khan & Mathew, 2018; Khan & Mathew, 2020). The MPPT technique aims to match the load impedance to the source impedance by adjusting the duty cycle of the dc-dc converter. The *MPPT* algorithm is not only enabling a greater power conveying from the solar panels to the solar arrays but as well extending the life of the solar array (John & Davis, 2018).

Research into alternative approaches of electrical power production has increased in recent years with ecological concerns such as greenhouse gas emissions and energy costs. Research into renewable sources is booming in recent years. It is aiming to find non-polluting energy sources as well as explore how to use renewable energy frameworks more efficiently and reduce power costs per peak watts (Khan, 2021). An *HRES* system with self-excited induction generators and powerpreparing circuits was developed using a dynamically-driven wind-driven induction generator (Valenciaga & Puleston, 2005). The *MPPT* algorithm presented on this page was modest and costeffective without analyzing ecological scenarios (Giraud & Salameh, 2001). The rationale for developing this *MPPT* algorithm for solar *PV* and wind turbines without

considering ecological situations is modest and cost-effective (Ali et al., 2014). Using voltage- and current-based *MPPT* techniques for *PV* systems, while on the other side, authors conducted an experimental and theoretical study for the assessment of fast and reliable *MPPT* control methods (Karanjkar et al., 2014).

The experimental microgrid is operated automatically in standalone conditions through the installation of a power management system (PMS) on an embedded microcontroller. In an islanded microgrid, battery state-of-charge (SOC) represents a critical operation element for the continuity of supply of power, therefore, the PMS has been designed to estimate and control it. On the other hand, sensor technology has played a significant role in the development of tracking control (Aslam & Qaisar, 2023 & Aslam MS, Li Q, Hou J 2021). *Fuel cells (FCs)* of the kilowatt (kW) class appear to be of general interest in residential applications within this context (Bagnoli & De Pascale, 2005; Gunes & Ellis, 2001; Shammes & Boersma, 2000). As opposed to other conventional small generators, *FMs*, and in particular *PEMs*, provide a higher level of cogeneration, dependable and quiet operation, and a more cost-effective power supply than other generators. A recent review by (Erdinc & Uzunoglu, 2010) examined different architectures of PEM FC-based systems, as well as combining them with power generation and energy storage components to construct what is known as hybrid systems. Therefore, it is necessary to investigate this kind of problem in an effective way.

In this paper, the sensor-based viz. *STM32 microcontroller* has been implemented in realtime using the *PV arrays*. First, we present motor characteristics in the form of *Tables* and *Figures*. In the construction of hardware, we cut the solar cells into small pieces; the required voltage and current are made, and then packaged it. Then, we analyzed the performance index of *MATLAB* code for achieving optimal results. We defined the objective function of *MATLAB* code and specified their constraints. A simulated result is provided in order to determine the PC's efficiency.

In the rest of the paper, *Section 2* presents the specification of solar arrays. The experimental setup is explained in *Section 3*. The conclusion part is presented in *Section 4*.

II. SPECIFICATIONS OF SOLAR ARRAY

Solar Epoxy Sheet is a kind of solar panel, but the way of packaging is different. By cutting the solar cells into small pieces, the required voltage and current are made and then packaged. Because of the small size, the packaging method similar to solar photovoltaic modules is generally not used, but the solar cells are covered with epoxy resin and bonded with the *PCB* circuit board with low cost and so on.

The specification and physical map for our experiment are given in *Table 1* and *Figure 1*. The parameters of the solar panel are all measured under standard test conditions which are temperature 25 degrees, AM1.5, and light intensity 1000W/m2. In our experiment, we used a DC motor to move the solar panel. So, first, we define the characteristics of a *DC motor* in the form of torque speed relation. We present *Table 2* and *Table 3*.

Table 1: Solar Epoxy Board Parameters with 14.5cm lead wire

Parameters	Range
Operating Voltage	0-5v
Operating Current	0-60mA
Dimension	68X37mm

Figure 1: Physical Map for Hardware

Table 2: Induction machine torque speed characteristic at rated voltage

Speed (rpm)	V = 400 V ; R = 0 Ω	
	Torque (Nm)	I (A)
0	177.4	105.2
100	181.9	103
200	186.3	100.5
300	190.4	97.65
400	193.8	94.44
500	196.4	90.78
600	197.8	86.58
700	197.3	81.75
800	194.2	76.18
900	187.6	69.74
1000	176.2	62.33
1100	158.7	53.87
1200	133.5	44.38
1300	99.07	34.22
1400	54.5	24.79
1425	41.76	22.96
1450	28.41	21.56
1475	14.48	20.71
1500	1.967e-0.9	20.53

Furthermore, we demonstrate the characteristics of DC motors. In *Figure 2,* we present the *Speed vs Torque* properties under different voltage levels, while in *Figure 3*, we demonstrate the *Speed vs current* properties under different voltage levels. In the same consequences, *Figure 4* and *Figure 5* present the *Speed vs Torque* and *Speed vs current under* different values of resistance, respectively.

Speed vs Torque Characteristics (Graph 1)
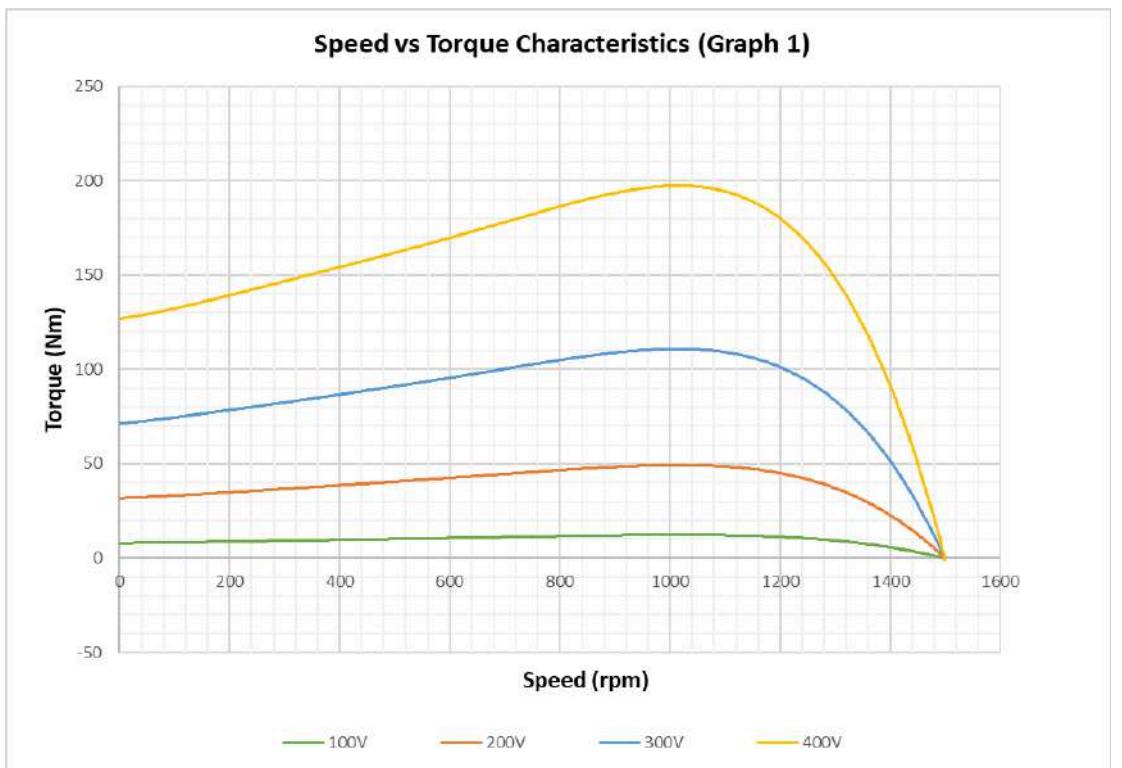
Figure 2: Speed vs Torque Properties under Various Voltage Levels

Speed vs Current Characteristics (Graph 2)
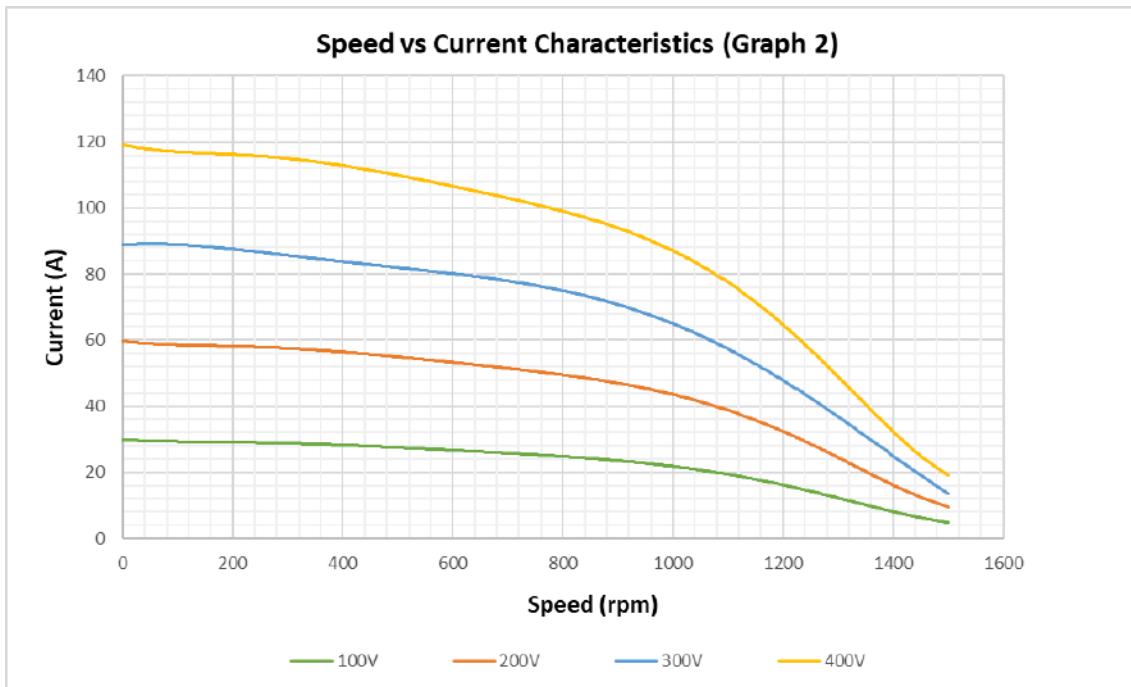
Figure 3: Speed vs Current Properties under Various Voltage Levels

The literature survey of this paper involves an analysis of state-of-the-art reviews of solar photovoltaic systems. The authors have reviewed and analyzed various research articles and publications related to solar photo-voltaic systems to understand the current trends and advancements in the field. The analysis of literature survey helped the authors to propose a sensor-based system using a STM32 microcontroller to improve the efficiency of solar panel tracking. The authors have also compared their proposed system with other traditional methods

---

and found that the sensor-based system performs better than other methods. Overall, the literature survey helped the authors to understand the current state of research in the field and propose a novel approach to improve the efficiency of solar photo-voltaic systems.
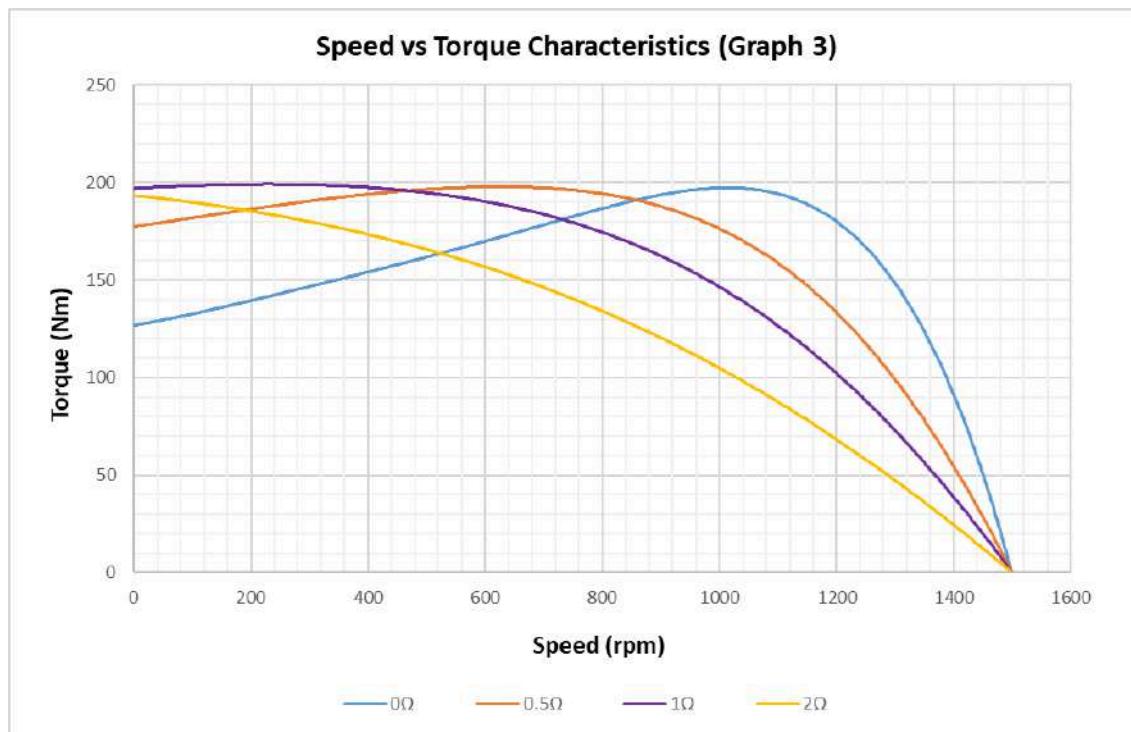

Figure 4: Speed vs torque properties under various resistance levels
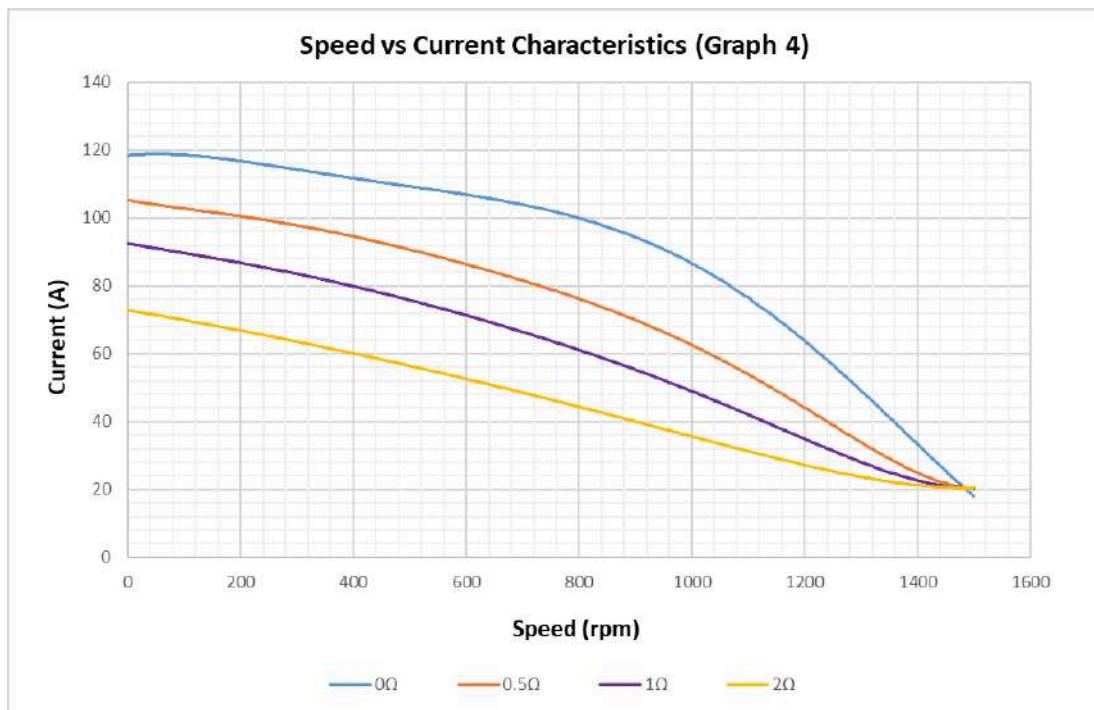
Figure 5: Speed vs Current Properties under Various Resistance Levels

First, we check the influence of an external resistor connected to the rotor on the Tcharacteristic. For this, we examine the Load of the model *AC WRIM* Rotor Resistance. Set the speed to 0 rpm, the voltage to 400 V, the frequency to 50 Hz, and the rotor resistance to

London Journal of Engineering Research

0.5 Ω and run the simulation. Then, increase the speed by 100 rpm and record the torque and current until reaching 1400 rpm. Record the torque and current for each step. Similarly, increase the speed by 25 rpm until 1500 rpm. Record the torque and current for each step.

Change the rotor resistance to 1 Ω. Repeat the steps for the 0.5 Ω and fill in *Table 3*. Change the rotor resistance to 2 Ω. Repeat the steps for the 0.5 Ω. These phenomena can be observed in *Table 3*.

Table 3: Induction machine torque speed characteristic function of the supply voltage for: (i) 300V, (ii) 200V, and (iii) 100 V

Speed (rpm)	V = 300 V ; R = 0 Ω		V = 200 V ; R = 0 Ω		V = 100 V; R = 0 Ω	
	Torque (Nm)	I (A)	Torque (Nm)	I (A)	Torque (Nm)	I (A)
0	235.5	157	104.7	104.7	26.16	52.34
100	236.6	152.1	105.2	101.4	26.29	50.69
200	237.3	146.8	105.5	97.85	26.36	48.92
300	237.2	141	105.4	94.02	26.36	47.01
400	236.3	134.8	105	89.86	26.25	44.93
500	234.2	128	104.1	85.34	26.03	42.67
600	230.8	120.6	102.6	80.4	25.64	40.2
700	225.5	112.5	100.2	74.99	25.06	37.49
800	217.9	103.5	96.86	69.03	24.21	34.51
900	207.4	93.66	92.16	62.44	23.04	31.22
1000	192.9	82.69	85.73	55.13	21.43	27.56
1100	173.3	70.46	77.04	46.97	19.26	23.49
1200	147.1	56.81	65.36	37.87	16.34	18.94
1300	111.8	41.64	49.68	27.76	12.42	13.88
1400	64.29	25.53	28.57	17.02	7.143	8.509
1425	50.01	21.74	22.23	14.5	5.556	7.248
1450	34.6	18.44	15.38	12.3	3.845	6.148
1475	17.97	16.11	7.986	10.74	1.996	5.369
1500	2.484e-0.9	15.4	1.104e-0.9	10.27	2.76e-10	5.133

Remark 1: This research process a strategy for nalyzing the current and voltage charatertics of PC due to envurnmental changes. The follow keys problems were implemented in this research:

- *Simulink/MATLAB platforms were used to implement the proposed strategy.*
- *A sensor-assisted system was examined.*
- *Sensor-based viz. STM32 microcontroller has been implemented in real-time using the PV arrays.*
- *Researchers analyzed the performance index of MATLAB code for achieving optimal results.*
- *Solar panel tracking was done using a DC motor. Solar cells were cut into small pieces, the required voltage and current were made, and then packaged it.*
- *State-of-the-art reviews of solar photo-voltaic systems were analyzed for this research article.*

In the experiment setup, our hardware specifications are given in *Table 4*.

Table 4: Specification of Solar Panel

Name	Numerical Values
Operating Voltage	0-36v
Dimensions	130X140mm
Size	120X125mm

Solar Panel

Tracking Light

Figure 6: Solar Panel

The practical implications of this paper are as follows:

- *The proposed sensor-based system using a STM32 microcontroller can be implemented in real-time to enhance the efficiency of solar panel tracking.*
- *The strategy for analyzing the current and voltage characteristics of a PC due to environmental changes can be used to provide sensor-based feedback for the solar tracking performance strategy.*
- *The performance index of MATLAB code was analyzed to achieve optimal results, which can be useful for researchers and engineers working in the field of renewable energy systems.*
- *The presented PC panel's tracking strategy using a DC motor and a sensor-assisted system can be used to improve the efficiency of solar photo-voltaic systems.*
- *The state-of-the-art reviews of solar photo-voltaic systems analyzed in this paper can be useful for researchers and engineers to understand the current trends and advancements in the field.The performance index of MATLAB code was analyzed to achieve optimal results, which can be useful*

for researchers and engineers working in the field of renewable energy systems.

Overall, the paper provides practical insights into the use of sensor-based techniques to improve the efficiency of renewable energy systems, specifically solar photo-voltaic systems.

include a *LED lamp*, *solar panels*, a battery, a charger, and maybe an inverter, too. Solar panels are used to charge the lamp's batteries, which run on electricity.

III.   EXPERIMENTAL SETUP

3.1   Solar LED Lights

Often referred to by the name solar light or solar lantern, solar lamps are lighting systems that
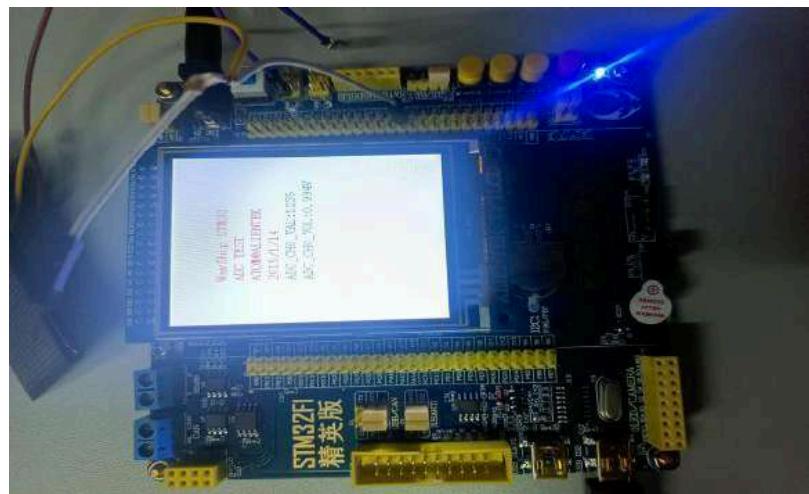
(a)   LED of STM32 Microcontroller
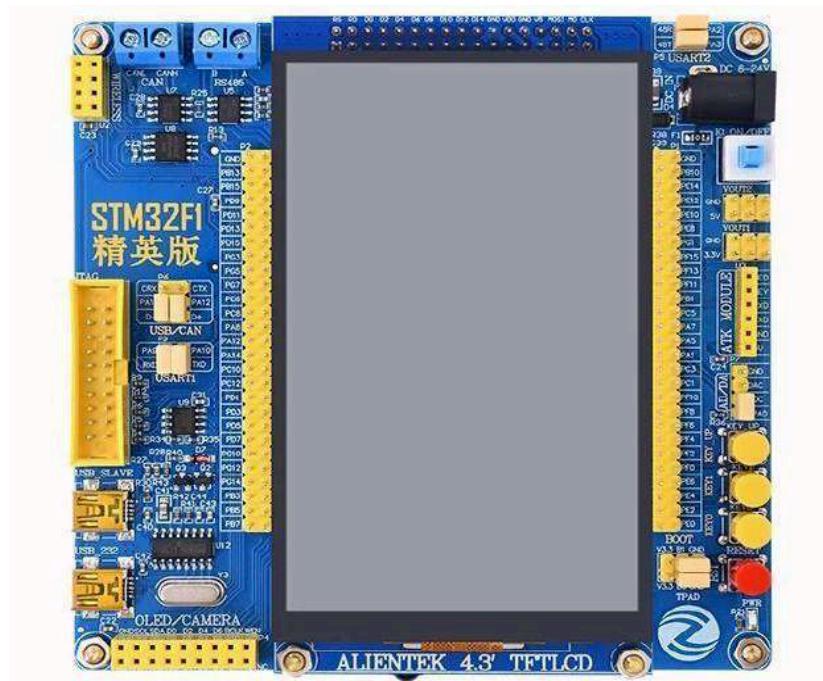
(b)   Digital Controller STM32F1

(c)   Digital Controller connected with PC

Figure 7: Overview of the Hardware Setup

Figure 7 presents the experimental setup of our research. While in *Figure 8*, presents the Real-time data collection graph. This result is obtained by the following algorithm:
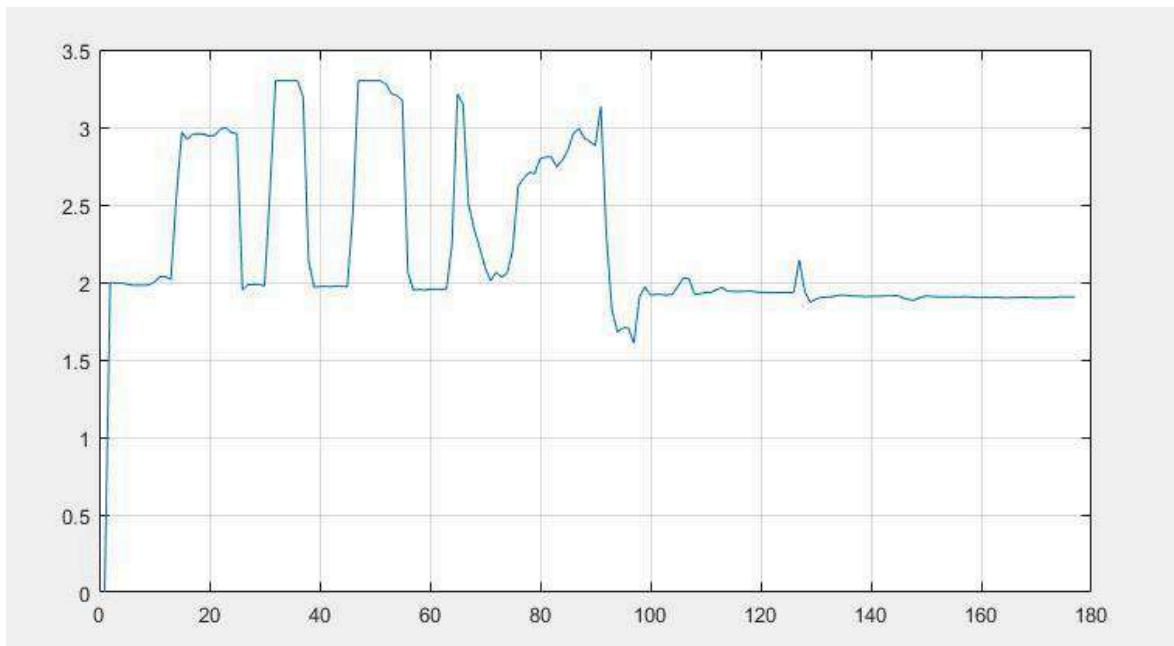
Figure 8: Real-time data collection graph

The basic parameters of the STM32F1 Elite Edition are as follows:

1. *Onboard 16MByte SPI FLASH with large capacity;*
2. *Onboard EEPROM, infrared, JTAG interface, USB Slave.*

3. *Provide more than ten kinds of interfaces, which are convenient to connect various modules for development and testing;*
4. *Onboard 6~24V wide power adapter interface, suitable for common power adapters;*
5. *With 4.3-inch touch LCD module;*
6. *Support UCOSII1/LWIP/Fatfs/Emwin.*

Tracking Control using Sensor Technology Solar Cell: In Real Time Domain Analysis

7. *The 3.3V/5V power supply/access interface terminal common to the on-board punctuality development board is convenient for external devices and the development board to obtain and supply power from each other.*

In the end, we also present the *MATLAB code* for the *data acquisition*.

Appendix: (MATLAB Data Acquisition Program)

```
delete(instrfindall);
s=serial('COM4');
set(s,'BaudRate',115200);
fopen(s);
interval=5000;
passo=1; t=1; x=0;
while(t<interval) b=str2num(fgetl(s));
x=[x,b];
plot(x);
grid t=t+passo;
drawnow; end
```

VI.   CONCLUSION

A PC panel's tracking is described in this paper. *Simulink/MATLAB* platforms were used to implement the proposed strategy and a sensor-assisted system was examined. This paper proposes a strategy for analyzing the current and voltage characteristics of a PC due to environmental changes. It is analyzed how to provide sensor-based from the PC through the ST's performance strategy. In this article, we analyzed the performance index of *MATLAB* code for achieving optimal results. We defined the objective function of *MATLAB* code and specified their constraints. A simulated result is provided in order to determine the PC's efficiency.

REFERENCES

1. Aslam MS, Qaisar I (2023). Sensor networks with distributed event-triggered scheme for T–S fuzzy system with dissipativity analysis, *European Journal of Control*, 71:100800, https://doi.org/10.1016/j.ejcon.2023.100800.

2. Aslam MS, Li Q, Hou J (2021). Fault detection for asynchronous T–S fuzzy networked Markov jump systems with new event-triggered scheme. *IET Control Theory & Applications*, 15(11):146173.

3. Ali, A. N., Jayabharath, R., & Udayakumar, M. D.(2014). An ANFIS based advanced MPPT control of a wind-solar hybrid power generation system. *International Review on Modelling and Simulations*, *7*(4), 638–643. https://doi.org/10.15866/iremos.v7i4.2457

4. Bagnoli, M., & De Pascale, A. (2005). Performance evaluation of a small size cogenerative system based on a PEM fuel cell stack. In *Turbo Expo: Power for Land, Sea, and Air* (vol. 47276, pp. 143-150). https://doi.org/10.1115/GT2005-68451

5. Erdinc, O., & Uzunoglu, M. (2010). Recent trends in PEM fuel cell-powered hybrid systems:

6. Investigation of application areas, design architectures and energy management approaches.

7. *Renewable and Sustainable Energy Reviews*, *14*(9), 2874-2884. https://doi.org/10.1016/j.rser.2010.07.060

8. Garcia-Blanco, R., Díez, P., Borzacchiello, D., & Chinesta, F. (2018). Algebraic and parametric solvers for the power flow problem: towards real-time and accuracy-guaranteed simulation of electric systems. *Archives of Computational Methods in Engineering*, *25*(4), 1003-1026. https://doi.org/10.1007/s11831-017-9223-6

9. Giraud, F., & Salameh, Z. M. (2001). Steady-state performance of a grid-connected rooftop hybrid wind-photovoltaic power system with battery storage. *IEEE transactions on energy conversion*, *16*(1), 1-7. https://doi.org/10.1109/60.911395

10. Gunes, M. B., & Ellis, M. W. (2001). Evaluation of Fuel Cell Based Combined Heat and Power Systems for Residential Applications. In *ASME International Mechanical Engineering Congress and Exposition* (vol. 35524, pp. 417-428), American Society of Mechanical Engineers. https://doi.org/10.1115/IMECE2001/AES-23651

11. John, D. K., & Davis, S. (2018). Integrated flyback converter with MPPT control for photovoltaic applications. *International Journal of Power Electronics Controllers and Converters*, 4(2), 33-40. https://doi.org/10.37628/ijpecc.v4i2.903

12. Karanjkar, D. S., Chatterji, S., Shimi, S. L., & Kumar, A. (2014). Real time simulation and analysis of maximum power point tracking (MPPT) techniques for solar photo-voltaic system. In *2014 Recent Advances in Engineering and Computational Sciences (RAECS),* IEEE (pp. 1-6). https://doi.org/10.1109/RAECS.2014.6799656

13. Khan, M. J. (2021). Review of recent trends in optimization techniques for hybrid renewable energy system. *Archives of Computational Methods in Engineering*, *28*(3), 1459-1469. https://doi.org/10.1007/s11831-020-09424-2

14. Khan, M. J., & Mathew, L. (2018). Comparative analysis of maximum power point tracking controller for wind energy system. *International Journal of Electronics*, *105*(9), 1535-1550. https://doi.org/10.1080/00207217.2018.1461251

15. Khan, M. J., & Mathew, L. (2020). Comparative study of optimization techniques for renewable energy system. *Archives of Computational Methods in Engineering*, 27, 351-360. https://doi.org/10.1007/s11831-018-09306-8

16. Li, H., Yang, D., Su, W., Lü, J., & Yu, X. (2019). An overall distribution particle swarm optimization MPPT algorithm for photovoltaic system under partial shading. *IEEE Transactions on Industrial Electronics*, *66*(1), 265-275. https://doi.org/10.1109/tie.2018.2829668.

17. Sammes, N. M., & Boersma, R. (2000). Small-scale fuel cells for residential applications. *Journal of Power sources*, 86(1-2), 98-110. https://doi.org/10.1016/s0378-7753(99)00415-2

18. Valenciaga, F., & Puleston, P. F. (2005). Supervisor control for a stand-alone hybrid generation system using wind and photovoltaic energy. *IEEE transactions on energy conversion, 20*(2), 398405. https://doi.org/10.1109/tec.2005.845524

Tracking Control using Sensor Technology Solar Cell: In Real Time Domain Analysis

This page is intentionally left blank

On the Mechanical Interaction between two Small Antennas

V. V. Arabadzhi

ABSTRACT

The emergence of a time-constant interaction force between a pair of antennas of sound and electromagnetic waves is shown analytically. This force is identically analytically expressed through the phases of excitation of the antennas and the distance between them both for acoustic and electromagnetic cases. Frequencies, excitation phases, and distances between the antennas were found at which the antennas maximize either the mutual repulsive (attractive) forces in a pair of antennas, or the wave thrust forces that tend to move a pair of antennas in one direction. It is shown that the force of the wave thrust of a pair of antennas is opposite to the radiation flux, which plays a role similar to gases flowing from a rocket nozzle.

On the Mechanical Interaction between two Small Antennas

V. V. Arabadzhi

ABSTRACT

The emergence of a time-constant interaction force between a pair of antennas of sound and electromagnetic waves is shown analytically. This force is identically analytically expressed through the phases of excitation of the antennas and the distance between them both for acoustic and electromagnetic cases. Frequencies, excitation phases, and distances between the antennas were found at which the antennas maximize either the mutual repulsive (attractive) forces in a pair of antennas, or the wave thrust forces that tend to move a pair of antennas in one direction. It is shown that the force of the wave thrust of a pair of antennas is opposite to the radiation flux, which plays a role similar to gases flowing from a rocket nozzle. For a catamaran (two floats-antennas of surface gravity waves on water with a phase shift of their vertical oscillations by $\pi/2$) the forward motion speed and the force of wave thrust, as well as the surface jet current near the float, similar to the flow created by a propeller, were measured. In this case, the inversion $\pi/2 \to -\pi/2$ of the difference in the excitation phases of the half floats simultaneously led to an inversion of the thrust force, translational motion and jet flow. The dependence of the wave thrust on the excitation frequency (with a structurally fixed phase difference $\pi/2$) in the experiment turned out to be similar to the analytically obtained dependences for sound and electromagnetic waves.

Author: A. V. Gaponov-Grekhov Institute of Applied Physics RAS. 603950 Box-120 Nizhny Novgorod, Ulianov st. 46, Russia.

London Journal of Engineering Research

I. INTRODUCTION

In many boundary value problems of radiation monochromatic (at some frequency $\omega = \omega_0 \neq 0$) waves of various physical natures the force constant in time (at the frequency $\omega = 0$) called also "wave thrust" or "steady force" arises. This force is interpreted [1-3] as the transfer of mechanical momentum by a traveling wave and equal (as a rule) to the wave energy flux divided by the phase wave speed. Steady forces of mechanical interaction of 3D emitters (antennas) via their own time-varying wave fields were first studied experimentally by Peter Lebedev [4] and Vilhelm Bjerknes [5]. In most cases, the pressure not of the radiation field itself (Fig. 1-a) on the radiating boundary was considered, and the pressure of the scattering field (reflection, Fig. 1-b) of the incident wave on the scattering body. Several decades later, the problems of mechanical interaction of small antennas began to be studied in relation to the dynamics of three-dimensional gas bubbles in a liquid and the problem of their coagulation [6-10], when the forces of attraction and repulsion between the bubbles are very important (as well as in many other complicated acoustical problems [11-14] recently).
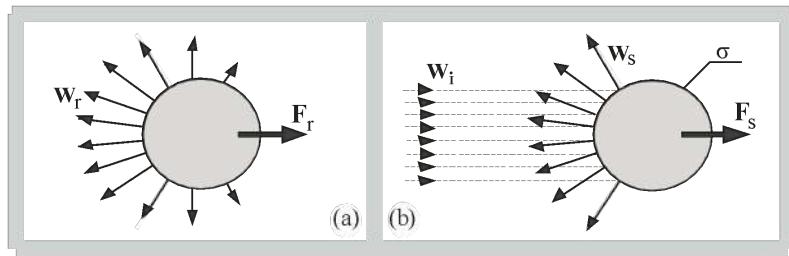
Figure 1: To the problems about pressure of the radiation field (a) and the pressure of the scattered field (b) on a body with a surface σ : $\mathbf{W_i}$ - power flow of the incident wave, $\mathbf{W_s}$ - power flow of the scattered wave, - power flow of the emitted wave, $\mathbf{F_s}$ - pressure force of the scattered field, $\mathbf{F_r}$ - pressure force of the radiated field.

In the 1 D boundary problem the volumetric steady force with which a plane sound wave acts on the propagation medium, taking into account the second order of its dynamics (for example, the dependence of the speed of sound on the amplitude), was considered analytically in [15]. The steady pressure of an incident sound wave on a flat reflecting interface (1D boundary problem) between two homogeneous compressible inviscid half-spaces was also considered [16], as well as the steady radiation pressure of a flat Huigence source in electrodynamics [17].

The purpose of the work [18] is to identify the similarities and differences in the manifestations of a wave thrust steady force [10] acting on a pair of small antennas irradiating each other with a fixed distance between them in application to acoustic waves, electromagnetic waves, waves on the surface of water in 3D and 1D boundary value problems. In the concrete boundary value problems for a monochromatic wave field (at the frequency $\omega = \omega_0 \neq 0$) considered below, this force is formed as the product of two components (just like the power flow) of the wave field at frequencies, which generates forces at the boundaries of a pair of antennas: power spectral density of these forces is concentrated at frequencies $\omega = 2\omega_0$ and $\omega = 0$.

II. WAVE THRUST OF ACOUSTICAL SMALL ANTENNAS

Let us imagine that a compressible inviscid medium (with density ρ_0 and speed c_0 of sound) surrounding a solid sphere $\hat{O}$ (the center of the sphere is fixed at point $x = 0$ and its radius a_0 is constant in time) oscillates uniformly in space along the axis $"x"$ with a certain complex velocity amplitude $V \neq 0$ at frequency ω_0. The medium tends to move the sphere from the point $x = 0$ of its fixation by some force $F \neq 0$. The same force, but with the opposite sign, will act on the medium, generating waves in it. For small size $a_0 \ll 1/k_0$ ($k_0 = \omega_0 / c_0$ - wave number) of the sphere $\hat{O}$, the problem described above is equivalent to determining the resistance force $F = Z_0 V$ of the medium during dipole (with a constant radius a_0 of the sphere $\hat{O}$) oscillations of the sphere $\hat{O}$ along the axis $"x"$ near a point $x = 0$ with complex amplitude $V \neq 0$ when the medium itself is motionless (as whole). In this case, the impedance Z_0 of such oscillations of a small sphere $\hat{O}$ is estimated as [19]

$$Z_0 = (\pi / 3)a_0^6 k_0^4 \rho_0 c_0 + \mathrm{i}(2\pi / 3)a_0^3 \omega_0 \rho_0 \,. \tag{1}$$

Oscillations (and pulsations below) of the sphere $\hat{O}$ are assumed to be small when the maximum displacement of the center of the sphere (or change in its radius) is much less than the unperturbed radius a_0 of the sphere, i.e.

$$|V|\pi / 4\omega_0 << a_0 .$$

(2)

Now let us instead one sphere $\hat{O}$ consider pair of identical spheres (antennas) $\hat{A}$, $\hat{B}$ of radius a_0 with given pulsations velocities V_A, V_B at frequency $\omega = \omega_0$, with centers fixed at points $x = -L_0$, $x = +L_0$ on the axis "x" (see Fig. 2-a). Each of these pulsating spheres creates velocity fields $V_{B\to A}$, $V_{A\to B}$ on the neighboring sphere [19]

$$V_{B\to A} = -V_B k_0^2 a_0^2 (1 + i k_0^2 a_0^2)^{-1} [(2k_0 L_0)^{-2} + i(2k_0 L_0)^{-1}] \exp(i\omega_0 t - 2 i k_0 L_0 - i k_0 a_0 - i\varphi_B) ,$$

(3)

$$V_{A\to B} = +V_A k_0^2 a_0^2 (1 + i k_0^2 a_0^2)^{-1} [(2k_0 L_0)^{-2} + i(2k_0 L_0)^{-1}] \exp(i\omega_0 t - 2 i k_0 L_0 - i k_0 a_0 - i\varphi_A) ,$$

(4)

where $V_A = V_0 \exp(-i\varphi_A)$, $V_B = V_0 \exp(-i\varphi_B)$ (φ_A, φ_B —given phases of spheres pulsations, $V_0 = \operatorname{Re} V_0$ —given module of velocity magnitudes, $a_0 << 1/k_0$, a_0 —radius of sphere in the absence of excitation. Velocity fields $V_{B\to A}$ and $V_{A\to B}$ generate forces

$$\mathbf{F}_{B\to A} = \mathbf{x}_0 Z_A V_{B\to A} , \qquad \mathbf{F}_{A\to B} = \mathbf{x}_0 Z_B V_{A\to B} ,$$

(5)

tending to cause dipole oscillations of spheres $\hat{A}$, $\hat{B}$ (with fixed centers at points $x = \pm L_0$) along the axis "x", and generating scattering of the field of the sphere $\hat{B}$ on the sphere $\hat{A}$ (and vice versa). Here, are oscillatory dipole impedances $Z_{A0} = Z_{B0} = Z_0$ (as stated in (1) above) of spheres. The smallness of the double (or higher) scattering of the fields of the spheres on each other guarantees, for example, inequality $(a_0 / 2L_0)^3 \sqrt{[1 + (2k_0 L_0)^2][1 + (k_0 a_0)^2]} << 1$ under the conditions $(a_0 / 2L_0) << 1$ and (2) (with substitution $V_A \to V$, or $V_B \to V$). Now note that in (5) we have of impedances $Z_A = Z_{A0} + \tilde{Z}_A(t)$, $Z_B = Z_{B0} + \tilde{Z}_B(t)$ of spheres $\hat{A}$, $\hat{B}$ consisting of parts constant in time and variable in time and their radiuses $a_A = a_0 + \tilde{a}_A(t)$, $a_B = a_0 + \tilde{a}_B(t)$ with given pulsation velocities $(da_A / dt) = V_0 \exp(-i\varphi_A)$, $da_B / dt = V_0 \exp(-i\varphi_B)$ correspondingly or

$$Z_A = Z_{A0} + (\partial \tilde{Z}_A / \partial a_0)(da_A / dt)(1 / i\omega_0) , \qquad Z_B = Z_{B0} + (\partial Z_{B0} / \partial a_0)(da_B / dt)(1 / i\omega_0) ,$$

(6)

$$da_A / dt = V_A \exp(i\omega_0 t - i\varphi_A) , \qquad da_B / dt = V_B \exp(i\omega_0 t - i\varphi_B) ,$$

(7)

where $(d / dt)Z_{A0} = (d / dt)Z_{B0} = 0$, $|\tilde{Z}_A(t)| << |Z_{A0}|$, $|\tilde{Z}_B(t)| << |Z_{B0}|$ and mean $< \tilde{Z}_{B0} >_T =< \tilde{Z}_B(t) >_T = 0$ on time period $T = 2\pi / \omega_0$ is zero. The quontities $\tilde{Z}_A(t)$, $\tilde{Z}_B(t)$, $V_A(t)$, $V_B(t)$, $V_{B\to A}(t)$, $V_{A\to B}(t)$ are oscillating at

On the Mechanical Interaction between two Small Antennas

frequency $\omega = \omega_0$. Therefore, their products $\mathbf{F}_{B \to A} = \mathbf{x}_0 Z_A(t) V_{B \to A}(t)$, $\mathbf{F}_{A \to B} = \mathbf{x}_0 Z_B(t) V_{A \to B}(t)$ (in (5)) have power spectral density concentrated at frequencies $\omega = \omega_0$, $\omega = 2\omega_0$ and $\omega = 0$. We are interested in the latter frequency $\omega = 0$. Substituting (6), (7) into (5) and averaging over the period $T = 2\pi / \omega_0$, we obtain constant forces of interaction of pulsating spheres in time (at frequency $\omega = 0$) $\hat{A}$ and $\hat{B}$:
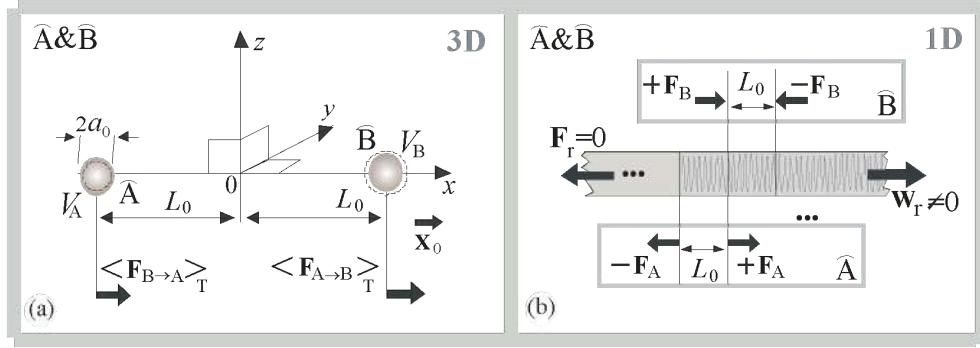

Figure 2: To the problem of the wave thrust of a pair $\hat{A}\&\hat{B}$ of three-dimensional acoustic antennas: (a) a pair of pulsating spheres; (b) a one-dimensional Huygens source driven by two pairs of forces $\pm \mathbf{F}_A(t)$ (antenna $\hat{A}$), and $\pm \mathbf{F}_B(t)$ (antenna $\hat{B}$) compression-tension applied to the boundaries $x = -L_0$, $x = 0$, $x = +L_0$ are giving zero radiation pressure force $\mathbf{F}_r(t) = 0$ at any ω_0, φ_A, φ_B, L_0.

$$< \mathbf{F}_{B \to A} >_T / q_a = -\mathbf{x}_0 [\alpha(\xi) \cos(\varphi_A - \varphi_B) - \beta(\xi) \sin(\varphi_A - \varphi_B)] \,, \tag{8}$$

$$< \mathbf{F}_{A \to B} >_T / q_a = +\mathbf{x}_0 [\alpha(\xi) \cos(\varphi_A - \varphi_B) + \beta(\xi) \sin(\varphi_A - \varphi_B)] \,. \tag{9}$$

$$\alpha(\xi) = [\cos(\xi)/(\xi)^2] + [\sin(\xi)/(\xi)] \,, \quad \beta(\xi) = [\cos(\xi)/(\xi)] - [\sin(\xi)/(\xi)^2] \tag{10}$$

($\xi = 2k_0 L_0$) are the functions (see Fig. 3-b,c), for which $\alpha(-\xi) = \alpha(+\xi)$, $\beta(-\xi) = -\beta(+\xi)$, $\beta(0) = 0$, $q_a = 2\pi k_0^2 a_0^4 \rho_0 V_0^2$. At $\varphi_A - \varphi_B = \pi/2$ we obtain the wave thrust force ($\rightarrow \rightarrow$ ($\hat{A}$ repels $\hat{B}$, $\hat{B}$ attracts $\hat{A}$) at $\beta > 0$ or $\leftarrow \leftarrow$ ($\hat{B}$ repels $\hat{A}$, $\hat{A}$ attracts $\hat{B}$) at $\beta < 0$ Fig. 3-b):

$$< \mathbf{F}_\Sigma >_T = < \mathbf{F}_{A \to B} >_T + < \mathbf{F}_{B \to A} >_T = \mathbf{x}_0 2 q_a \beta \,, \tag{11}$$

and when $\varphi_A - \varphi_B = 0$ we get strength

$$< \mathbf{F}_{B \to A} >_T = -\mathbf{x}_0 q_a \alpha \,, \quad < \mathbf{F}_{A \to B} >_T = +\mathbf{x}_0 q_a \alpha \,, \tag{12}$$

repulsion $\leftarrow \rightarrow$ at $\alpha > 0$ and attraction $\rightarrow \leftarrow$ at $\alpha < 0$ (Fig. 3-c).

Now let's calculate the relative difference $\eta(k_0 L_0) = [H(k_0 L_0) - \bar{H}(k_0 L_0)]/[H(k_0 L_0) + \bar{H}(k_0 L_0)]$ between the integral radiation power fluxes forward $H(k_0 L_0) = \int_0^{\pi/2} \Phi(\vartheta, k_0 L_0) |\cos(\vartheta)| \sin(\vartheta) d\vartheta$ (in the sector $0 < \vartheta < \pi/2$ of

polar angles) and backward $\overline{H}(k_0 L_0) = \int_{\pi/2}^{\pi} \Phi(\vartheta, k_0 L_0) |\cos(\vartheta)| \sin(\vartheta) d\vartheta$ (in the sector $\pi/2 < \vartheta < \pi$), taking into account the projections $\Phi(\vartheta, k_0 L_0) |\cos(\vartheta)|$ of the radiation flux (in the far zone at a distance $k_0 L_0^2 \gg 1$ from the antenna $\hat{A} \& \hat{B}$), where $\Phi(\vartheta, k_0 L_0) = |U + U^*|^2$ - radiation power directional pattern of antenna $\hat{A} \& \hat{B}$, $U = \exp[\mathrm{i}(k_0 L_0)\cos(\vartheta) - \mathrm{i}(\varphi_A - \varphi_B)/2]$.

In Fig. 3-a shows: the dependence on the wave size $k_0 L_0$ of the difference $\eta(k_0 L_0)$ in power fluxes to the left and right (at $\varphi_A - \varphi_B = \pi/2$) and the directional pattern (in power, with an odd number of lobes) of the radiation of the pair $\hat{A} \& \hat{B}$ at values characterized by the maximum radiation. It can be seen that the function $\eta(k_0 L_0)$ almost mirror copies (with the opposite sign) the dependence (Fig. 3-b) of wave thrust $<\mathbf{F}_\Sigma>_T \sim \beta(k_0 L_0)$ ((10) at phases $\varphi_A - \varphi_B = \pi/2$) on the wave dimensions of the radiating system.

In this case, the maximum power is always radiated in the direction opposite to the traction force $<\mathbf{F}_\Sigma>_T$. In Fig. 3-c shows: the dependence on the wave size $k_0 L_0$ of the forces of attraction and repulsion $<\mathbf{F}_{B \to A}>_T = -<\mathbf{F}_{A \to B}>_T \sim \alpha(k_0 L_0)$ ((11) at phases $\varphi_A - \varphi_B = 0$ when the traction force $\beta = 0$ is zero and $\eta = 0$) on the wave size $k_0 L_0$, as well as symmetrical radiation directivity patterns $\Phi(\vartheta, k_0 L_0)$ (in power, with an even number of lobes) of the pair $\hat{A} \& \hat{B}$ at values of $k_0 L_0$, corresponding to the maxima of attraction or repulsion of antennas $\hat{A}$ and $\hat{B}$.
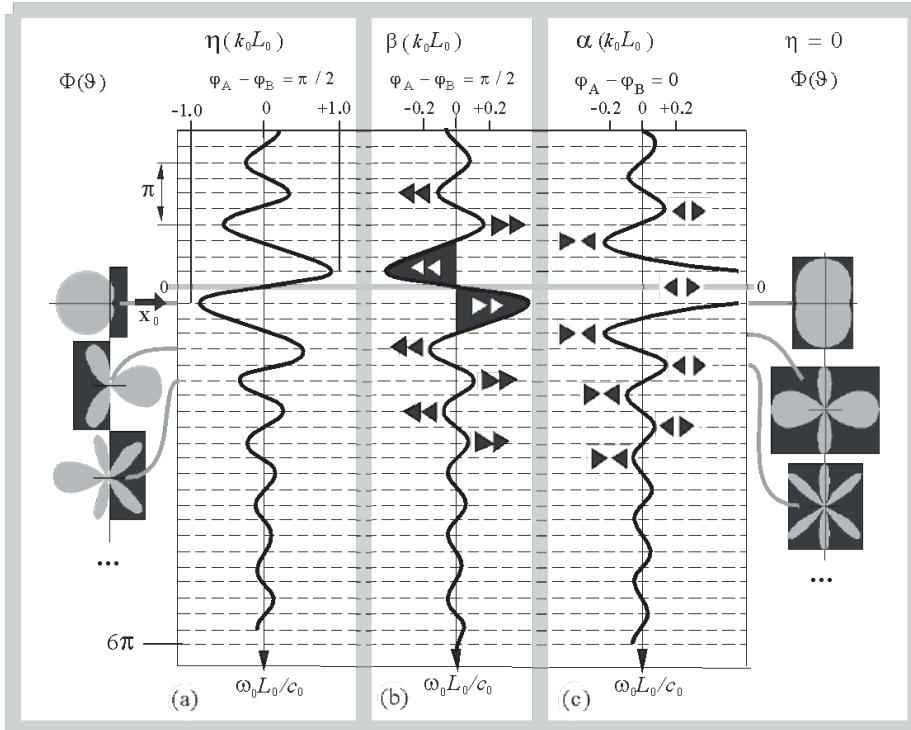

Figure 3: On the relationship between the directional pattern of the radiation power of a pair $\hat{A} \& \hat{B}$ and the force of wave thrust

(a) the normalized difference $\eta(k_0 L_0)$ between forward and backward radiation energy fluxes ($\parallel \mathbf{x}_0$) as a function of the wave half-distance $k_0 L_0$ between $\hat{A}$ and $\hat{B}$, examples of radiation directivity patterns $\Phi(\vartheta; k_0 L_0)$ at $(\varphi_A - \varphi_B) = \pi/2$ with noneven number of lobes (petals);

(b) the force $\beta(k_0 L_0)$ of the wave thrust of the pair $\hat{A}\&\hat{B}$ ($\rightarrow \rightarrow$ or $\leftarrow \leftarrow$ at $\varphi_A - \varphi_B = \pi/2$ and $\alpha = 0$);

(c) the force $\alpha(k_0 L_0)$ of attraction ($\rightarrow \leftarrow$) or repulsion ($\leftarrow \rightarrow$) at $\varphi_A - \varphi_B = 0$ and $\beta = 0$), examples of radiation directivity patterns $\Phi(\vartheta; k_0 L_0)$ at $(\varphi_A - \varphi_B) = 0$ with even number of lobes (petals).
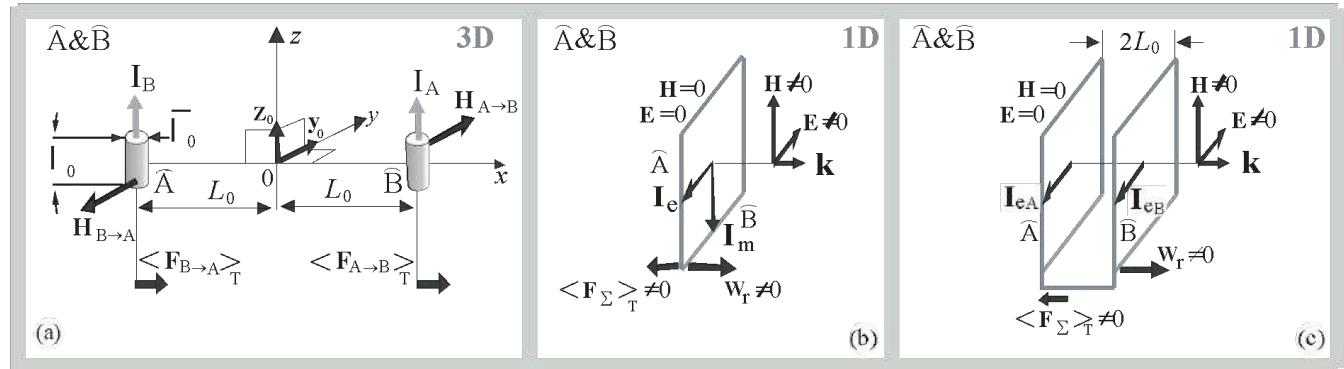

Fig. 4: To the problem of the wave thrust of a pair $\hat{A}\&\hat{B}$ of electromagnetic antennas: (a) the geometry of a pair of 3D elements of electric current $\mathbf{I}_A$ (antenna $\hat{A}$) and $\mathbf{I}_B$ (antenna $\hat{B}$); (b) one-dimensional Huygens source: a pair driven by mutually perpendicular electric $\mathbf{I}_e$ (antenna $\hat{A}$) and magnetic $\mathbf{I}_m$ (antenna $\hat{B}$) currents; (c) one-dimensional Huygens source: with electric currents $\mathbf{I}_{eA}$, $\mathbf{I}_{eB}$ located on two parallel planes, $\mathbf{W}_r$ - vector of power flax density of radiation.

III. WAVE THRUST OF ELECTROMAGNETIC SMALL ANTENNAS

Let's consider two current elements $\mathbf{I}_A = \mathbf{z}_0 I_A$, $\mathbf{I}_B = \mathbf{z}_0 I_B$, where $I_A = I_0 \exp(i\omega_0 t - i\varphi_A)$, $I_B = I_0 \exp(i\omega_0 t - i\varphi_B)$, $\mathrm{Re}\, I_0 = I_0$ (two emitters $\hat{A}$, $\hat{B}$ of length $\ell_0 \ll L_0$, with thickness $\delta_0 \ll \ell_0$ see Fig. 4-a), located at points $x = \mp L_0$. Currents I_A, I_B create magnetic fields on each other [17] ($\parallel \mathbf{y}_0$)

$$\mathbf{H}_{B\rightarrow A} = -\mathbf{y}_0 I_B \ell_0^2 k_0^2 \mu_0 [(2k_0 L_0)^{-2} + i(2k_0 L_0)^{-1}] \exp(i\omega_0 t - 2i k_0 L_0 - i\varphi_B) \quad , \tag{13}$$

$$\mathbf{H}_{A\rightarrow B} = -\mathbf{y}_0 I_A \ell_0^2 k_0^2 \mu_0 [(2k_0 L_0)^{-2} + i(2k_0 L_0)^{-1}] \exp(i\omega_0 t - 2i k_0 L_0 - i\varphi_A) \,, \tag{14}$$

which, in turn, generate the corresponding Ampere forces

$$\mathbf{F}_{B\rightarrow A} = \mu_0 [\mathbf{I}_A, \mathbf{H}_{B\rightarrow A}] \,, \qquad \mathbf{F}_{A\rightarrow B} = \mu_0 [\mathbf{I}_B, \mathbf{H}_{A\rightarrow B}] \,. \tag{15}$$

Note that currents I_A, I_B and generate end electric charges of equal magnitude and opposite sign, oscillating at a frequency ω_0. Therefore, the Coulomb force with which the antenna $\hat{A}$ ($\hat{B}$) acts with

its electric field on the end charge of the antenna $\hat{B}$ ($\hat{A}$) can be neglected. Thus, quantities $\mathbf{I}_A$, $\mathbf{H}_{B \to A}$, $\mathbf{I}_B$, $\mathbf{H}_{A \to B}$, oscillating at frequency $\omega = \omega_0$, generate forces $\mathbf{F}_{B \to A}(t)$, $\mathbf{F}_{A \to B}(t)$, whose spectral power densities are concentrated at frequencies $\omega = 2\omega_0$ and $\omega = 0$ ("frequency" of the wave propulsion force). From (15) we obtain expressions for the forces averaged over the period $2\pi / \omega_0$ like expressions (11), (12), which differ from the acoustic case only by the factor

$$q_a = 2\pi k_0^2 a_0^4 \rho_0 V_0^2 ,\tag{16}$$

instead of which we need to insert

$$q_e = I_0^2 \ell_0^2 k_0^2 \mu_0 / 4\pi ,\tag{17}$$

where μ_0 is the magnetic constant of the vacuum. The cross-section of the radiation power directional patterns for the electromagnetic problem along a plane $"x, y"$ coincides with the radiation patterns of pulsating spheres shown in Fig. 3. Note that in the electromagnetic boundary value problem described above, there is no both single and multiple scattering of waves by antennas $\hat{A}$, $\hat{B}$. Because currents I_A , I_B (precisely currents, and not implied metal vibrators) are transparent to the waves incident on them. But in the acoustic problem there is no radiation pressure on an object if this object does not scatter the waves incident on it. And yet, the dependence of forces $< \mathbf{F}_{A \to B} >_T$, $< \mathbf{F}_{B \to A} >_T$ on quantities $\alpha(2k_0 L_0)$ и $\beta(2k_0 L_0)$ remains the same as in the acoustic problem described above.

IV.   WAVE THRUST OF GRAVITATIONAL WAVES ON WATER SURFACE (EXPERIMENT)

To study the horizontal wave thrust (of gravitational waves on the surface of the water surface), a catamaran $\hat{A} \& \hat{B}$ was made, consisting of two identical rectangular floats (antennas) $\hat{A}$ and $\hat{B}$ with dimensions $0.18 \, \text{m} \times 0.09 \, \text{m} \times 0.12 \, \text{m}$ (see Fig. 5-a). The floats $\hat{A}$, $\hat{B}$ are made of light and rigid (relative to the water surface) foam plastic, oriented parallel to each other with respect to their length and rigidly connected to each other by a plate of the same foam plastic. This catamaran $\hat{A} \& \hat{B}$ was placed in basin of water volume of dimensions $50.0 \, \text{m} \times 4.0 \, \text{m} \times 2.0 \, \text{m}$ (the last is depth). Vertical oscillations of the floats $\hat{A}$, $\hat{B}$ are provided by two identical synchronous in-phase electric drives $\hat{D}$, the axes of which rotate in mutually opposite directions at frequency f_0 (Hz). Rigid thin light rods of length $0.06 \, \text{m}$ are rigidly attached to the ends of the axles of each electric drive, rotated relative to each other on the axis by an angle $\pi / 2$; point masses $m_0 = 0.25$ kg are fixed to these light thin rods. The action on the catamaran $\hat{A} \& \hat{B}$ of inertial forces of rotating masses m_0 attached to the axes of different drives $\hat{D}$ is mutually compensated in the horizontal direction. Thus, the rotation of the masses m_0 by electric drives $\hat{D}$ provides vertical forces applied to the floats $\hat{A}$ and $\hat{B}$ shifted relative to each other in phase by $\pi / 2$.

The physical mechanism for creating wave thrust is the same as in the acoustic problem in Section 1. The sinusoidal (with frequency f_0) immersion of the float $\hat{A}$ (or $\hat{B}$) simultaneously performs two functions: (a) radiates a wave traveling towards the float $\hat{B}$ (or $\hat{A}$); (b) modulates in time with

frequency f_0 the horizontal component of the force (proportional to the depth of immersion) with which the float $\hat{A}$ (or $\hat{B}$) is acted upon by a scattered wave generated by a wave coming from the float $\hat{B}$ (or $\hat{A}$). Thus, similar to Section 1, by selecting the necessary phases of oscillations of the floats, the distance between them and the excitation frequency, we hope to obtain a non-zero time-average horizontal force of the catamaran $\hat{A}\&\hat{B}$ wave thrust or in other words to obtain scattered field at frequencies $f = 2f_0$ and $f = 0$ (reactive flow).

When constructing the model $\hat{A}\&\hat{B}$, the main goal was to ensure geometric symmetry, hydrostatic symmetry and symmetry of moments of inertia, so that the asymmetry of the phases of rotation of the masses $m_0 = 0.25$ kg would manifest itself most clearly and a small wave thrust would become noticeable. At low frequencies, the wave thrust is "overshadowed" by unaccounted waves reflected from the walls of the basin (four meters wide) at the small inertia forces of the loads driving the model, as well as multiple scattering between the floats $\hat{A}$ and $\hat{B}$. At high frequencies, the wave thrust is "overshadowed" by the viscosity of the liquid. However, despite the interfering factors described above, the maximum force $F_0 = 0.02$ N (force measurements were averaged over at least four wave periods) of wave thrust was found at a frequency $f_0 = 1.14$ Hz when the model was fixed horizontally (i.e., at $V_0 = 0$ and the maximum speed $V_J = 0.023$ m/s of dust particles in the jet flow on the surface of the water (see [20]), and the maximum speed of the model, freed from horizontal fixation, reached value $V_0 = 0.009$ m/s. The dependence of the wave thrust force on frequency f_0 in the range from 2.0 Hz to -2.0 Hz was experimentally recorded, qualitatively similar to Fig. 3-b (black section of the function β) marked by black thick vertical lines which present the bounds of measurement errors. Quite remarkable is the fact that when the sign changing $f_0 \to -f_0$ of the rotation frequency (or when changing $t \to -t$) of the masses changed, the wave thrust force also changed the sign, saving its absolute value. In addition, at $f_0 \to -f_0$ the picture of the flow on the water surface was completely inverted ($V_J \to -V_J$). In this case, the load with the previously "lagging" phase of rotation became "advanced" (and vice versa). Two axes of rotation of the loads m_0 are needed so that the driving force of inertia of the loads does not have even an instantaneous projection onto the axis $"x"$ (the direction of the expected wave thrust). In Fig. 5-a shows the design of a catamaran. Fig. 5-b shows a top view of the catamaran $\hat{A}\&\hat{B}$ as well as the calculated cardioid radiation pattern (highlighted white field) and the structure of the vortex jet flow on the water surface similar to the flow around the propeller. Fig. 5-c represents the optimal frequency f_0 of rotation of the drives $\hat{D}$, the wave semi-distance k_0L_0 between the floats $\hat{A}$ and $\hat{B}$, and the phase φ_A and φ_B rotation of the masses m_0, at which the force F_0 of the wave thrust and the speed V_J of the jet stream of the attached catamaran, as well as the translational speed of the freed catamaran $\hat{A}\&\hat{B}$ are maximum. Fig. 5-d presents the experimental dependence of the wave thrust force on the rotation speed of electric drives $\hat{D}$, similar to (11) and Fig. 3-b.
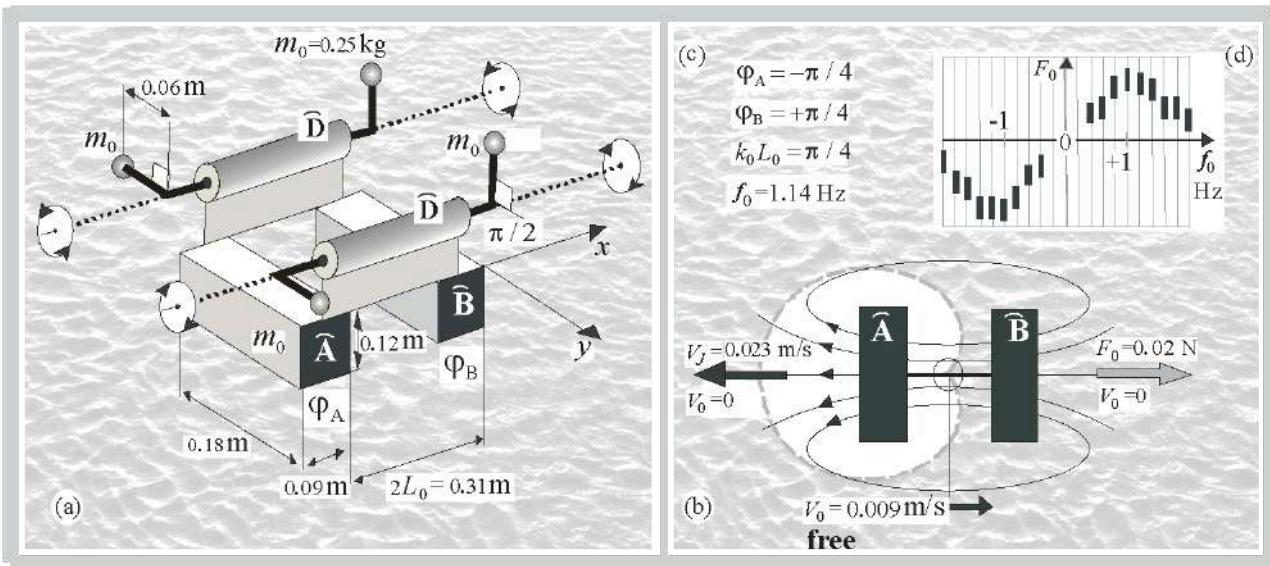
Figure 5: About the experiment with surface gravity waves on water: (a) the design of the model $\hat{A} \& \hat{B}$ (wave mover) from floats $\hat{A}$ and $\hat{B}$ identical masses $m_0 = 0.25$ kg located on axes with opposite sign and equal in magnitude rotation frequencies $\pm f_0$ determined by electric drives $\hat{D}$, the phases φ_A, φ_B of rotation are determined by the angle of attachment on the axis of rotation; b) top view (cardioid directional pattern of radiation and streamlines of the jet stream) as well as the highest values of the force of wave thrust F_0 and the speed V_J of particles of the jet stream with horizontal fixation ($V_0 = 0$) of the model $\hat{A} \& \hat{B}$, horizontal speed V_0 of the model $\hat{A} \& \hat{B}$ in free motion; (c) optimal parameters for creating wave thrust of the model used (a); (d) dependence of the wave thrust force F_0 on the excitation frequency f_0 of the model (see also Fig. 3-b)

V. WAVE MOVER AND HUIGENCE SOURCE

Since wave propulsion requires a difference in radiation power "forward" and "backward," below we will consider the similarities and differences in the design and characteristics of a 3D, 1D wave mover (WM) and a 3D, 1D Huygens source (HS) based on a two-element antenna.

The construction of WM and HS at 3D dimension: WM are two small spheres pulsating with speeds V_A, V_B in Fig. 2-a (or current elements I_A, I_B, Fig. 4-a) with phases $\varphi_A = -\pi/4$, $\varphi_B = +\pi/4$ (regardless of frequency ω_0); HS - the same two spheres (or current elements $I_A = -I_B \exp(2ik_0L_0)$) with phases of speeds (currents) $\varphi_A = -i\omega_0 L_0/c_0$ and $\varphi_B = +i\omega_0 L_0/c_0$ (proportional to frequency ω_0).

| $k_0 L_0$	$2.0\,(\pi/4)$	$1.5\,(\pi/4)$	$(\pi/4)$	$0.75(\pi/4)$	$0.5(\pi/4)$
WAVE MOVER					
HUIGENCE SOURCE					
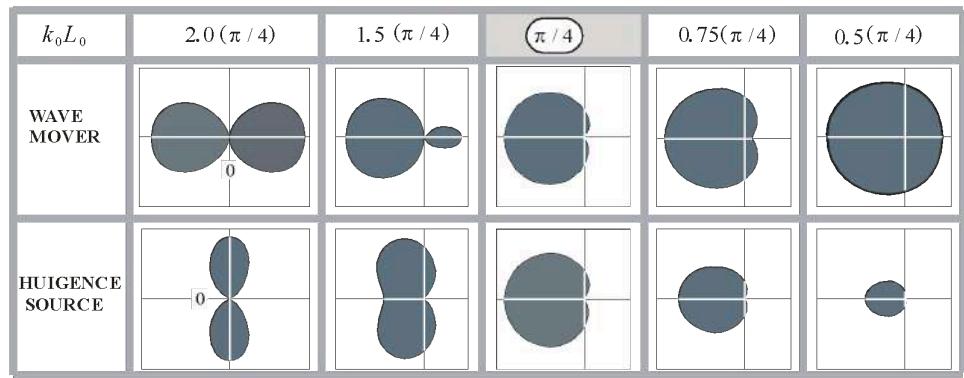
Figure 6: Directional patterns (in terms of power) of an acoustic wave propulsion device (3D mover, see Section 2) and a Huygens source for different wave sizes $k_0 L_0$ of the device and identical amplitude modulus of the normal oscillatory velocity on the surface of pulsing spheres (the intersection of the vertical and horizontal axes means zero power)

The requirement for a wave propulsion device is the maximum force of wave propulsion. The requirement for a Huygens source is a zero radiation pattern in one direction "forward" and non-zero radiation in the direction "backward" while saving (at $k_0 L_0 < \pi/4$) a constant shape of a single-lobe cardioid radiation pattern. The requirements for WM and HS and their characteristics are different (see Fig. 6), however, the combination of parameters $k_0 L_0 = \pi/4$, $\varphi_A = -\pi/4$, $\varphi_B = +\pi/4$ is a special case (Fig. 5-c) when WM and HS are identical to one another and the traction force β (11) is maximum (see Fig. 3-b). In the 3D case it is possible to create WM both for waves in a compressible inviscid medium and for electromagnetic waves in a vacuum.

In the 1D performance HS and WM are equivalent to one another at all frequencies ω_0. It is possible to create HS (see Fig. 4-b,c) for linear (in vacuum) electromagnetic waves (with the traditional expression $< \mathbf{F}_\Sigma >_T = -\mathbf{W}_r / c_0$ for the wave thrust force density, where $\mathbf{W}_r$ is the flux density vector of unilaterally radiated power. For example flat electromagnetic HS on one plane [17]: flat electric current produce the electric field which acts on perpendicular flat magnetic current and on the other hand flat magnetic current produce the magnetic field which acts on perpendicular flat electric current by Ampere force.

On the other hand, one can guess that the force of wave thrust (in the case of waves caused by vibrations of the masses of matter) is created by the vortex jet flow described in Section 3 and Fig-5-b (or acoustic flow for sound waves). After all, we assumed the wave fields to be stationary. The absence of avoiding (diffraction) of 1D obstacles (antennas) by such waves would mean the absence of a reactive vortex flow, because a spatially one-dimensional vortex is impossible. For example, an 1D unsupported HS is driven by pairs $\pm \mathbf{F}_A(t)$, $\mathbf{F}_B(t)$ of mutually opposite and equal in modulus forces ([20], [21] see Fig. 3-b) in the infinite homogeneous media, therefore such a source does not create reactive recoil at any frequency, including the zero frequency of the wave thrust force that interests us.

VI. CONCLUSIONS

The interaction of the simplest local emitters (small antennas) is analyzed analytically: two pulsating spheres in acoustics and two current elements in electrodynamics. An identical dependence (up to coefficients (16), (17)) for both cases (11), (12) of the interaction force on the distance between the emitters, their sizes, as well as the frequency, amplitude and phases of their excitation was obtained.

On the Mechanical Interaction between two Small Antennas

Formulas (11), (12) describe the effects of attraction, repulsion and propulsive action of emitters on each other.

Despite the identity of the above-mentioned analytical dependence (11), (12) in the acoustic (Section 1) and electrodynamic (Section 2) cases, there is a fundamental difference. Acoustic forces (11), (12) of interactions are generated by the modulation (Section 1) in time of the radii of the spheres $\hat{A}$, $\hat{B}$) and, accordingly, the modulation of the fields scattered by them, i.e. scattering plays a fundamentally important role in the generation of steady acoustic thrust force (10) of small antennas. But in the case of electromagnetic waves, to generate steady components of forces (15), scattering (and modulation of scattering in time) is not required at all, because the current element (emitter $\hat{A}$ or $\hat{B}$) does not create a scattering field (single or multiple scattering).

In addition, in the case of gravitational waves (Section 3), a vortex jet flow (Fig. 5-b) and wave thrust of a catamaran float $\hat{A} \& \hat{B}$ were experimentally detected on the water surface, the dependence of which on the frequency (Fig. 5-d) and on wave dimensions $k_0 L_0$ of the device is similar to the function (11) (Fig. 3-b), obtained for acoustic and electromagnetic waves (Sections 1, 2).

The results above obtained in the article can find potential application in the development of wave propulsion devices for the transfer of physical bodies and allow us to better understand the energy efficiency of such devices for acoustic waves, electromagnetic waves and gravitational waves on water surface.

ACKNOWLEDGMENTS

REFERENCES

1. Poynting, J.H. Radiation pressure. Philos. Mag. 9, 393–406 (1905) https://archive.org/details/paper-doi-10_1038_071200b0/mode/2up
2. Mc-Intire M. E. On the «wave momentum» myth//J. Fluid Mech. 25-th Anniversary issue, 1981, vol. 106, pp. 331-347.
3. Beyer R.T. Radiation pressure—The history of a mislabeled tensor //J. Acoust. Soc. Am. **63,** 1025-1030 (1978), https://www.ece.uvic.ca/~bctill/papers/numacoust/Beyer_1978.pdf
4. Lebedew P. Untersuchungen über die Druckkräfte des Lichtes // Annalen der Physik. 1901. fasc. 4, Bd 6, S. 433-458. doi: https://dx.doi.org/10.1002/andp.19013111102
5. Bjerknes C.A. Hydrodynamische Fernkrafte. Leipzig: Verlag von Wilhelm Engelmann, 1915.
6. Westervelt P.J. The theory of steady forces caused by sound waves.- JASA, 1951, v. 23, № 4, p. 312-315, doi: 10.1121/1.1906764 005
7. Yosioka K., Kawasima G. Acoustic Radiation Pressure on Compressible Sphere //Acoustic, 1955, v. 5, № 3, p. 167—173. 2009.
8. Hasegawa T, Kido T, Iizuka T, Matsuoka C. A general theory of Rayleigh and Langevin radiation pressures //The Journal of the Acoustical Society of Japan (E), (2000), *21* (3): 145-152. doi:10.1250/ast.21.145
9. Prosperetti Andrea, Lawrence A Crum, Kerry W. Commander Nonlinear bubble dynamics // JASA, V. 83, February 1988, P. 502-514. doi: 10.1121/1.396145 doi:10.1016/j.solener.2020.04.090
10. Doinikov A. Translational motion of two interacting bubbles in a strong acoustic field // Phys Rev E. 64.026301. 2001 Jul 16. doi: 10.1103/PhysRevE.64.026301

11. Nelson G.C. Astrath, Luis C. Malacarne, Mauro L. Unravelling the effects of radiation forces in water // Nature Communications, Published 7 Jul 2014, doi: 10.1038/ncomms5363 |www.nature.com/naturecommunica

12. Na Yan, Wen-Li Di , Zhen-Yu Hong, Wen-Jun Xie and Bing-BoWei Dynamic Superposition and Levitation Capability of Two Confronting Ultrasonic Waves 2019 Chinese Physics Letters, Volume 36, Number 3, P. 034303 doi: 10.1088/0256-307X/36/3/034303

13. Na Yan, Wen-Li Di , Zhen-Yu Hong, Wen-Jun Xie and Bing-BoWei Dynamic Superposition and Levitation Capability of Two Confronting Ultrasonic Waves 2019 Chinese Physics Letters, Volume 36, Number 3, P. 034303 doi: 10.1088/0256-307X/36/3/034303

14. Félix S., Thibaut D., Lionel H. and Samuel C., "Water-air interface deformation induced by a transient acoustic radiation force," 2021 *IEEE International Ultrasonics Symposium (IUS)*, Xi'an, China, 2021, pp. 1-4 , doi: 10.1109/IUS52206.2021.9593395

15. Denisov G.G. Momentum, Radiation Pressure, and Other Second-Order Quantities in Ideal Gas (Liquid) in Some Boundary-Value Problems //Acoustical Physics, Vol. 46, No. 3, 2000, pp. 287–294. doi: https://doi.org/10.1134/1.29883

16. L.D. Landau, E.M. Lifshitz, *Course of theoretical physics* (*Fluid Mechanics*), Vol. 6, Butterworth-Heinemann, 2 edition, Jan 15, 1987.

17. Nikolskii V.V. *Theory of Electromagnetic Field*, "Visshaya shkola", Moskow, 1961.

18. Arabadzhi V.V. Wave thrust of local emitters, Proceedings XXXVI Session RAS, Moscow (wave propagation and diffraction section), October 21-25, 2024, P. 515-523, doi: 10.34756/GEOS.2024.17.38888

19. Lependin L.F. *Acoustics*, 1978 (in Russian).

20. Carl Eckart Vortices and Streams Caused by Sound Waves // Phys. Rev. **73**, 68 – Published 1 January 1948, DOI: https://doi.org/10.1103/PhysRev.73.68

21. Arabadzhi V.V. Supportless Unidirectional Acoustic Sources //Acoustical Physics, 2009, Vol. 55, No. 1, pp. 120–131, doi: https://doi.org/10.1134/S106377100901014X

22. Arabadzhi, V.V. *Solutions to Problems of Controlling Long Waves with the Help of Micro-structure Tools*. Bentham Science Publishers, 2011, doi: 10.2174/9781608052752111010

On the Mechanical Interaction between two Small Antennas

Great Britain Journal Press Membership

For Authors, subscribers, Boards and organizations

Great Britain Journals Press membership is an elite community of scholars, researchers, scientists, professsionals and institutions associated with all the major disciplines. Great Britain memberships are for indivi - duals, research institutions, and universities. Authors, subscribers, Editorial Board members, Advisory Board members, and organizations are all part of member network.

Read more and apply for membership here:
https://journalspress.com/journals/membership

Author Membership provide access to scientific innovation, next generation tools, access to conferences/seminars/ symposiums/webinars, networking opportunities, and privileged benefits. Authors may submit research manuscript or paper without being an existing member of GBJP. Once a non-member author submits a research paper he/she becomes a part of "Provisional Author Membership".

Society flourish when two institutions Come together." Organizations, research institutes, and universities can join GBJP Subscription member-shipor privileged "Fellow Membership" membership facilitating researchers to publish their work with us, become peer reviewers and join us on Advisory Board.

Subscribe to distinguished STM (scientific, technical, and medical) publisher. Subscription member-ship is available for individuals universities and institutions (print & online). Subscribers can access journals from our libraries, published in different formats like Printed Hardcopy, Interactive PDFs, EPUBs, eBooks, indexable documents and the author managed dynamic live web page articles, LaTeX, PDFs etc.

PRINTED VERSION, INTERACTIVE PDFS, EPUBS, EBOOKS, INDEXABLE
DOCUMENTS AND THE AUTHOR MANAGED DYNAMIC LIVE WEB PAGE
ARTICLES, LATEX, PDFS, RESTRUCTURED TEXT, TEXTILE, HTML, DOCBOOK,
MEDIAWIKI MARKUP, TWIKI MARKUP, OPML, EMACS ORG-MODE & OTHER